Implementation and evaluation of the GEOS-Chem chemistry module version 13.1.2 within the Community Earth System Model v2.1

Thibaud M. Fritz[1], Sebastian D. Eastham[1,2]*, Louisa K. Emmons[3], Haipeng Lin[4], Elizabeth W. Lundgren[4], Steve Goldhaber[3], Steven R. H. Barrett[1,2], Daniel J. Jacob[4]

[1]Laboratory for Aviation and the Environment, Department of Aeronautics and Astronautics, Massachusetts Institute of Technology, Cambridge, MA 02139, USA

[2]Joint Program on the Science and Policy of Global Change, Massachusetts Institute of Technology, Cambridge, MA 02139, USA

[3]Atmospheric Chemistry Observations and Modeling Laboratory, National Center for Atmospheric Research, Boulder, CO, USA

[4]John A. Paulson School of Engineering and Applied Sciences, Harvard University, Cambridge, MA 02138, USA

**Correspondence to*: Sebastian D. Eastham (seastham@mit.edu)

Short summary. We bring the state-of-the-science chemistry module GEOS-Chem into the Community Earth System Model (CESM). We show that some known differences between results from GEOS-Chem and CESM's CAM-chem chemistry module may be due to the configuration of model meteorology rather than inherent differences in the model chemistry. This is a significant step towards a truly modular ESM and allows two strong but currently separate research communities to benefit from each other's advances.

Abstract. We implement the GEOS-Chem chemistry module as a chemical mechanism in the Community Earth System Model version 2 (CESM). Our implementation allows the state-of-the-science GEOS-Chem chemistry module to be used with identical emissions, meteorology, and climate feedbacks as the CAM-chem chemistry module within CESM. We use coupling interfaces to allow GEOS-Chem to operate almost unchanged within CESM. Aerosols are converted at each time step between the GEOS-Chem bulk representation and the size-resolved representation of CESM's Modal Aerosol Model (MAM4). Land type information needed for dry deposition calculations in GEOS-Chem is communicated through a coupler, allowing online land-atmosphere interactions. Wet scavenging in GEOS-Chem is replaced with the Neu and Prather scheme, and a common emissions approach is developed for both CAM-chem and GEOS-Chem in CESM.

We compare how GEOS-Chem embedded in CESM (C-GC) compares to the existing CAM-chem chemistry option (C-CC) when used to simulate atmospheric chemistry in 2016, with identical meteorology and emissions. We compare atmospheric composition and deposition tendencies between the two simulations and evaluate the residual differences between C-GC compared to its use as a standalone chemistry transport model in the GEOS-Chem High Performance configuration (S-GC). We find that stratospheric ozone agrees well between the three models with differences of less than 10% in the core of the ozone layer, but that ozone in the troposphere is generally lower in C-GC than in either C-CC or S-GC. This is likely due to

greater tropospheric concentrations of bromine, although other factors such as water vapor may contribute to lesser or greater extents depending on the region. This difference in tropospheric ozone is not uniform, with tropospheric ozone in C-GC being 30% lower in the Southern Hemisphere when compared to S-GC but within 10% in the Northern Hemisphere. This suggests differences in the effects of anthropogenic emissions. Aerosol concentrations in C-GC agree with those in S-GC at low altitudes in the tropics but are over 100% greater in the upper troposphere due to differences in the representation of convective scavenging. We also find that water vapor concentrations vary substantially between the standalone and CESM-implemented version of GEOS-Chem, as the simulated hydrological cycle in CESM diverges from that represented in the source NASA MERRA-2 reanalysis meteorology which is used directly in the GEOS-Chem CTM.

Our implementation of GEOS-Chem as a chemistry option in CESM (including full chemistry-climate feedback) is publicly available and is being considered for inclusion in the CESM main code repository. This work is a significant step in the MUlti-Scale Infrastructure for Chemistry and Aerosols (MUSICA) project, enabling two communities of atmospheric researchers (CESM and GEOS-Chem) to share expertise through a common modeling framework and thereby accelerate progress in atmospheric science.

1. Introduction

Accurate representation and understanding of atmospheric chemistry in global Earth System Models (ESMs) has been recognized as an urgent priority in geoscientific model development. The National Research Council (NRC) report on a National Strategy for Advancing Climate Modeling (Bretherton et al., 2012) stresses the need for including comprehensive atmospheric chemistry in the next generation of ESMs. The NRC report on the Future of Atmospheric Chemistry (NRC, 2016) identifies the integration of atmospheric chemistry into weather and climate models as one of its five priority science areas. This work responds to those needs, presenting the implementation of the state-of-science model GEOS-Chem (Bey et al., 2001; Eastham et al., 2018) as an atmospheric chemistry module within the Community Earth System Model (CESM) (Hurrell et al., 2013; Tilmes et al., 2016; Lamarque et al., 2012; Emmons et al., 2020).

GEOS-Chem is a state-of-the-science global atmospheric chemistry model developed and used by over 150 research groups worldwide (http://geos-chem.org). It has wide appeal among atmospheric chemists because it is a comprehensive, state-of-science, open-access, well-documented modeling resource that is easy to use and modify but also has strong central management, version control, and user support. The model is managed at Harvard by a GEOS-Chem Support Team with oversight from an international GEOS-Chem Steering Committee. Documentation and communication with users is done through extensive web and wiki pages, email lists, newsletters, and benchmarking. Grass-roots model development is done by users, and inclusion into the standard model is prioritized by Working Groups reporting to the Steering Committee. The model can simulate tropospheric and stratospheric oxidant-aerosol chemistry, aerosol microphysics, and budgets of various gases .

Simulations can be conducted on a wide range of computing platforms with either shared-memory (OpenMP) or distributed memory (MPI) parallelization – with this latter implementation referred to as GEOS-Chem High Performance, or GCHP (Eastham et al., 2018).

For the general atmospheric chemistry problem involving K atmospheric species coupled by chemistry and/or aerosol microphysics, GEOS-Chem solves the system of K coupled continuity equations

$$\frac{\partial n_i}{\partial t} = -\nabla \cdot (n_i \mathbf{U}) + P_i(\mathbf{n}) - L_i(\mathbf{n}) \quad (1)$$

where $\mathbf{n} = (n_1, \ldots n_K)^T$ is the number density vector representing the concentrations of the K species, $\mathbf{U}$ is the 3-D wind vector, and P_i and L_i are local production and loss terms for species i including emissions, deposition, chemistry, and aerosol physics. The transport term $-\nabla \cdot (n_i \mathbf{U})$ includes advection by grid-resolved winds as well as parameterized subgrid turbulent motions (boundary layer mixing, convection). The local term $P_i(\mathbf{n}) - L_i(\mathbf{n})$ couples the continuity equations across species through chemical kinetics and aerosol physics.

Standard application of the GEOS-Chem model as originally described by Bey et al. (2001) is off-line, meaning that the model does not simulate its own atmospheric dynamics. Instead, it uses analyzed winds and other meteorological variables produced by Goddard Earth Observation System (GEOS) simulations of the NASA Global Modeling and Assimilation Office (GMAO) with assimilated meteorological observations. The near-real time GEOS Forward Processing (GEOS-FP) output provides data globally at a horizontal resolution of 0.25°×0.3125°, and the Modern-Era Retrospective analysis for Research and Applications, Version 2 (MERRA-2) provides data at 0.5°×0.625°. GEOS-Chem simulations can be conducted at that native resolution or at coarser resolution (by conservative re-gridding of meteorological fields). Long et al. (2015) developed an on-line capability for GEOS-Chem to be used as a chemical module in ESMs, with initial application to the GEOS ESM. In that configuration, GEOS-Chem only solves the local terms of the continuity equation

$$\frac{\partial n_i}{\partial t} = P_i(\mathbf{n}) - L_i(\mathbf{n}) \quad (2)$$

and delivers the updated concentrations to the ESM for computation of transport through its atmospheric dynamics. On-line simulation avoids the need for a meteorological data archive and the associated model transport errors (Jöckel et al., 2001; Yu et al., 2018). It also enables fast coupling between chemistry and dynamics.

Transformation of GEOS-Chem to a grid-independent structure was performed transparently, such that the standard GEOS-Chem model uses the exact same code for on-line and off-line applications. This includes a mature implementation within the

GEOS ESM. It was applied recently to a year-long tropospheric chemistry simulation with ≈12 km (cubed-sphere c720) global resolution (Hu et al., 2018), and is now being used for global atmospheric composition forecasting (Keller et al., 2017, 2021). However, the only implementations of GEOS-Chem which are currently publicly available are either designed to run "offline", driven by archived meteorological data from the NASA Goddard Earth Observing System (GEOS) (Bey et al., 2001; Eastham et al., 2018), or operate at regional scale and do not extend to global simulation (Lin et al., 2020; Feng et al., 2021).

Integration of GEOS-Chem as a chemistry option within an open-access, global ESM responds to the aforementioned calls from the NRC. One of the most widely used open-access ESM is the Community Earth System Model (CESM) (Hurrell et al., 2013). CESM is fully coupled and state-of-science. It produces its own meteorology based on fixed sea surface temperatures or with a fully interactive ocean model. It can also be nudged to observed meteorology including from GEOS. The CESM configuration with chemistry covering the troposphere and stratosphere is referred to as CAM-chem (Community Atmosphere Model with chemistry) (Tilmes et al., 2016; Lamarque et al., 2012). CAM-chem is a state-of-science model of atmospheric chemistry; it has participated (along with CESM's WACCM model which extends to the lower thermosphere) in many international model intercomparison activities such as ACCMIP, CCMI, POLMIP, HTAP2, GeoMIP and CMIP6, and has a large international user community. CAM-chem also has a very different development heritage from GEOS-Chem, with each model providing better performance in comparison to observations in different areas (Park et al., 2021; Emmons et al., 2015; Nicely et al., 2017; Jonson et al., 2018). It is widely used for simulations of global tropospheric and stratospheric atmospheric composition, in part because it is able to run either with specified meteorological datasets or with fully-coupled physics (https://www2.acom.ucar.edu/gcm/cam-chem).

The fundamental differences in implementation of almost every atmospheric process between GEOS-Chem and CAM-chem mean that it is difficult to disentangle the root causes of these differences. Modular Earth system models can resolve this issue. Allowing individual scientific components to be swapped freely allows researchers to evaluate exactly what effect that component has in isolation, while also giving a single user base access to a larger portfolio of options. If two different models each implement five processes in different ways, a researcher must learn to use both in order to compare their results and cannot isolate the effect of any one process with confidence. If process options are implemented in the same framework, this problem is avoided. Such modularity is becoming increasingly possible with the availability of Earth system infrastructure such as the Earth System Modeling Framework (ESMF) and the National Unified Operational Prediction Capability (NUOPC), which describe common interfaces for Earth system modeling components (Hill et al., 2004; Sandgathe et al., 2011). The Multi-Scale Infrastructure for Chemistry and Aerosols (MUSICA) builds upon this trend with process-level modularization, with the goal of allowing researchers to select from a range of community-developed options when performing atmospheric simulations.

This work integrates the GEOS-Chem chemistry module into CESM as an alternative option to CAM-chem. Our implementation allows researchers to select either model to simulate gas-phase and aerosol chemistry throughout the troposphere and stratosphere, while other processes such as advection, broadband radiative transfer, convective transport, and emissions are handled nearly identically. We demonstrate this capability by comparing simulations of the year 2016 as generated by GEOS-Chem and CAM-chem operating within CESM, with the chemical module being the only difference. Estimates of atmospheric composition are compared between the two models and against a simulation in the standalone GCHP chemistry transport model (CTM). Finally, we evaluate the accuracy of the three approaches against observations of atmospheric composition and deposition.

Section 2 provides a technical description of the implementation of GEOS-Chem into CESM. Section 3 then describes the model setup. Sections 4 and 5 present a one-year simulation (not including spin up) performed in CESM with GEOS-Chem; CESM with CAM-chem; and the standalone GEOS-Chem CTM. This includes model intercomparison (Section 4), and evaluation against surface and satellite measurements (Section 5).

2. Coupling between GEOS-Chem and CESM

We first describe the interface used within CESM when using either the CAM-chem or GEOS-Chem options (Section 2.1). Unless otherwise stated, "GEOS-Chem" refers to the grid independent chemistry module which is common to all implementations, including standalone GEOS-Chem with OpenMP (Classic) or MPI (GCHP) parallelization, NASA GMAO's GEOS ESM, and WRF coupled with GEOS-Chem (WRF-GC). We then briefly summarize the chemistry and processes represented by the CAM-chem and GEOS-Chem options within CESM (Section 2.2). This is followed by a description of differences between the implementation of GEOS-Chem in CESM and its stand-alone code (Section 2.3), differences in the data flow through CESM when using GEOS-Chem as opposed to CAM-chem (Section 2.4), and finally the installation and compilation process (Section 2.5).

2.1. Interface

Our approach embeds a full copy of the GEOS-Chem chemistry module source code (version 13.1.2) within CESM (version 2.1.1). All modifications made to the GEOS-Chem source code have been propagated to the GEOS-Chem main code branch (https://github.com/geoschem/geos-chem) to ensure future compatibility between CESM and GEOS-Chem. Information is passed between the CESM Community Atmosphere Model (CAM) version 6 (CAM6) and the GEOS-Chem routines through an interface layer developed as part of this work. A schematic representation of the implementation is provided in Figure 1.

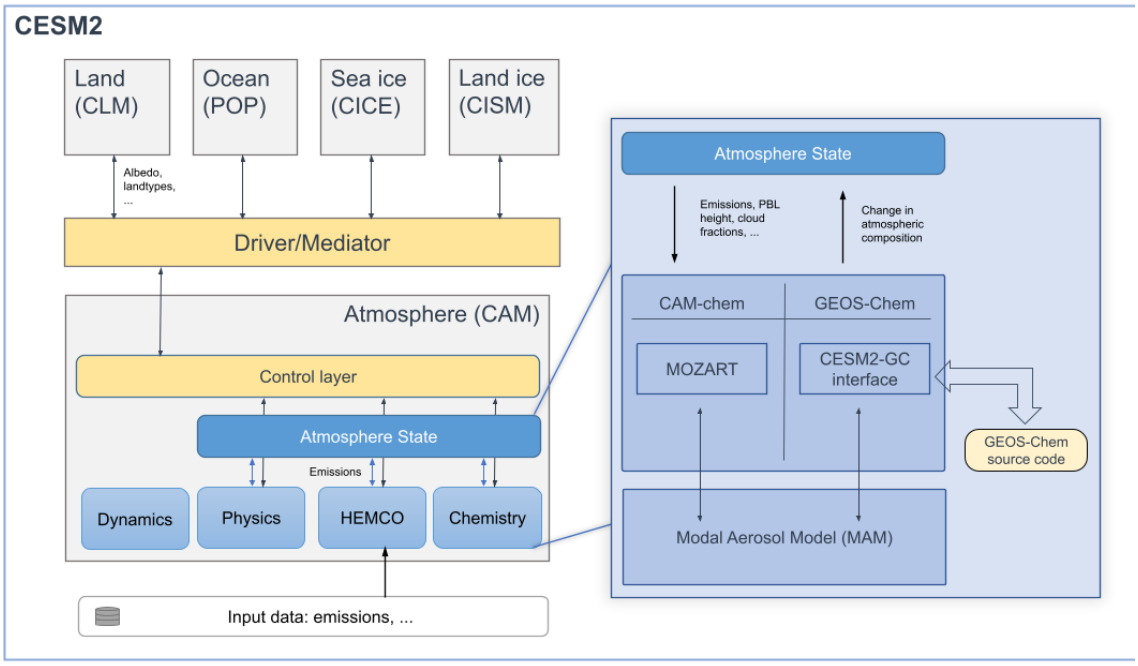

Figure 1. Architectural overview of CESM when running with either the GEOS-Chem or CAM-chem chemistry options. The left section shows the architecture of CESM, where the five major Earth system components are connected through the driver/mediator. The work presented here changes only the contents of the atmosphere component (CAM). Regardless of the chemistry option used, dynamics, physics, and emissions (HEMCO) are handled identically. Each component modifies the "Atmosphere State" while communication occurs through the control layer. The choice of chemistry module is confined to the "Chemistry" subcomponent, where either CAM-chem or GEOS-Chem can be chosen. In each case, data are transmitted between the "Atmosphere State" and the chemistry module, which interacts in turn with the Modal Aerosol Model. Dynamics are shown separately as they act on a "dynamics container" rather than directly on the atmospheric state. Further detail regarding timing of calls is provided in the Supplementary Information.

At each time step, CESM calls the coupling interface (referred to as CESM2-CG interface in Figure 1) which fills in the meteorological variables required by either CAM-chem or GEOS-Chem. Atmospheric transport and physics are identical whether using CAM-chem or GEOS-Chem to simulate atmospheric chemistry. The interface passes species concentrations from CAM to GEOS-Chem, which are then modified by GEOS-Chem and passed back to CAM. Meteorological data and land data are also passed to GEOS-Chem through the same interface. The routine calls in CAM when using either GEOS-Chem or CAM-chem are identical, with the appropriate chemistry module defined at compilation time such that the calls are routed to the appropriate routines.

The interface handles the conversion of meteorological variables and concentrations of atmospheric constituents between the state variables in CAM and those used in GEOS-Chem. Since GEOS-Chem operates in a "grid-independent" fashion, changes in the grid specification and other upstream modifications to CESM do not necessitate any changes to this interface (Long et al., 2015). Our version of CESM 2.1.1 is modified such that emissions are handled by the Harmonized Emissions Component

(HEMCO), which operates independently of the chemistry module and can provide emissions data to either CAM-chem or GEOS-Chem equally (Lin et al., 2021).

The interface code is kept in a subfolder of chemistry source code (`src/chemistry/geoschem` subfolder), which also contains a copy of the source code for GEOS-Chem. Unlike the implementation of GEOS-Chem within GEOS, we do not use ESMF. However, we plan to develop a NUOPC-based interface as part of future work.

2.2. Processes represented by CAM-chem and GEOS-Chem

CAM-chem uses the Model for OZone And Related chemical Tracers (MOZART) family of chemical mechanisms to simulate atmospheric chemistry (Emmons et al., 2020). The tropospheric-stratospheric MOZART-TS1 scheme which we demonstrate in our intercomparison involves 186 gas-phase chemical species and includes stratospheric bromine and chlorine chemistry. MOZART-TS1 does not include detailed tropospheric halogen chemistry or short-lived halogen sources such as sea salt bromine, although these will be available in a future release (Badia et al., 2021; Fernandez et al., 2021). Photolysis rates are calculated using a lookup table, based on calculations with the Tropospheric Ultraviolet and Visible (TUV) radiation model (Kinnison et al., 2007). Wet deposition is calculated using the Neu and Prather (2012) scheme for both convective and large-scale precipitation. Dry deposition velocities over land are calculated for each land type by the Community Land Model (CLM) in CESM using the Wesely (1989) resistance scheme with updates described by Emmons et al. (2020). Deposition velocities over the ocean are calculated separately in CAM-chem. Aerosols are represented using the 4-mode Modal Aerosol Model (MAM4), which includes sulfate, black carbon, primary, and secondary organic aerosols (SOAs) (Mills et al., 2016). Ammonium and ammonium nitrate aerosols are calculated with a parameterization using the bulk aerosol scheme (Tilmes et al., 2016). SOAs are simulated using a 5-bin volatility basis set (VBS) scheme, formed from terpenes, isoprene, specific aromatics and lumped alkanes through reaction with OH, ozone and NO_3, with unique yields for each for each combination of volatility and size bin (Tilmes et al., 2019). This more detailed scheme differs from the default MAM SOA scheme that is used in CAM6 (without interactive chemistry). Aerosol deposition, including dry and wet deposition, and gravitational settling (throughout the atmosphere) are calculated in the MAM code of CESM. CAM-chem also uses a volatility basis set (VBS) approach for SOA with five volatility bins, covering saturation concentrations with logarithmic spacing from 0.01 to 100 $\mu g.m^{-3}$. CAM-chem explicitly represents Aitken and accumulation mode SOA using two separate tracers for each volatility bin but does not include an explicit representation of non-volatile aerosol.

GEOS-Chem uses a set of chemical mechanisms implemented with the Kinetic PreProcessor (KPP) (Damian et al., 2002). The standard chemical mechanism has evolved continuously from the tropospheric gas-phase scheme described by Bey et al. (2001) and now includes aerosol chemistry (Park, 2004), stratospheric chemistry (Eastham et al., 2014), and a sophisticated tropospheric-stratospheric halogen chemistry scheme (Wang et al., 2019). The scheme present in GEOS-Chem 13.1.2 includes 299 chemical species. Additional "specialty simulations" such as an aerosol-only option and a simulation of the global mercury

cycle are present in GEOS-Chem but are not implemented into CESM in this work. Photolysis rates are calculated using the Fast-JX v7 model (Wild et al., 2000). When implemented as the standalone model, wet deposition is calculated for large-scale precipitation using separate approaches for water-soluble aerosols (Liu et al., 2001) and gases (Amos et al., 2012) with calculation of convective scavenging performed inline with convective transport. A different approach is used to simulate wet scavenging for the implementation of GEOS-Chem in CESM (see Section 2.3.4). Dry deposition is calculated using the Wesely (1989) scheme (Wang et al., 1998), but with updates for nitric acid (HNO_3) (Jaeglé et al., 2018), aerosols (Jaeglé et al., 2011; Alexander et al., 2005; Fairlie et al., 2007; Zhang et al., 2001), and over ocean (Pound et al., 2020). The representation of aerosols in GEOS-Chem varies by species. Sulfate-ammonium-nitrate aerosol is represented using a bulk scheme (Park, 2004), with gas-particle partitioning determined using ISORROPIA II (Fountoukis and Nenes, 2007). Modal and sectional size-resolved aerosol schemes are available for GEOS-Chem (Kodros and Pierce, 2017; Yu and Luo, 2009), but are disabled by default and not used in this work. Sea salt aerosol is represented using two (fine and coarse) modes (Jaeglé et al., 2011), while dust is represented using four size bins (Fairlie et al., 2007). We use the "complex SOA" chemistry mechanism in GEOS-Chem when running in CESM, as this uses a volatility basis set (VBS) representation of secondary organic aerosol which is broadly compatible with that used in CAM--chem (Pye and Seinfeld, 2010; Marais et al., 2016; Pye et al., 2010). The complex SOA VBS scheme uses four volatility bins covering saturation concentrations on a logarithmic scale from 0.1 to 100 $\mu g.m^{-3}$. Two classes of SOA are represented in this fashion: those derived from terpenes (TSOA) and those derived from aromatics (ASOA). For each "class" of SOA, two tracers are used to represent each volatility bin (one holding the gas phase mass, the other holding the condensed phase mass). The only exception is the lowest-volatility aromatic aerosol, which is considered to be non-volatile and therefore has no gas-phase tracer. Two additional SOA tracers, representing isoprene-derived and glyoxal-derived SOA, are not represented using a VBS approach.

Additional differences between the two chemistry modules include the use of different Henry's law coefficients, gravitational settling schemes, representation of polar stratospheric clouds, and heterogeneous chemistry. Full descriptions of the two models are available at https://geos-chem.seas.harvard.edu/ and in Emmons et al. (2020).

2.3. Representation of atmospheric processes in GEOS-Chem when running in CESM

Some processes cannot be easily transferred from standalone GEOS-Chem to its implementation in CESM, due to factors such as the different splitting of convective transport in the two models. Processes which vary in their implementation between the standalone and CESM implementations of GEOS-Chem are described below.

2.3.1. Aerosol coupling in CESM with GEOS-Chem

Since GEOS-Chem and CESM use different approaches to represent aerosols, there is no straight-forward translation between the GEOS-Chem representation and that used elsewhere in CESM. We implement an interface between the CESM and GEOS-

Chem representations, so that GEOS-Chem's processing of aerosols is most accurately represented without compromising the microphysical simulations and radiative interactions of aerosol calculated elsewhere in CESM.

CESM uses the 4-mode version of the Modal Aerosol Model (MAM4) to represent the aerosol size distribution and perform aerosol microphysics (Liu et al., 2016). This represents the mass of sulfate aerosols, secondary organic matter (in five volatility basis set bins), primary organic matter, black carbon, soil dust, and sea salt with advected tracers for each mode (accumulation, Aitken, coarse, and primary carbon), although some species are considered only in a subset of the four modes. A tracer is also implemented for the number of aerosol particles in each mode, resulting in a total of 18 tracers. As discussed above, GEOS-Chem instead represents sulfate, nitrate, and ammonium aerosol constituents with three tracers; fresh and aged black and organic carbon with four tracers; fine and coarse sea salt as two tracers; and different sizes of dust with four tracers. Six additional tracers are used to track the bromine, iodine, and chlorine content of each mode of sea salt aerosol, with two more used to track overall alkalinity. Gas-phase sulfuric acid (H_2SO_4) is assumed to be negligible in the troposphere and is estimated using an equilibrium calculation in the stratosphere (Eastham et al., 2014). The GEOS-Chem mechanism therefore represents greater chemical complexity but reduced size resolution compared to the aerosol representation in MAM4.

Accordingly, when receiving species concentrations from CESM, the interface to GEOS-Chem lumps all modes of the MAM aerosol into the corresponding GEOS-Chem tracer. This includes gas-phase H_2SO_4, in the case of the GEOS-Chem sulfate (SO_4) tracer. Aerosol constituents which are not represented explicitly by MAM (e.g. nitrates) are not included in this calculation. The relative contribution of each mode is stored during this "lumping" process for each grid cell. Once calculations with GEOS-Chem are complete, the updated concentration of the lumped aerosol is repartitioned into the MAM tracers based on the stored relative contributions in each grid cell.

For SOAs, additional steps are needed. For the bins covering saturation concentrations of 1 $\mu g.m^{-3}$ and greater, we assume that the relevant volatility bin in MAM4 is equal to the sum of the two classes in GEOS-Chem covering the same saturation concentrations. For example, the tracers TSOA1 and ASOA1 in GEOS-Chem are combined to estimate the total quantity of the Aitken and accumulation modes for species "soa3" in MAM4. Partitioning between the two modes (when transferring from GEOS-Chem to MAM4) is calculated based on the relative contribution of each constituent to the total prior to processing by GEOS-Chem. Partitioning between the two classes (when transferring from MAM4 to GEOS-Chem) is calculated based on the relative contribution of each constituent to the total at the end of the previous time step. For the lowest-volatility species, we split the lowest volatility bin concentrations (and non-volatile species) from GEOS-Chem between the two lowest volatilities in MAM4. A full mapping for all species is provided in Table 1.

Table 1. Mapping between tracers used to represent SOA in GEOS-Chem and CAM-chem. Translation between GEOS-Chem and MAM4 is performed by preserving the relative contributions provided during the previous transfer.

GEOS-Chem species	Mapping to CAM-chem species	Saturation concentration range ($\mu g.m^{-3}$)	Phase
TSOA0 + ASOAN	soa1_a1 + soa1_a2 + soa2_a1 + soa2_a2	0 – 0.1	Aerosol
TSOA1 + ASOA1	soa3_a1 + soa3_a2	0.1 – 1.0	Aerosol
TSOA2 + ASOA2	soa4_a1 + soa4_a2	1.0 – 10	Aerosol
TSOA3 + ASOA3	soa5_a1 + soa5_a2	10 – 100	Aerosol
TSOG0	SOAG0 + SOAG1	0 – 0.1	Gas
TSOG1 + ASOG1	SOAG2	0.1 – 1.0	Gas
TSOG2 + ASOG2	SOAG3	1.0 – 10	Gas
TSOG3 + ASOG3	SOAG4	10 – 100	Gas

Finally, MAM simulates some chemical processing on and in the aerosol. This includes the reaction of sulfur dioxide with hydrogen peroxide and ozone in clouds, which is already included in the GEOS-Chem chemistry mechanism. We therefore disable in-cloud sulfur oxidation in MAM4 when using the GEOS-Chem chemistry component in CESM, consistent with the GEOS-Chem CTM. A comparison of the effect of each approach is provided in the Supplementary Information.

2.3.2. Dry deposition

Dry deposition velocities over land are calculated in CESM for each atmospheric constituent by the Community Land Model (CLM) using a species database stored by the coupler. GEOS-Chem is also able to calculate its own dry deposition velocities (see Section 2.2), in situations where a land model is not available such as when running as a CTM. We thus implement different options to compute dry deposition velocities when running CESM with the GEOS-Chem chemistry option:

1. Dry deposition velocities over land are computed by CLM and are passed to CAM through the coupler. They are then merged with dry deposition velocities computed over ocean and ice by GEOS-Chem, identical to the procedure used in CAM-chem. Each of these are scaled by the land and ocean/ice fraction respectively.
2. GEOS-Chem computes dry deposition at any location using the land types and leaf area indices from CLM, which are passed through the coupler.
3. GEOS-Chem obtains “offline” land types and leaf area indices and computes the dry deposition velocities similarly to GEOS-Chem Classic.

This allows researchers to experiment with different dry deposition options, ranging from that most consistent with the approach used in CAM-chem (option 1) to that most consistent with stand-alone GEOS-Chem (option 3). For this work we use option 2, but option 1 will be brought as standard into the CESM main code to reduce data transfer requirements.

2.3.3. Emissions

The Harmonized Emissions Component (HEMCO) is used to calculate emissions in standalone GEOS-Chem (Keller et al., 2014), and HEMCO v3.0 was recently implemented as an option for CAM-chem (Lin et al., 2021). HEMCO offers the possibility for the user to read, regrid, overlay, and scale emission fluxes from different archived emissions inventories at runtime. Emissions extensions allow for the computation of emissions that depend on meteorology or surface characteristics (e.g. lightning, dust emissions). Some extensions have also been designed to calculate subgrid-scale chemical processes, such as non-linear chemistry in ship plumes (Vinken et al., 2011).

The GEOS-Chem CTM implementations use archived ("offline") inventories of natural emissions, calculated at native resolution using the NASA GEOS MERRA-2 and GEOS-FP meteorological fields. This ensures that the emissions are calculated consistently regardless of grid resolution. These archived emissions fields can be used within CESM but we also preserve the option for users to employ "online" emissions inventories where relevant. This enables feedback between climate and emissions to be calculated. For instance, lightning nitrogen oxides (NO_x = NO + NO_2) emissions, dust and sea salt emissions, and biogenic emissions are all computed online using parameterizations from CAM and CLM. CAM computes lightning NO_x emissions based on the lightning flash frequency, which is estimated following the model cloud height, with different parameterizations over ocean and land. The NO lightning production rate in CAM is assumed proportional to the discharged energy, with 10^{17} atoms of nitrogen released per Joule (Price et al., 1997). The lightning NO_x emissions are then allocated vertically from the surface to the local cloud top based on the distribution described by Pickering et al. (1998). For biogenic emissions, we use the online Model of Emissions of Gases and Aerosols from Nature version 2.1 (MEGANv2.1), as established in CLM (Guenther et al., 2012). Aerosol mass and number emissions are passed directly to MAM constituents. Global anthropogenic emissions can be specified from any of the standard GEOS-Chem inventories, but default to the Community Emissions Data System (CEDS) inventory (Hoesly et al., 2018). Sulfur emissions from the CEDS inventory are partitioned into size-resolved aerosol (mass and number) and SO_2 (Emmons et al., 2020). In CAM, volcanic out-gassing of SO_2 is provided from the GEIA inventory with 2.5% emitted as sulfate aerosol (Andres and Kasgnoc, 1998), while eruptive emissions are provided from the VolcanEESM database (Neely and Schmidt, 2016). The option is also available through HEMCO to use the "AeroCom" volcanic emissions, which are derived from OMI observations of SO_2 (Ge et al., 2016; Carn et al., 2015).

Although we use HEMCO with both model configurations, there remain differences between the representation of emissions in CAM-chem and in GEOS-Chem when run within CESM. This is because of differences in the species present in their respective mechanisms. For instance, emissions of iodocarbons (CH_3I, CH_2I_2, CH_2ICl, CH_2IBr) and inorganic iodine (HOI, I_2) are not available in CAM-chem since iodine is not explicitly modeled in the versions of CAM-chem available in CESM v2.1.1. VOC lumping is also performed differently (see the Supplemental Information for more detail).

Where the emitted species are present in both chemical mechanisms, the emissions calculated by HEMCO in CESM are identical whether running with GEOS-Chem or CAM-chem. If the HEMCO implementations of lightning, dust, sea salt, and biogenic emissions are used, emissions will be identical between CESM and the standalone GEOS-Chem CTM.

2.3.4. Wet deposition and convection

For both GEOS-Chem and CAM-chem within CESM, convective scavenging and transport are handled separately. Unlike in the Liu et al. (2001) approach implemented in the GEOS-Chem standalone code, removal of soluble gases within convective updrafts is not explicitly simulated in either CAM-chem or GEOS-Chem when embedded in CESM. When using the CAM-chem mechanism within CESM, the Neu scheme is used to perform washout of soluble gaseous species, while wet deposition of MAM aerosols is handled by MAM. When running CESM with the GEOS-Chem chemistry mechanism, the Neu scheme also performs wet scavenging for aerosols which are not represented by MAM4 (e.g. nitrate). For all such aerosols we assume a Henry's law coefficient equal to that for HNO_3.

2.3.5. Surface boundary conditions

In CESM, surface boundary mixing ratios of long-lived greenhouse gases (methane, N_2O, and chlorofluorocarbons) are set to the fields specified for CMIP6 historical conditions and future scenarios (Meinshausen et al. 2017). For whichever CMIP6 scenario is chosen, the boundary conditions overwrite those set by the GEOS-Chem chemistry module or by the HEMCO emissions component.

2.4. Changes to the data flow in CESM when running with GEOS-Chem

In CESM, data such as the Henry's law coefficients required to calculate dry deposition velocities and wet scavenging rates for each species are defined at compile time. For species that are common to GEOS-Chem and CAM-chem but where these factors differ, the GEOS-chem values are used by default. The CAM-Chem values are listed alongside them in the source code to allow users to switch if desired. Additionally, we modify CAM, CLM and the Common Infrastructure for Modeling the Earth (CIME) such that the land model can pass land type information and leaf area indices to the atmosphere model to compute dry deposition velocities. This could be a potential solution for dry deposition of aerosols in MAM, which currently uses fixed land types independent of the ones used in CLM (Liu et al., 2012). However, this comes at the cost of passing land information through the coupler at every time step.

2.5. Installation and compilation process

The interface between CESM and GEOS-Chem, as well as the GEOS-Chem source code, is automatically downloaded when CAM checks out its external repositories. The versions of GEOS-Chem and of the coupling interface can be changed by modifying the `Externals_CAM.cfg` and by running the `checkout_externals` command.

When creating a new case, the user chooses the atmospheric chemistry mechanism (GEOS-Chem or CAM-chem). The chemistry option is defined by the name of the CESM configuration (component set, or "compset"), making the process of creating a run directory almost identical when choosing either GEOS-Chem or CAM-chem. Whereas chemistry options in CAM-chem are set explicitly using namelist files, certain options in GEOS-Chem are set using ASCII text input files which are read during the initialization sequence. The installation and build infrastructure of CIME will therefore copy any GEOS-Chem specific text input files to the case directory when setting up a simulation which includes GEOS-Chem. This currently includes emissions specifications read by HEMCO, although this is expected to change as HEMCO becomes the standard emissions option for both CAM-chem and GEOS-Chem in CESM (currently being discussed with the CESM team).

Although CESM supports both shared-memory parallelization (OpenMP) and distributed memory parallelization (MPI), GEOS-Chem implemented in CESM does not currently support OpenMP. When running CESM with the GEOS-Chem chemistry model, the number of OpenMP threads per MPI task is therefore set to one.

Although a complete copy of the GEOS-Chem source code is downloaded from the version-controlled remote of GEOS-Chem repository (to ensure that the most-recent release of GEOS-Chem is used), not all files present in the GEOS-Chem source code directory are compiled. For instance, the files pertaining to the GEOS-Chem advection scheme are not needed as advection is performed by CAM, and therefore the GEOS-Chem advection routines are not compiled. To do this we implement a new feature in CIME to use `.exclude` files which list files not needed during compilation. CIME reads each `.exclude` file at compile time and searches subdirectories recursively from the location of the exclude file, preventing any named file from being included in compilation. For example, an `.exclude` file is provided in the chemistry coupling interface folder for GEOS-Chem that lists the files to exclude in the GEOS-Chem source code directories.

3. Setup used for model evaluation

We simulate a two-year period with GEOS-Chem embedded in CESM (hereafter C-GC). The simulation setup is described in the present Section. Then, we perform a comparison of its output to that generated by two other model configurations (Section 4). By comparing the results to those produced for the same period by CESM with CAM-chem (hereafter C-CC), we can perform the first comparison of GEOS-Chem and CAM-chem when run as chemistry modules within the same ESM. Any differences between these two simulations can only be the result of differences between the two chemical modules and their implementations in CESM. This includes not only differences in the gas-phase chemical mechanism, but also in the implementation of photolysis calculations, heterogeneous chemistry, aerosol microphysics, and the chemical kinetics integrator itself. We also compare output to that produced by the standalone GEOS-Chem High Performance model (hereafter

S-GC). This enables us to evaluate the effect of using CESM's grid discretization, advection, aerosols, and representation of meteorology compared to that used in the GEOS-Chem CTM.

Lastly, we evaluate the performance of C-GC by comparing output to observational data (Section 5). We also include comparisons of data from the C-CC and S-GC configurations, to provide insight into the relative performance of the model and the root cause of disagreements with observations. This section describes the model configurations in detail, but a brief summary is provided in Table 6.

All simulations cover January 1st to December 31st 2016, with an additional 6 months (S-GC) or 1 year (C-GC/C-CC) of spin up. For C-CC, the standard restart file provided with CESM is used to provide initial conditions. For S-GC, we use a restart file provided with version 13.1.2 of the GEOS-Chem chemistry module, which was obtained from a 10-year simulation. The CESM restart file is intended to represent the early 21st century, so we have followed the lead of previous studies which have used a 1-2 year spin up period (Schwantes et al., 2022; He et al., 2015). For C-GC, we use initial conditions which are taken from the S-GC restart file where possible, but fill missing species (e.g. MAM4 aerosol tracers) using data from the C-CC restart file. Both simulations performed with CESM v2.1.1 (C-GC and C-CC) use a horizontal resolution of 1.9°×2.5° on 56 hybrid pressure levels, extending from the surface to 1.65 hPa. Aerosols are represented in CESM using the 4-mode version of the modal aerosol model, MAM4 (Liu et al., 2012). In C-GC, we use the complex SOA chemistry scheme (Pye and Seinfeld, 2010; Pye et al., 2010; Marais et al., 2016). In C-CC, we use the MOZART-TS1 chemistry scheme (Emmons et al., 2020).

Standalone GEOS-Chem (S-GC) simulations are performed using the GEOS-Chem High Performance (GCHP) configuration, using a C48 cubed-sphere grid (approximately equivalent to a 2°×2.5° horizontal grid) on 72 hybrid pressure levels extending up to 0.01 hPa. In GCHP, chemistry is performed up to 1 hPa (approximately 50 km) with simplified parameterizations used above that point. Aerosols are represented using GEOS-Chem's "native" scheme, without translation to or from MAM4. As in C-GC, we use the complex SOA scheme.

All three model configurations are driven using meteorological data from MERRA-2. In S-GC all meteorological fields are explicitly specified by MERRA-2, using the same 72-layer vertical grid. The only exception is the specific humidity in the stratosphere, which is computed online. In C-CC and C-GC, we use the "specified dynamics" (SD) configuration of CAM6 in which 3-D temperature, 3-D wind velocities, surface pressure, surface temperature, surface sensible heat flux, surface latent heat flux, surface water flux, and surface stresses are provided by MERRA-2 on a truncated 56-layer vertical grid. These variables are nudged with a relaxation time of 50 hours, resulting in a relatively "loose" nudging strength. All other fields (e.g. cloud fraction) are computed using the CAM physics routines. This includes convection. Whereas S-GC computes convective transport from archived convective mass fluxes and calculates scavenging within the updraft (Wu et al., 2007), convective transport in both C-CC and C-GC is calculated in CAM6 using the CLUBB-SGS scheme for shallow convection (Bogenschutz

et al., 2013) and the Zhang-McFarlane scheme (Zhang and McFarlane, 1995) for deep convection. Scavenging within the convective updraft is not simulated explicitly.

Water vapor in C-GC is initialized from the specific humidity "Q" restart variable, which is identical to the one used for C-CC; after this point humidity is calculated based on the moist processes represented explicitly in CAM's physics package. The GEOS-Chem CTM does not calculate water vapor in the troposphere, instead prescribing specific humidity directly from MERRA-2 output. Mixing ratios of water vapor in C-CC and C-GC are therefore identical to that in S-GC at initialization time, but from that point onwards may diverge.

Emissions are harmonized between the three models, with all three configurations using HEMCO to calculate emissions fluxes. Surface anthropogenic emissions are provided from CEDS and are identical between all three models, apart from small differences in effective emissions from ships due to parameterized plume processing (Vinken et al., 2011). Simulated anthropogenic and biomass burning surface emissions of nitrogen oxides are 128-132 Tg(N) in each of the three models. Aviation emissions are calculated in all three models based on the AEIC 2005 emission inventory, contributing a further 0.8 Tg(N) in addition to other species (Simone et al., 2013).

Lightning emissions are calculated in C-CC and C-GC using the online parameterization described in Section 2.3.3, while lightning emissions in S-GC are calculated using archived flash densities and cloud top heights (Murray et al., 2012). Total lightning NO_x emissions are 5.7-6.1 Tg(N) in all three models. A summary of the breakdown of NO_x emissions is provided in Table 2.

Table 2. Annual global anthropogenic, soil, and lightning NO_x emissions expressed in Tg(N)/year.

	C-GC	**S-GC**	**C-CC**
Anthropogenic + biomass burning	40.1	39.1	39.6
Soil	7.23	7.23	7.23
Lightning	6.05	5.82	5.71

Biogenic emissions are calculated in C-CC and C-GC using the embedded MEGAN emissions module in CESM, which differs slightly from the implementation in S-GC and will produce different emissions due to different vegetation distributions. Total biogenic emissions in S-GC and C-GC are shown in Table 3. In all three simulations we use the "AeroCom" volcano emissions implemented in HEMCO.

Table 3. Annual global biogenic emission totals in GEOS-Chem implemented in CESM (C-GC) compared to in standalone GEOS-Chem (S-GC).

Species	Name in GEOS-Chem	C-GC (Tg/year)	S-GC (Tg/year)
Acetone	ACET	42.7	48.2
Acetic acid	ACTA	3.86	-
Acetaldehyde	ALD2	20.8	17.9
Lumped alkanes >= C_4	ALK4	0.16	-
Ethylene	C2H4	30.4	-
Ethane	C2H6	0.34	0.21
Propane	C3H8	0.03	-
Formaldehyde	CH2O	5.14	-
Carbon monoxide	CO	88.8	-
Ethanol	EOH	20.8	17.9
Limonene	LIMO	11.0	9.11
α/β-pinene, sabinene, carene	MTPA	98.6	81.5
Other monoterpenes	MTPO	40.8	38.6
Isoprene	ISOP	502	397.6
Methanol	MOH	119	-
Toluene	TOLU	1.57	-
Lumped alkenes >= C_3	PRPE	22.3	24.2

Emissions of aerosols (primary organic matter, and black carbon) are listed in Table 4. These emissions are consistent with the values provided in Tilmes et al. (2016).

Table 4. Annual global emissions of sulfates, primary organic matter and black carbon in all three model configurations.

	C-GC	S-GC	C-CC
SO_4 in Tg(S)/year	0.22	0.22	0.22
POM in Tg(C)/year	45.86	34.57	57.19
BC in Tg(C)/year	8.14	7.86	6.24

Mobilization of mineral dust is calculated in all three models using the DEAD scheme (Zender, 2003). In C-CC and C-GC, the online implementation in CESM is employed, resulting in total natural mineral dust emissions of 5984 Tg/year. A brief discussion of dust emissions in CESM is provided in the Supplementary Information. In S-GC, natural mineral dust emissions

are calculated online using the same scheme but with a different scaling and at a slightly different grid resolution, resulting in total emissions of 1390 Tg/year.

Emissions of sea salt are calculated online in CESM for C-GC and C-CC, while S-GC uses a pre-calculated (offline) inventory of sea-salt emissions, as well as sea-salt bromine and chloride. Emissions of sea-salt bromine in C-GC are calculated based on the offline inventory rather than the calculated emissions of sea salt, and therefore do not scale correctly with the estimated sea-salt emissions from CESM (see Table 5). This will be resolved as part of future work.

Table 5. Annual global emissions of sea salt aerosols (fine and coarse) and bromine in sea salt for C-GC and S-GC. The names of the tracers used to represent these species in GEOS-Chem are provided in brackets.

Species	C-GC (Tg/year)	S-GC (Tg/year)
Fine sea-salt (SALA)	93.0	59.1
Coarse sea-salt (SALC)	2780	3576
Bromine in fine sea-salt (BrSALA)	0.166	0.126
Bromine in coarse sea-salt (BrSALC)	10.1	7.54

Finally, for long-lived species such as chlorofluorocarbons (CFCs) we use the shared socio-economic pathway 2-4.5 (SSP2-4.5) (Riahi et al., 2017) set of surface boundary conditions in both C-GC and C-CC. In comparisons against S-GC we use historical emissions from the World Meteorological Organization's 2018 assessment of ozone depletion (Fahey et al., 2018). However, this difference is unlikely to significantly affect simulation output given the short duration of the simulations.

Table 6. Brief summary of the model configuration used for C-GC, S-GC, and C-CC.

	C-GC	**S-GC**	**C-CC**
Horizontal resolution	1.9°×2.5°	C48 (~2°×2.5°)	1.9°×2.5°
Vertical levels	L56 (up to 1.65 hPa)	L72 (up to 0.01 hPa)	L56 (up to 1.65 hPa)
Aerosol microphysics	MAM4 with VBS-SOA	Bulk with VBS-SOA	MAM4 with VBS-SOA
Aerosol tracers	Mixed (S-GC for aerosol chemistry; C-CC for microphysics)	SO4, BC, OM, sea salt, dust, AERI, DMS, INDIOL, IONITA, MONITA, MOPI, MOPO, MSA, NH4, NIT, pFe, SOAGX, SOAIE, TSOA, ASOA	SO4, BC, OM (both primary and secondary), sea salt, dust
Treatment of SOA	Explicit calculation of SOA using VBS (five bins)	Explicit calculation of SOA using VBS (four bins)	Explicit calculation of SOA using VBS (five bins)
Chemistry	GEOS-Chem 13.1.2	GEOS-Chem 13.1.2	MOZART-TS1
Biogenic emissions	Online from dynamically evolving vegetation computed in CLM using MEGAN2.1	Offline from archived vegetations using MEGAN2.1	Online from dynamically evolving vegetation computed in CLM using MEGAN2.1

Original model references	This work	(Bey et al., 2001)	(Tilmes et al., 2016; Emmons et al., 2020; Lamarque et al., 2012)

4. Model intercomparison

We first compare the global distribution of ozone and aerosols between C-GC, S-GC, and C-CC. Section 4.1 evaluates the vertical and latitudinal distribution of ozone and two related species (water vapor (H_2O) and the hydroxyl radical (OH)), followed by the global distribution of ozone at the surface in each model configuration (Section 4.2). Stratospheric chemistry in GEOS-Chem is described by Eastham et al. (2014) and by Emmons et al. (2020) for CAM-chem. A similar evaluation of differences in zonal mean and surface aerosol concentrations follows (Section 4.3).

To understand the causes of these differences, we compare the global distribution of reactive nitrogen and halogen species in each model configuration (Section 4.4). When comparing halogen distributions we consider only bromine and chlorine distributions, as iodine is not simulated in this version of CAM-chem. The latest implementation of halogen chemistry in GEOS-Chem and its role in atmospheric chemistry are described by Wang et al. (2021), while its representation in CAM-chem is described by Emmons et al. (2020). Differences in the total atmospheric burden and vertical distribution of these families provides information regarding differences in removal processes. Differences in their internal partitioning (e.g. between NO_x and HNO_3) provide information regarding the representation of atmospheric chemistry.

4.1. Ozone

Figure 2 shows the annual mean mixing ratio of stratospheric ozone simulated by each of the three model configurations. At 10 hPa in the tropics, where ozone mixing ratios reach their peak, the three configurations agree to within 10% suggesting a reasonable representation of stratospheric ozone. However, near the tropopause the three configurations diverge. Comparison of C-GC to S-GC (panel b) shows mixing ratios 20% lower near the tropical tropopause but more than 50% greater in the extratropical lower stratosphere. However, C-GC simulates mixing ratios of ozone around the tropopause which are 20% lower than C-CC (panel c) at all latitudes.

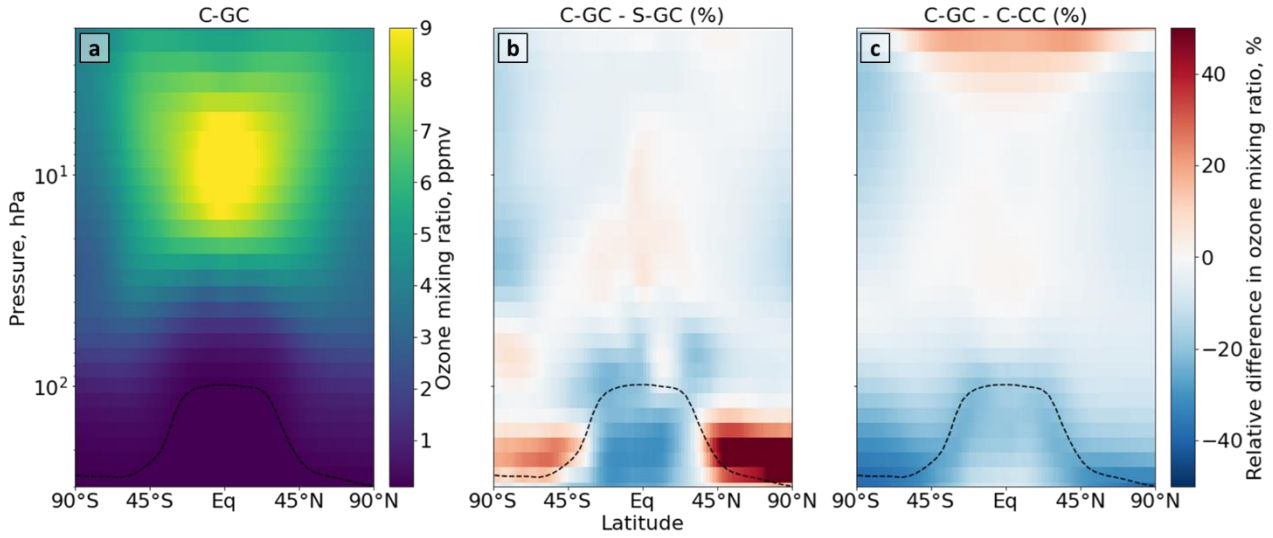

Figure 2. Comparison of stratospheric ozone simulated with CESM running GEOS-Chem (C-GC) to standalone GEOS-Chem (S-GC) and CESM running CAM-chem (C-CC). Left column (a): absolute values estimated with C-GC. Center column (b): relative difference between C-GC and S-GC. Right column (c): relative difference between C-GC and C-CC. Red (blue) shading means that C-GC estimated a higher (lower) value than the other model.

The difference in pattern in the comparison between C-GC, S-GC, and C-CC implies that the cause is likely to be related to factors which are common between C-GC and C-CC, such as the representation of meteorology. One such factor may be water vapor, which is treated differently between the "online" (C-GC, C-CC) and "offline" (S-GC) configurations.

To quantify and understand these differences in stratospheric ozone, we analyze concentrations of three different related compounds from the surface to the stratosphere: ozone, the hydroxyl radical OH, and water vapor. OH reacts with most trace species in the atmosphere and its high reactivity makes it the primary oxidizing species in the troposphere, such that differences in abundance between models will affect the simulated abundances of many atmospheric pollutants (Seinfeld and Pandis, 2006). Since OH is produced from water vapor and (indirectly) ozone, these three compounds can collectively be used to understand some of the differences between C-GC, S-GC, and C-CC. Later analyses will focus on NO_x, bromine, and chlorine, each of which also strongly affect tropospheric and stratospheric concentrations of ozone.

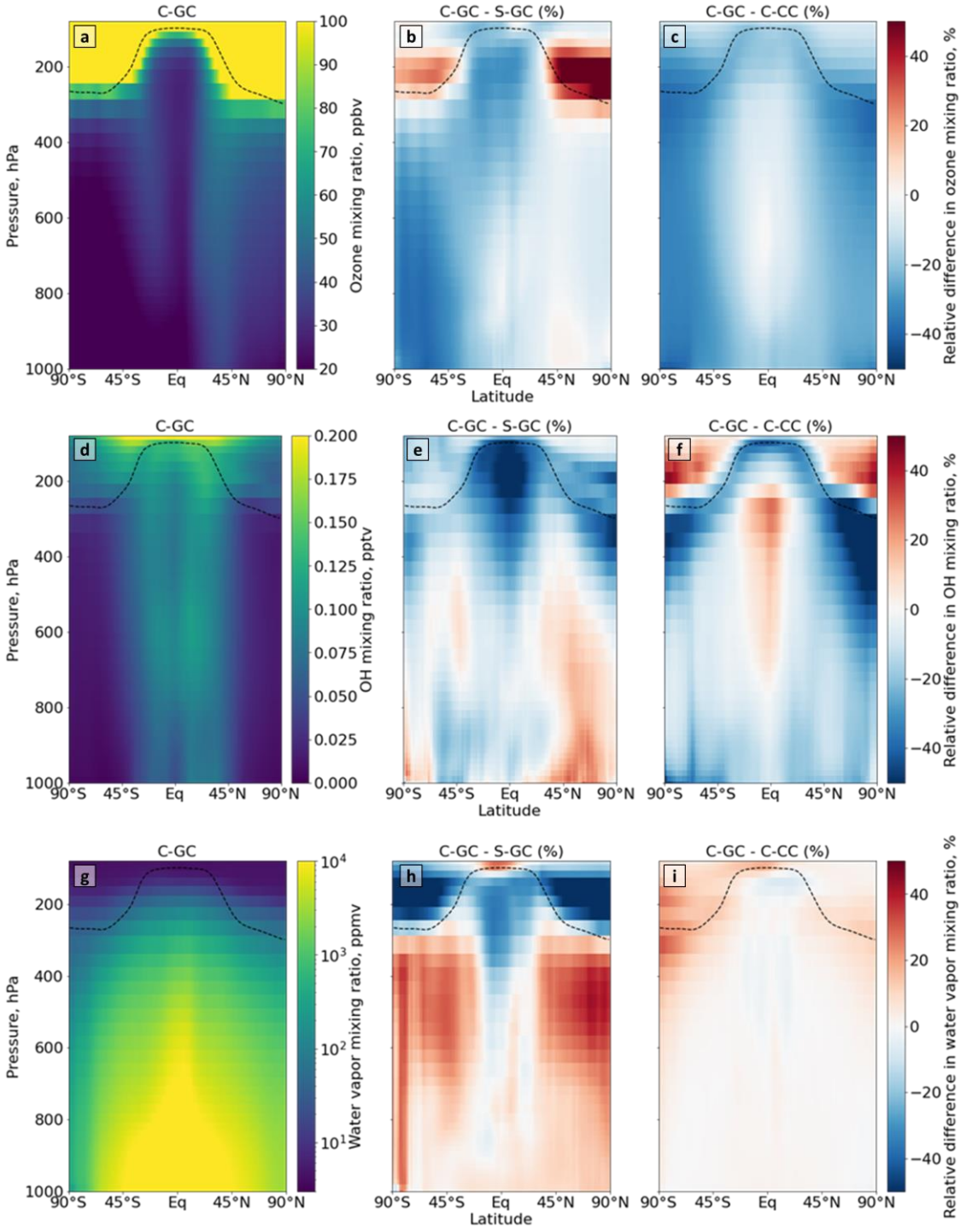

523 *Figure 3. Comparison of atmospheric composition simulated with CESM running GEOS-Chem (C-GC) to standalone GEOS-Chem (S-GC)*
524 *and CESM running CAM-chem (C-CC). Different rows show different constituents, while different columns show different model results.*
525 *Top row (a-c): ozone. Middle row (d-f): OH radical. Bottom row (g-i): water vapor. Left column (a, d, g): absolute values estimated with*

C-GC. Center column (b, e, h): relative difference between C-GC and S-GC. Right column (c, f, i): relative difference between C-GC and C-CC. Red (blue) shading means that C-GC estimated a higher (lower) value than the other model.

The upper row of Figure 3 shows the distribution of ozone as represented by C-GC (panel a), and the difference when compared to S-GC (panel b) or C-CC (panel c). Comparing to C-CC, C-GC estimates mixing ratios of ozone which are 30% lower from the surface (across all latitudes) and throughout the extratropical troposphere. This is consistent with previous work which showed that ozone simulated by GEOS-Chem to match the KORUS-AQ campaign had a normalized mean bias of -26%, compared to -9% in CAM-chem (Park et al., 2021). In the present study, we find that ozone mixing ratios around the tropopause are also lower in C-GC than in C-CC by 15-20%. This suggests that discrepancies observed in KORUS-AQ may be related to chemistry rather than the treatment of meteorology, but a more focused regional analysis would be needed to confirm this.

Comparing to the differences between C-GC and S-GC provides some insight into possible causes for these discrepancies. Near-surface ozone in C-GC in the Southern Hemisphere is also 30-40% lower than in S-GC, suggesting a potential common cause for the differences with C-CC. However, in the Northern extratropical troposphere below 400 hPa, zonal mean differences between C-GC and S-GC are consistently less than 10%. Ozone concentrations are also lower in the tropical mid-troposphere in C-GC than in S-GC by 15-25%, whereas concentrations were well matched in this region between C-GC and C-CC. In the lower stratosphere, ozone concentrations in C-GC are instead greater than in S-GC, with the difference in the Northern extratropical lower stratosphere exceeding 50%. The global ozone burden in C-GC is within 1.5% of that estimated by S-GC, while C-CC has a total atmospheric ozone burden 15% greater than C-GC. These model differences are evaluated against observations in Section 5.2.

Differences in tropospheric NO_y and halogens, in particular the higher loading of BrO in C-GC, may explain some of these differences (see Section 4.4). However, another possible factor in these differences in ozone is differences in water vapor distribution. The bottom row of Figure 3 shows the annual average simulated distribution of water vapor in C-GC, and the difference relative to S-GC and C-CC. Water vapor concentrations are approximately equal between C-GC and C-CC, since the representation of moist physics in the two models is identical. However, differences of up to 20% arise around the tropopause, possibly due in part to the different representation of stratospheric water chemistry and settling of stratospheric aerosol (including ice). This is unlikely to be due to HO_x catalytic cycles depleting ozone, as OH in this region is lower in C-GC than in S-GC (panel e) and HO_x cycles are in any case a minor contributor to ozone depletion in the lower stratosphere (Brasseur and Solomon, 2006). The greater water vapor (and therefore humidity) may instead result in faster heterogeneous chemistry, including the liberation of NO_x from HNO_3.

The differences between C-GC and S-GC are larger. Outside of the tropics and below the tropopause, water vapor concentrations are up to 30% greater in C-GC than in S-GC. Differences are smaller in the tropics, but in the tropical upper troposphere water vapor concentrations are instead 15% lower in C-GC than in S-GC. This may be part of the reason that

water vapor concentrations in the extratropical lower stratosphere are more than 50% lower in C-GC than in S-GC, since the tropical upper troposphere is the source of water vapor to the stratosphere. This is the same region in which C-GC calculates ozone mixing ratios which are more than 50% greater than in S-GC, potentially due to the lower concentration of water vapor (an indirect sink for ozone).

These differences arise due to the different representation of moist processes between CAM's physics package (used in both C-GC and C-CC), and GEOS, which produces MERRA-2 and therefore is represented in S-GC. For example, although total annual average precipitation agrees to within 10% between the models, the mean volumetric cloud fraction in C-GC and C-CC is 15%, compared to 8% in S-GC. Meanwhile the area-averaged cloud water content and cloud ice content are 57% and 38% greater in S-GC than in C-GC (or C-CC).

Differences in ozone and water vapor result in differences in concentrations of OH, as shown in the middle row of Figure 3. The global OH atmospheric burden is approximately 10% lower in C-GC than in S-GC, but this difference is not evenly distributed. Differences in OH concentrations can be roughly considered to be the product of differences in ozone and differences in water vapor, since both are needed to create OH (along with UV radiation). In the tropical troposphere, OH concentrations are more than 50% lower in C-GC than in S-GC, likely due to a relative lack of both ozone and water vapor. However, in the Northern mid- and upper latitudes below 900 hPa, OH concentrations are 10-20% greater in C-GC than in S-GC. This reflects the greater water vapor concentrations and roughly equal ozone concentrations between the two models.

4.2. Surface ozone

Figure 4 compares the simulated, annually-averaged surface ozone mixing ratios as estimated by C-GC, S-GC, and C-CC. We find that, when globally averaged, C-GC predicts a lower surface ozone mixing ratio than either C-CC or S-GC. Averaged over each Hemisphere, C-GC estimates a lower surface ozone mixing ratio than S-GC (panel b) by 4.9 ppbv and 2.2 ppbv in the Southern Hemisphere and Northern Hemisphere respectively. This varies between the land and oceans. In the Northern Hemisphere, we observe a small difference in surface ozone mixing ratio over the oceans (less than 1 ppbv), while a difference of approximately 3 ppbv can be found over North America, Europe and East Asia.

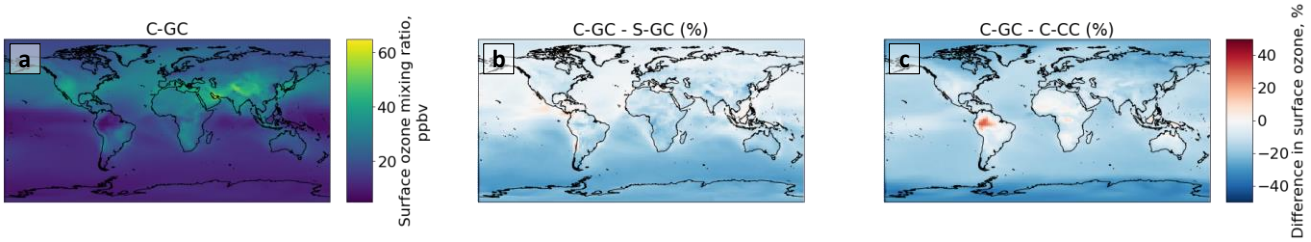

Figure 4. Comparison of the annually averaged surface ozone mixing ratios simulated with CESM running GEOS-Chem (C-GC, panel a) to standalone GEOS-Chem (S-GC, panel b) and CESM running CAM-chem (C-CC, panel c). Red (blue) shading means that C-GC estimated a higher (lower) value than the other model.

The difference between C-GC and C-CC (panel c) does not show the same hemispheric asymmetry in absolute terms, and a larger difference over oceans than over land. We find that C-GC estimates 5.4 and 7.9 ppbv less ozone than C-CC in the Southern and Northern Hemispheres respectively. The pattern indicated in Figure 4c suggests that bromine from sea salt may be the principal cause of the differences in surface ozone between C-GC and C-CC, whereas differences between C-GC and S-GC are likely to be related to anthropogenic emissions given the hemispheric asymmetry. The 20-30% increase in ozone over the Amazon in C-GC related to C-CC may instead be related to differences in biogenic emissions.

In addition to annual averages, we also consider seasonal variations of surface ozone. Figure 5 presents parity plots of monthly-averaged surface ozone mixing ratios for January and July comparing C-GC to S-GC and C-CC, after outputs from all three model configurations were remapped to a common 2°×2.5° grid. In January, we find a correlation coefficient of 0.91 and slope of 0.91 between C-GC and S-GC. In July this agreement is worsened, with a correlation coefficient of 0.80 but a slope of 0.93. This indicates that the sources of differences in surface ozone mixing ratios between C-GC and S-GC are magnified during boreal summer. There is also a distinctive "hot spot" in the July parity plot, with a large cluster of grid cells showing mixing ratios in the range 20-25 ppbv in S-GC but 10-20 ppbv in C-GC. Further research is needed to establish the origin of this cluster, which does not occur during boreal winter.

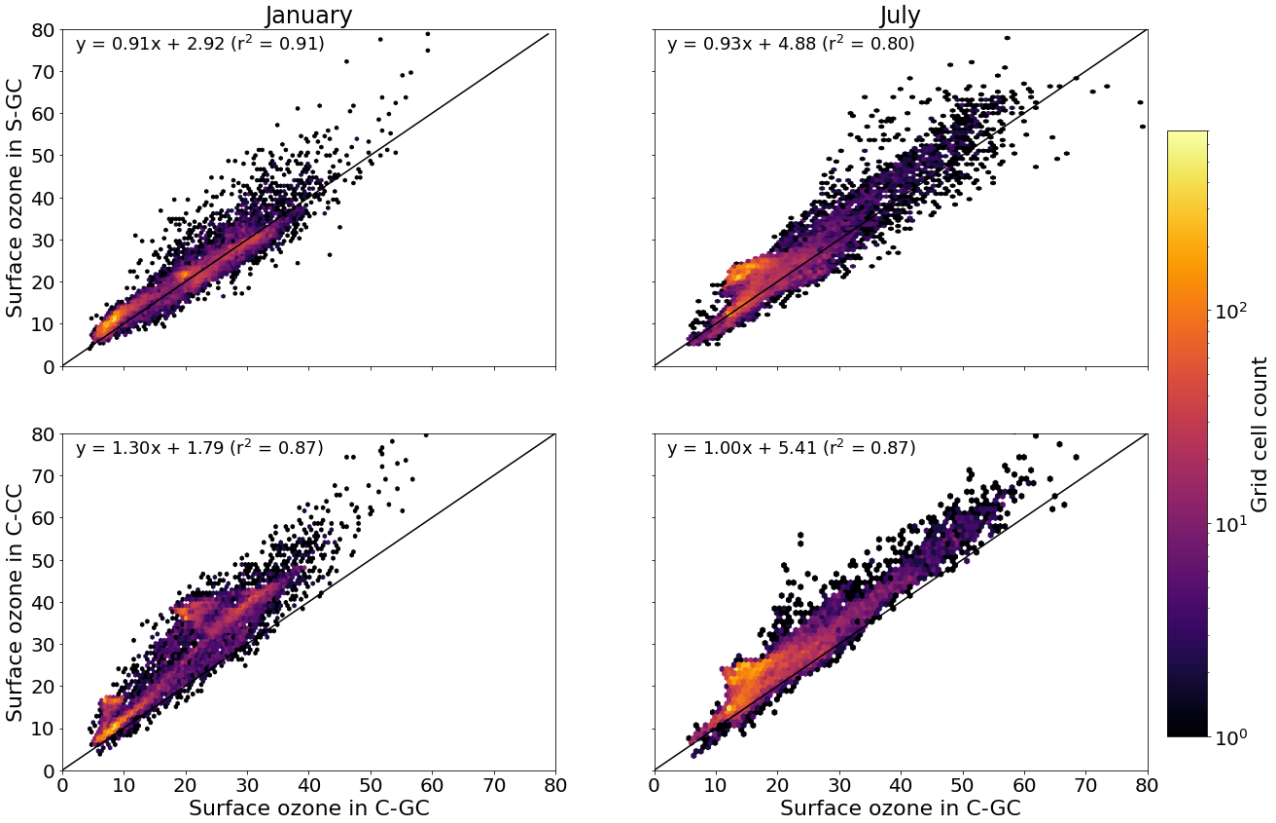

Figure 5. Parity plots of surface ozone mixing ratios, expressed in ppbv, for January (left) and July (right) comparing C-GC on the X axis to S-GC (top) and C-CC (bottom) on the Y axis. Fitting parameters are shown in the top left corner for both months. All panels share the same color scale.

Comparison between C-GC and C-CC shows a different pattern. The line of best fit between C-CC and C-GC indicates 30% greater ozone in C-CC in January than in C-GC (y ~ 1.3x), but no such normalized mean bias is present in July (y ~ 1.0x). As with the comparison of C-GC to S-GC, the absolute bias is greater in July than in January, but the correlation between C-CC and C-GC does not worsen between the two months (r^2 = 0.87). This may indicate the strength of the effect of meteorology and non-chemistry processes in the seasonality of simulated surface ozone.

4.3. Aerosols

Figure 6 shows the zonal mean mass concentration of sulfate aerosol as simulated in each of the three model configurations. In C-GC and C-CC, this is calculated as the sum across all aerosol size bins, whereas S-GC uses a bulk representation.

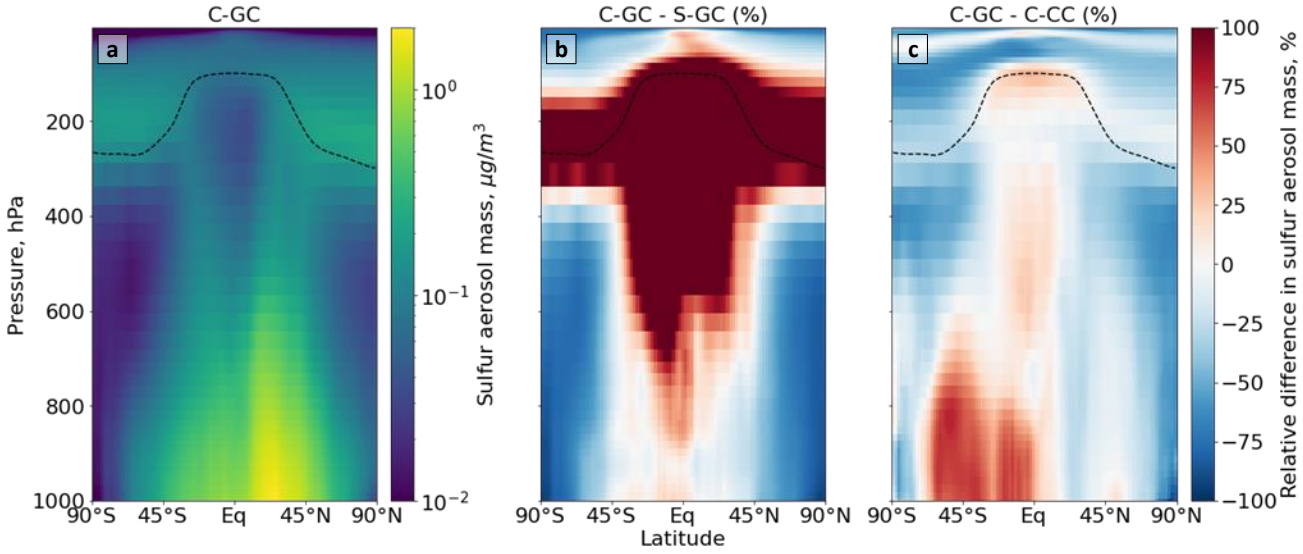

Figure 6. Comparison of sulfate aerosol mass concentration as simulated with CESM running GEOS-Chem (C-GC) to standalone GEOS-Chem (S-GC) and CESM running CAM-chem (C-CC). Left (a): absolute values estimated with C-GC. Center (b): relative difference between C-GC and S-GC. Right (c): relative difference between C-GC and C-CC. Red (blue) shading means that C-GC estimated a higher (lower) value than the other model. Differences are restricted to ±100% for clarity.

Between 45°S and 45°N, and below 800 hPa, C-GC more closely follows S-GC (comparison in panel b) with regards to sulfate aerosol mass. Compared to C-CC (panel c), sulfate aerosol mass is approximately 50% greater in southern latitudes with differences being greatest over the oceans. Sulfate concentrations in this region are dominated by oxidation of naturally-emitted dimethyl sulfide (DMS) (Seinfeld and Pandis, 2006). Since DMS concentrations are identical between the three configurations, the greater sulfate concentration in C-GC compared to C-CC may instead reflect differences in OH (Figure 3). Elsewhere the concentration of sulfate in C-GC more closely follows that in C-CC, likely due to the common representation of sulfate aerosol in MAM4 and differences in the representation of convective scavenging between CESM and standalone GEOS-Chem. Concentrations of sulfate in the tropical mid-to-upper troposphere and extratropical lower stratosphere in C-GC exceed those in S-GC by over 100%, whereas comparison to C-CC show differences of ±25%.

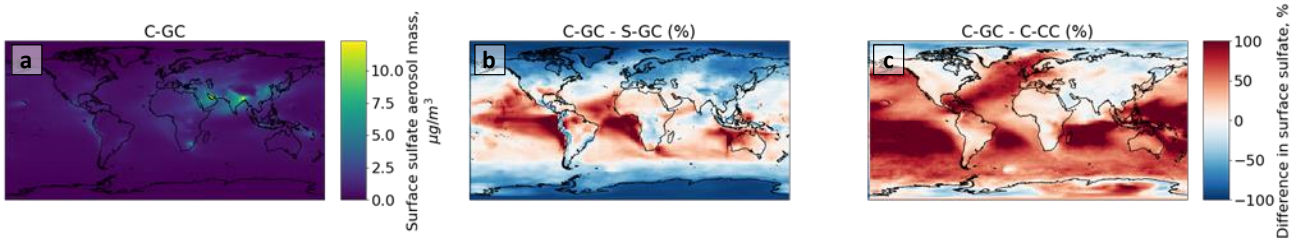

Figure 7. Comparison of the annually averaged surface mass concentration of sulfate aerosol simulated with CESM running GEOS-Chem (C-GC) to standalone GEOS-Chem (S-GC) and CESM running CAM-chem (C-CC). Red (blue) shading means that C-GC estimated a higher (lower) value than the other model.

This is further illustrated in Figure 7, which shows the surface concentration of sulfate aerosol in each model configuration. C-GC simulated greater concentrations in the intertropical convergence zone (off the west coast of Southern Hemisphere continents) than in S-GC (panel b), but in these regions agrees more closely with C-CC (panel c). Elsewhere in the tropics the agreement between C-GC and S-GC is stronger, whereas surface concentrations of sulfate aerosol over (e.g.) the Southern Pacific exceed those in C-CC by over 100%. At high latitudes and over land the agreement between C-GC and C-CC is again stronger than in S-GC, although this varies by location. Further work would be needed to identify the underlying causes leading to differences in surface sulfate concentrations between all three models.

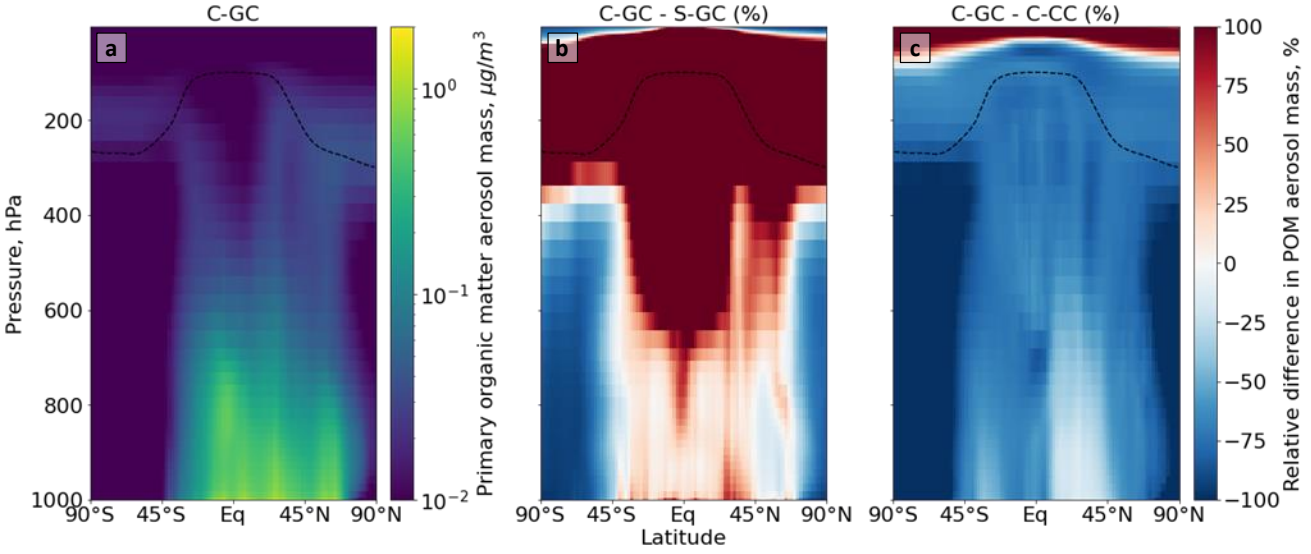

Figure 8. Comparison of primary organic matter aerosol mass concentration as simulated with CESM running GEOS-Chem (C-GC) to standalone GEOS-Chem (S-GC) and CESM running CAM-chem (C-CC). Left: absolute values estimated with C-GC. Center: relative difference between C-GC and S-GC. Right: relative difference between C-GC and C-CC. Red (blue) shading means that C-GC estimated a higher (lower) value than the other model.

We also show the zonal mean concentrations of primary organic matter (POM) aerosol in each configuration (Figure 8). POM in C-GC and C-CC is calculated as the sum of the POM aerosol size bins, whereas in S-GC it is the sum of the hydrophobic and hydrophilic organic carbon species. As with sulfate aerosol, C-GC and S-GC agree to within 25-50% in the tropics below

800 hPa, but C-GC simulates concentrations of POM which are over 100% greater than S-GC in the mid- and upper tropical troposphere and throughout the lower stratosphere. This is again likely due to differences in the representation of convective scavenging. C-GC also simulates concentrations of POM which are lower than C-CC throughout the entire troposphere. This is likely due to differences in the implementation of POM emissions between C-CC and C-GC, where emissions of POM in C-CC are 29% lower and occur as accumulation-mode rather than primary organic mode aerosol.

4.4. Reactive nitrogen (NO_y), bromine (Br_y), and chlorine (Cl_y)

To better understand the source of differences in ozone and aerosols described above, we now investigate differences in reactive nitrogen (NO_y) and halogen families (Br_y and Cl_y).

4.4.1. Reactive nitrogen (NO_y)

We compare the total concentration and partitioning of reactive nitrogen species in each model configuration, including NO_x and its reservoir species (collectively NO_y). A full list of the species included in the lumped NO_y reservoir species can be found in the legend of Figure 10 for each model configuration. We first compare results in the stratosphere, followed by an evaluation of concentrations and partitioning below 100 hPa. Concentrations of nitrate aerosol concentrations are estimated in CAM-chem using a simplified approximation (Lamarque et al., 2012), and particulate nitrate is typically not considered to be simulated by CAM-chem (e.g. Park et al. (2021)). We therefore do not include it in this analysis.

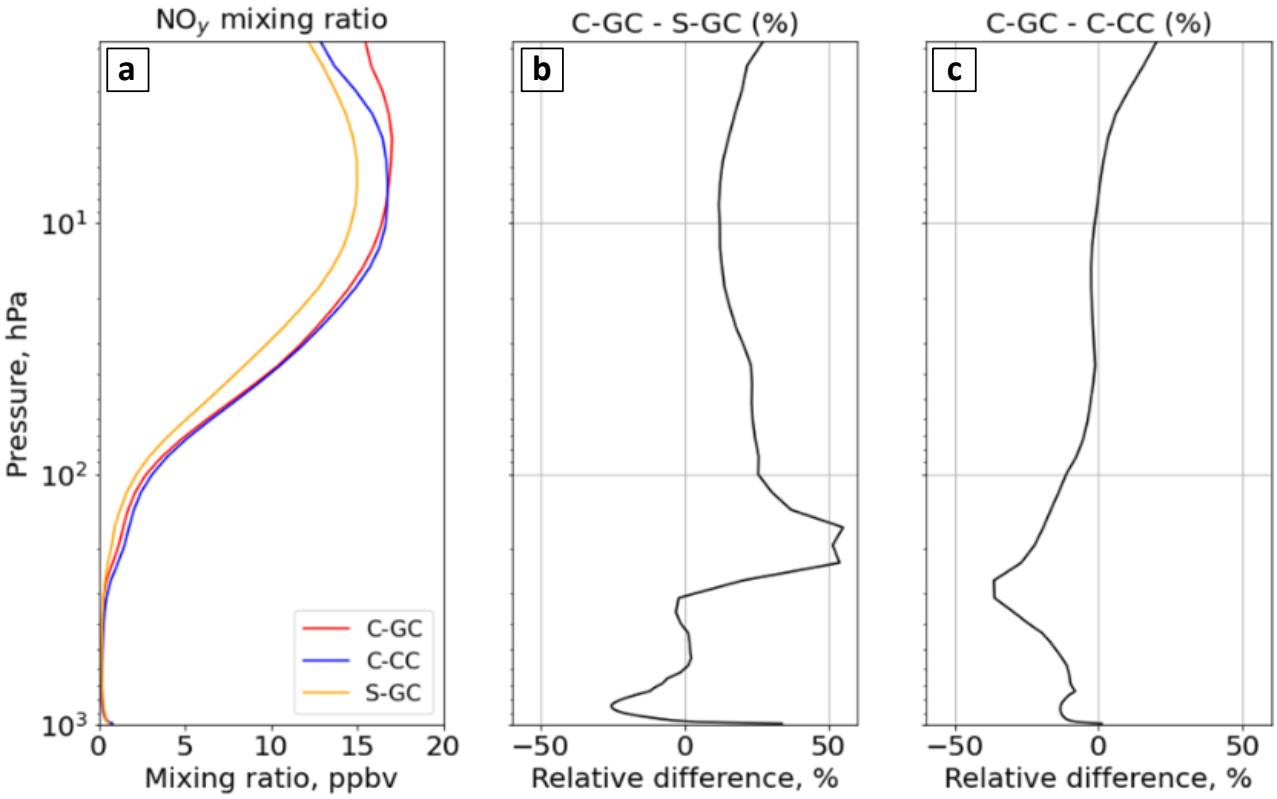

Figure 9. Global annual mean mixing ratio of total reactive nitrogen (NO_y) as a function of altitude. Left (panel a): Profile of NO_y mixing ratio for C-GC (red), C-CC (blue), and S-GC (orange). Middle (panel b): Relative difference in NO_y mixing ratio between C-GC and S-GC. Right (panel c): Relative difference in NO_y mixing ratio between C-GC and C-CC.

Figure 9 shows global mean NO_y at each altitude for C-GC, C-CC, and S-GC. Comparing C-GC to S-GC (panel b), differences in total NO_y are less than ±50% at all altitudes. Between 100 and 10 hPa, C-GC differs from S-GC by less than 20%, compared to less than 10% with respect to C-CC (panel c). The difference between C-GC and C-CC increases from -2% at 10 hPa to +20% at the top of the model, compared to an increase from 10% to 25% when comparing C-GC to S-GC. At lower altitudes C-GC more closely follows C-CC than S-GC, with differences between C-GC and S-GC exceeding 50% between 200 and 300 hPa. The global NO_y burden in C-GC (2.74 TgN) is closer to that in S-GC (2.84 TgN) than C-CC (3.01 Tg), likely due to the stronger influence of the troposphere on this quantity.

Figure 10 shows the speciation of NO_y as a function of altitude in each model from the surface to 1 hPa. The list of species defined collectively as NO_y differs between C-GC and S-GC on one side and C-CC on the other side. At altitudes above 100 hPa, the dominant contributors to NO_y in all three model configurations are NO, NO_2, HNO_3, and N_2O_5, although $ClNO_3$ contributes significantly between approximately 80 and 5 hPa. Between 10 and 200 hPa ratios of NO to NO_2 are approximately consistent between the models, lying in the range 0.35 to 0.50. This suggests broad consistency in actinic flux and ozone concentrations, given their role in controlling NO:NO_2 ratios in the stratosphere (Cohen and Murphy, 2003).

By contrast, partitioning between NO_x and HNO_3 differs significantly between the three models. At 10 hPa, HNO_3 constitutes 20% of total NO_y in C-GC but 23% in both C-CC and S-GC (values not shown explicitly). This fraction increases with decreasing altitude at differing rates. At 200 hPa, HNO_3 constitutes 60 and 63% of NO_y in C-GC and S-GC respectively, but 78% of NO_y in C-CC. One possible cause of these discrepancies is heterogeneous chemistry. GEOS-Chem (in both S-GC and C-GC) uses a different representation of N_2O_5 hydrolysis than CAM-chem, but the CESM-driven simulation includes a more detailed representation of the sulfate aerosol size distribution through MAM4. The present study did not include the analysis of aerosol reactive tendencies. This would be a valuable line of inquiry for future comparisons of CAM-chem and GEOS-Chem, given the lack of nitrate aerosol in the former.

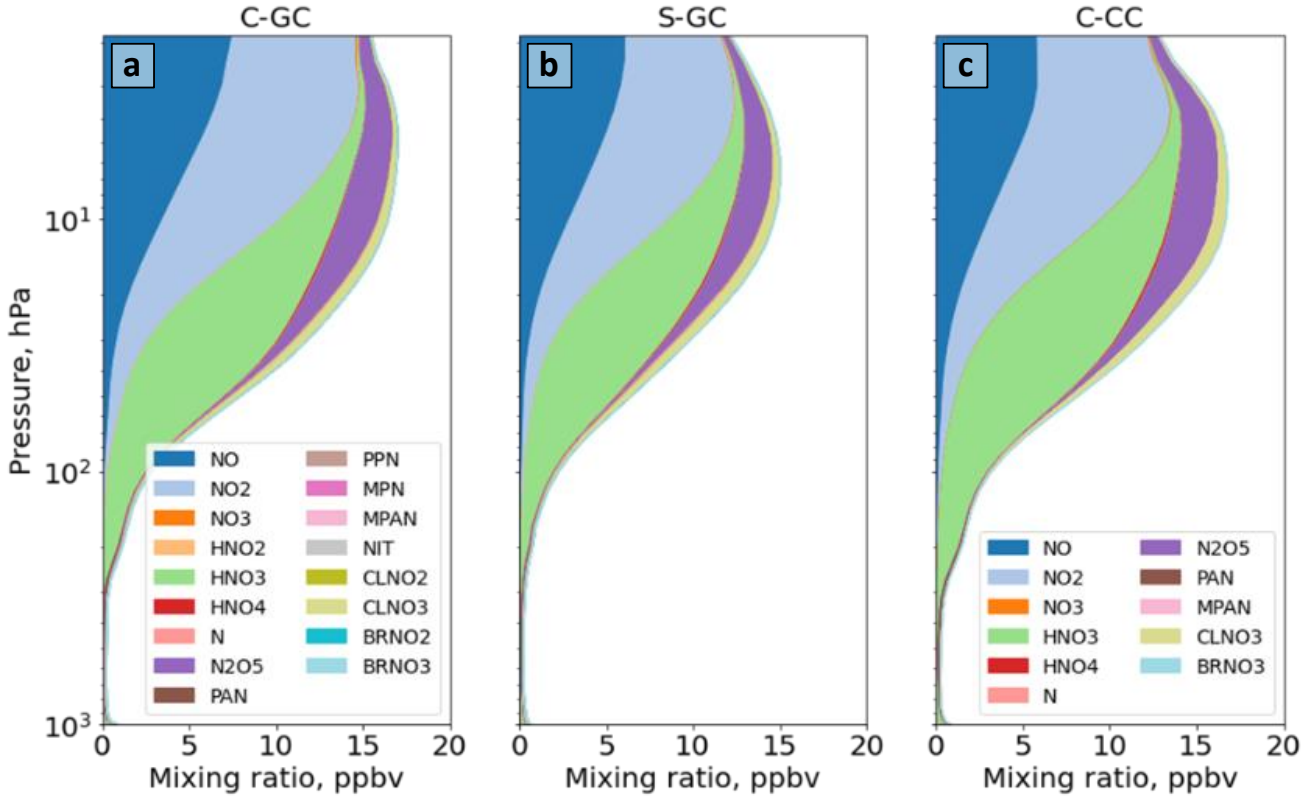

Figure 10. Global annual mean speciation of NO_y as a function of altitude. Results are shown from C-GC (left, a), S-GC (middle, b), and C-CC (right, c) from the surface up to the model top (approximately 2 hPa). Values correspond to the number of N atoms present, such that (e.g.) the mixing ratio of N_2O_5 is multiplied by 2.

Figure 11 provides a closer look at the speciation of NO_y at altitudes below 100 hPa. NO_y at altitudes below 200 hPa is predominantly NO_x, HNO_3, and peroxyacetyl nitrate (PAN). At 200 hPa, the combination of NO_x, HNO_3, and PAN make up 86% of total NO_y in C-GC (panel a) and 84% in S-GC (panel b), but 96% in C-CC (panel c). However, between 200 and 900 hPa the dominant contributors are HNO_3 and PAN. In this pressure range, the C-GC and S-GC simulations also show a significant contribution from nitrate aerosol (NIT) and $BrNO_3$. At 500 hPa, the contributions of NO_x, HNO_3, and PAN are

78%, 85%, and 97% respectively for C-GC, S-GC, and C-CC. Below 900 hPa, NO and NO_2 once again become significant contributors to total NO_y. At these lower altitudes C-GC more closely follows C-CC than S-GC, with differences in total NO_y between C-GC and S-GC exceeding 50% between 200 and 300 hPa. As such, we find that the speciation in C-GC more closely follows that in S-GC at lower altitudes.

Since surface emissions of NO_x are nearly identical between the three configurations (see Table 2) and lightning NO_x emissions are identical between C-GC and C-CC, differences below 100 hPa may instead be related to NO_x chemistry, and nitrate aerosol. However, concentrations of PAN in C-GC more closely follow C-CC than S-GC, suggesting that the representation of meteorology (including wet deposition rates) is also an important factor. At 500 hPa, total PAN in C-GC is 3% lower than the value in C-CC, but exceeds the value in S-GC by 38%. This may be due to the greater emissions of biogenic VOCs in CESM than in the standalone GEOS-Chem (see Table 3Table 3), resulting in more NO_x being bound into PAN for long-range transport. We also find that HNO_3 concentrations in the mid-troposphere are lower in C-GC than in either C-CC or S-GC. At 500 hPa, HNO_3 mixing ratios in C-GC are 43% lower than in S-GC and 52% lower than in C-CC. This does not account for the conversion of HNO_3 in C-GC and S-GC to nitrate aerosol (NIT), which is not represented in C-CC.

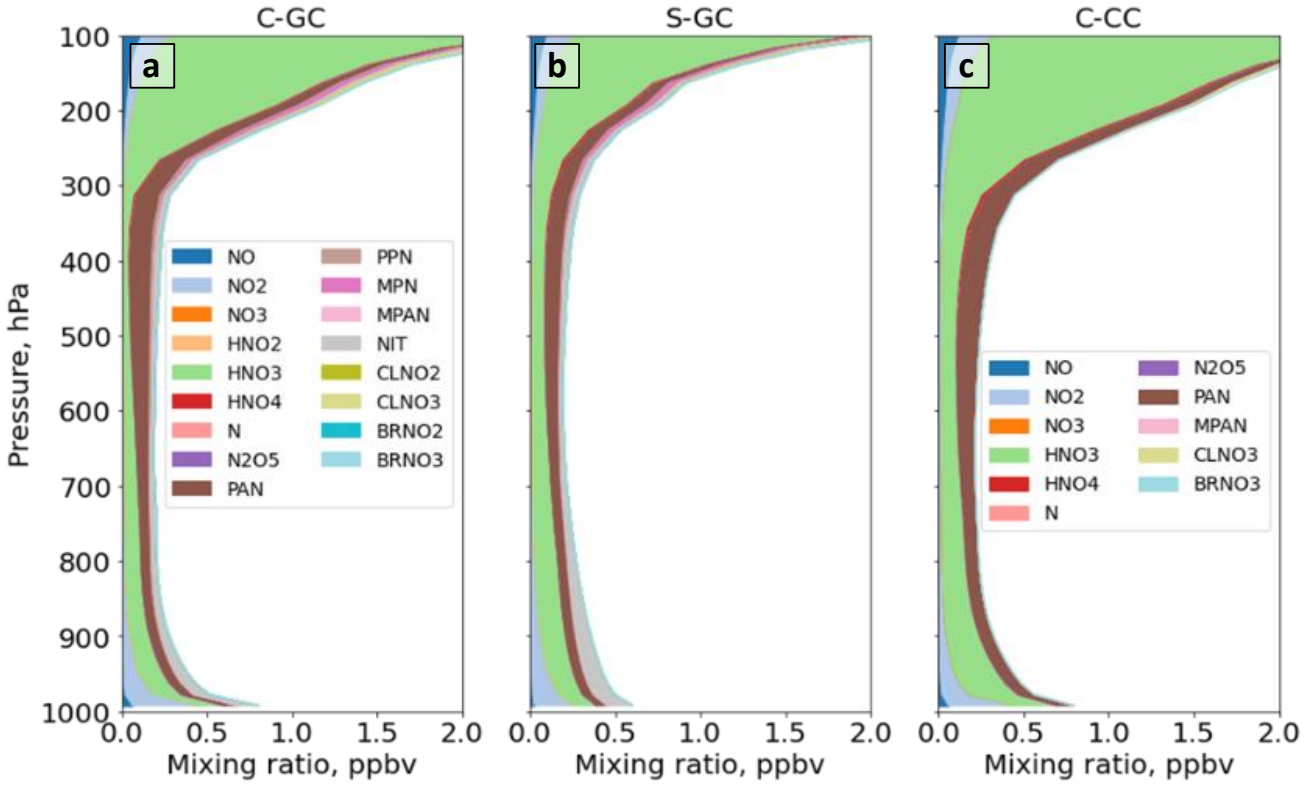

Figure 11. As in Figure 10, but showing only the 10^3-10^2 hPa pressure range.

Differences in mid-tropospheric HNO_3 between the models are most likely due to differences in the representation of wet scavenging. In C-CC and C-GC, scavenging of gaseous species is handled by the Neu scheme, while scavenging of modal aerosols is performed by MAM (Neu and Prather, 2012). Any aerosol species not handled by MAM, such as nitrate in C-GC, are also scavenged using the Neu scheme. In C-GC and C-CC, the Neu scheme calculations are performed at the same time as the chemistry and after convective transport, while scavenging of MAM aerosols is performed before. Thus, all species that undergo wet deposition in the Neu scheme are not removed during convective transport. This leads to soluble species and aerosols being carried to higher altitudes without being convectively scavenged. We also find that the Neu scavenging scheme in C-GC and C-CC results in an HNO_3 wet removal rate which is four times higher in C-GC than in S-GC (Figure S1 of the Supplementary Information). This likely explains the greater depletion of HNO_3 in the mid-troposphere calculated by C-GC compared to S-GC. Wet scavenging in C-CC is faster yet, with HNO_3 wet removal rates approximately six times greater than in S-GC, and 50% greater than in C-GC. This is in part because the mixing ratio (or fraction of total NO_y) of HNO_3 in the mid- and upper-troposphere as modeled in C-CC is greater than in either C-GC or S-GC, but also because C-GC and S-GC simulate nitrate aerosol explicitly. The application of the Neu scheme to remove nitrate aerosol also affects removal of total NO_y in C-GC (Figure S2 in the Supplementary Information). We find that the Neu scheme removes aerosol more rapidly than the scheme used in S-GC, and at lower altitudes.

Total HNO_3 removal tendencies in each model configuration are shown in Table 7. The total removal rate of NO_3^- is lowest in S-GC and highest in C-CC, consistent with the finding that total NO_y burdens are lower in S-GC than C-GC or C-CC. However, the removal rate of nitrate aerosol is lower in C-GC than in S-GC despite the greater wet removal rates for C-GC. A possible explanation is that washout rates of nitrate aerosol are sufficiently high in both C-GC and S-GC that all nitrate aerosol is effectively removed, but that the faster washout of HNO_3 in C-GC results in less nitrate aerosol being available for removal.

Table 7. Total wet removal tendency of HNO_3 and nitrate aerosol in each model configuration. All values are given in units of Tg NO_3/yr.

	C-GC	S-GC	C-CC
HNO_3	82.0	71.3	119.6
Nitrate aerosol	20.4	22.7	-
Total NO_3^-	102.4	94.0	119.6

4.4.2. Reactive bromine (Br_y)

Halogens are involved in multiple catalytic ozone-depleting chemical cycles, and are critical to an accurate description of both tropospheric and stratospheric chemistry (Solomon et al., 2015). We therefore analyze the abundance and speciation of the two key halogens – bromine and chlorine – in each configuration. Figure 12 shows the annual average mixing ratio of total reactive bromine as a function of altitude in each of the three models. This does not include long-lived species such as halons or CH_3Br. A full listing is included in the legend of Figure 13.

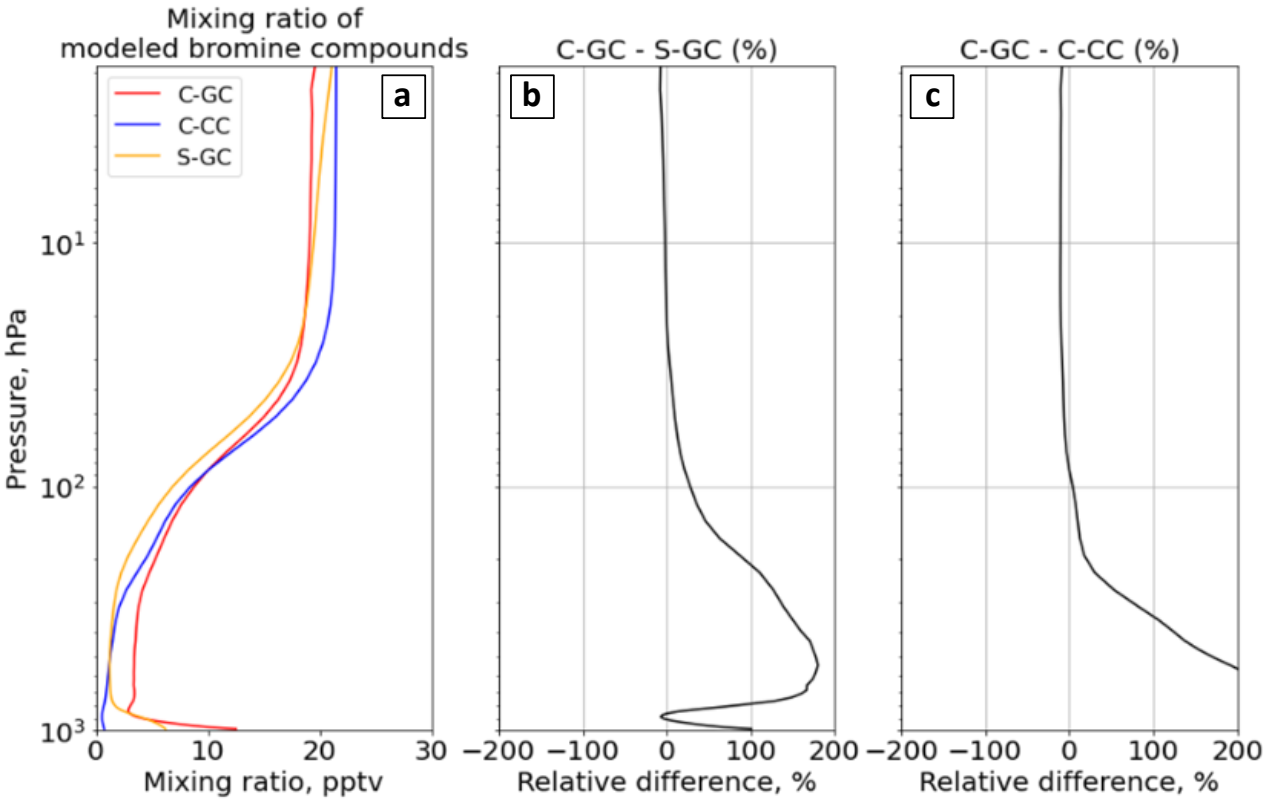

Figure 12. Global annual mean mixing ratio of reactive bromine as a function of altitude. Left (panel a): Profile of total gaseous inorganic and organic bromine mixing ratio for C-GC (red), C-CC (blue), and S-GC (orange). Middle (panel b): Relative difference in bromine-containing species mixing ratio between C-GC and S-GC. Right (panel c): Relative difference in bromine-containing species mixing ratio between C-GC and C-CC. Although relative differences between C-GC and C-CC exceed 1000% near the surface, the limits on the rightmost panel are clipped to allow comparison to the center panel.

Globally averaged total Br_y in C-GC is maximized at the surface, exceeding that from S-GC by 100%. This is partially explained by the greater emissions of sea salt bromine, although C-GC's annual emission of sea salt bromine is only 36% greater than that in S-GC (see Table 4). Since C-CC does not include short-lived bromine sources such as sea salt bromine, the C-GC total Br_y concentration exceeds C-CC by 1000 % at the surface.

From Figure 13, we find that, in all three models, the mixing ratio increases monotonically with altitude above 800 hPa due to the reaction of CH_3Br with OH. Br_y falls sharply from 12 pptv at the surface in C-GC to 3 pptv at 900 hPa, but then increases again to 10 pptv at 100 hPa. This pattern is similar to that displayed by S-GC, although the decrease from the surface is less sharp and the absolute value lower in S-GC. Above 100 hPa, the averaged Br_y mixing ratio levels off, with values between 20 hPa and 2 hPa remaining roughly constant in the range of 16-20 pptv. This is similar to the behavior shown by C-CC but differs from S-GC, in which Br_y continues to rise with altitude – albeit more slowly. The net effect is that total Br_y in C-GC

exceeds both C-CC and S-GC below 100 hPa, but is lower than the value in either model above 10 hPa (above 80 hPa when compared to C-CC).

In addition to differences in total Br_y, the partitioning of Br_y also varies between the three models (Figure 13). The additional near-surface bromine present in C-GC and S-GC is due to the presence of Br_2 and sea salt bromine (BrSALA and BrSALC, representing bromine in fine and coarse-mode sea salt respectively). This provides a source of active bromine in the planetary boundary layer which is not represented in C-CC, but in forms which are rapidly washed out in C-GC and S-GC. The greater concentrations of Br_y near the surface as calculated by C-GC compared to S-GC are likely due to the greater emissions of sea salt bromine, as shown in Table 4.

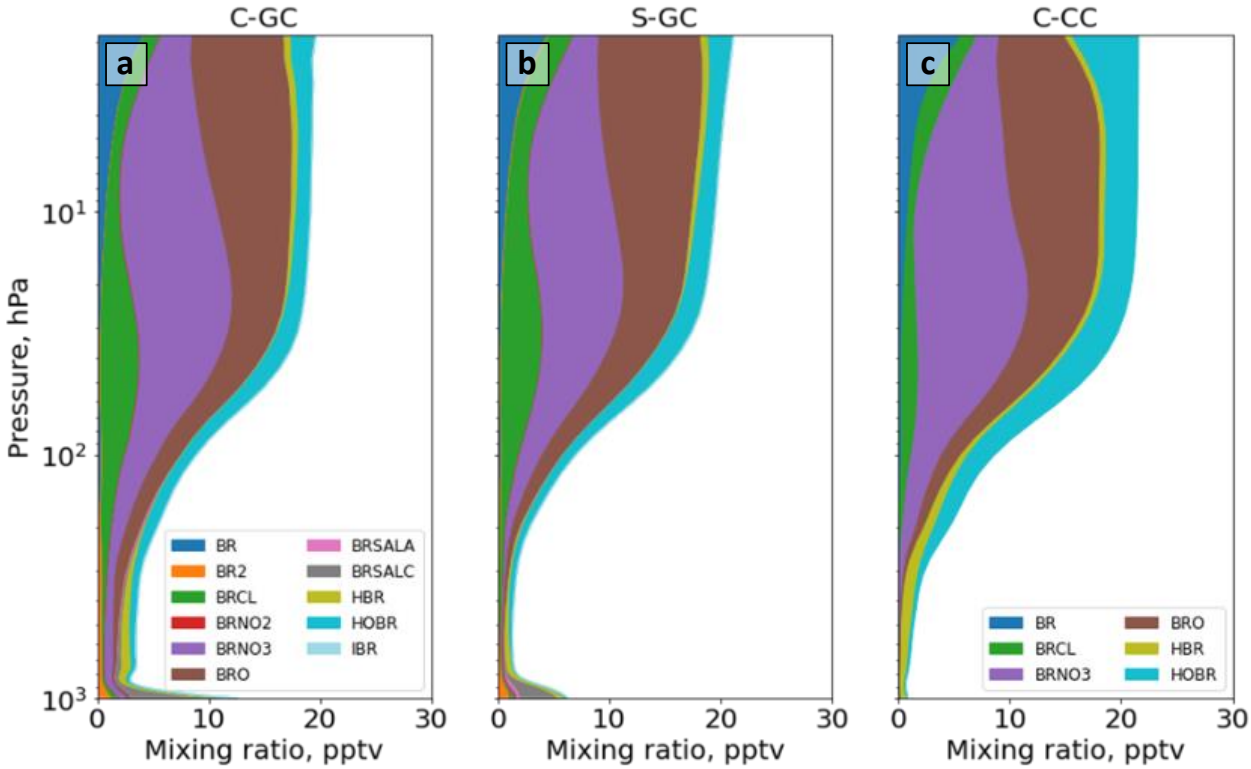

Figure 13. Global annual mean speciation of total organic and inorganic bromine as a function of altitude. Results are shown from C-GC (left, a), S-GC (middle, b), and C-CC (right, c), from the surface up to the model top (approximately 2 hPa). Values correspond to the number of Br atoms present, such that (e.g.) the mixing ratio of Br_2 is multiplied by 2.

Br_y in the model stratosphere is dominated by the same species in all three configurations: BrO_x (Br + BrO), BrCl, $BrNO_3$, HBr, and HOBr. The most significant difference is the greater proportion of HOBr in C-CC (approximately 15%) than in S-GC or C-GC (8-10%). Larger mixing ratios of $BrNO_3$ are also present in C-CC (approximately 10 ppbv at 30 hPa) compared to C-GC and S-GC (approximately 7.4 and 7.0 ppbv respectively at 30 hPa). Smaller mixing ratios of BrCl are present in C-CC, with a mean value of 1.8 ppbv at 30 hPa, while they reach 3.1 ppbv in C-GC and S-GC at 30 hPa. The base causes of

these differences are not clear, but may be related to the presence of more complex tropospheric and stratospheric halogen chemistry in the GEOS-Chem chemical mechanism (Wang et al., 2021).

Between 30 hPa and the top of the boundary layer, the three models show greater divergence. The only significant sources of atmospheric Br_y in C-CC are CH_3Br, CH_2Br_2, and very long-lived bromine species such as halons which are insoluble. As a result, tropospheric Br_y concentrations increase only slowly from the surface up to 300 hPa, at which point HOBr, BrO, and $BrNO_3$ begin to form in significant quantities. In C-GC and S-GC, these sources of bromine are supplemented by bromine from sea salt and surface Br_2 emissions. Mid-tropospheric Br_y concentrations are therefore largely set by the quantity of sea salt bromine emitted, and by the fraction of that bromine which can be released to an insoluble form (e.g. Br_2) before the sea salt is washed out of the atmosphere.

The greater concentration of mid-tropospheric Br_y in C-GC than in S-GC is likely due to differences in wet scavenging. Wet removal tendencies of bromine in fine sea salt (BrSALA) from large-scale and convective precipitation as calculated by C-GC and S-GC are shown in the Supplementary Information (Figure S3). We find that there is greater wet deposition of fine sea salt bromine in S-GC than in C-GC, despite removal rates below 900 hPa being greater in C-GC. Since total emissions of BrSALA are also 26% lower in S-GC than in C-GC (Table 4), the slower mid-tropospheric mid-tropospheric removal of bromine in C-GC explains the greater simulated concentration of Br_y in the mid troposphere.

C-GC also calculates wet deposition of non-MAM aerosols from both convective and large-scale precipitation independent of convective transport, whereas S-GC calculates convective scavenging as part of convective transport. This means that soluble species can be transported in convective updrafts in C-GC, unlike in S-GC.

4.4.3. Reactive chlorine (Cl_y)

We now focus on atmospheric chlorine by comparing its profile and partitioning in all three models. Annually-averaged vertical profiles of reactive chlorine (Cl_y) are displayed in Figure 14, excluding source species such as chlorocarbons. A full list of the species used to define Cl_y in each configuration is provided in Figure 15.

As with total Br_y, total Cl_y follows the same vertical distribution as S-GC up to 10 hPa. Above this pressure, the vertical distribution in C-GC is closer to that of C-CC. The dominant factor in differences below 100 hPa is the lack of short-lived chlorine species such as sea salt in C-CC, which are the dominant source of chlorine to the lower troposphere. Above 10 hPa, the relative difference in Cl_y between C-GC and S-GC increases slowly from -2% at 10 hPa to -5% at 2 hPa, while the difference relative to C-CC remains at approximately -20% above 200 hPa.

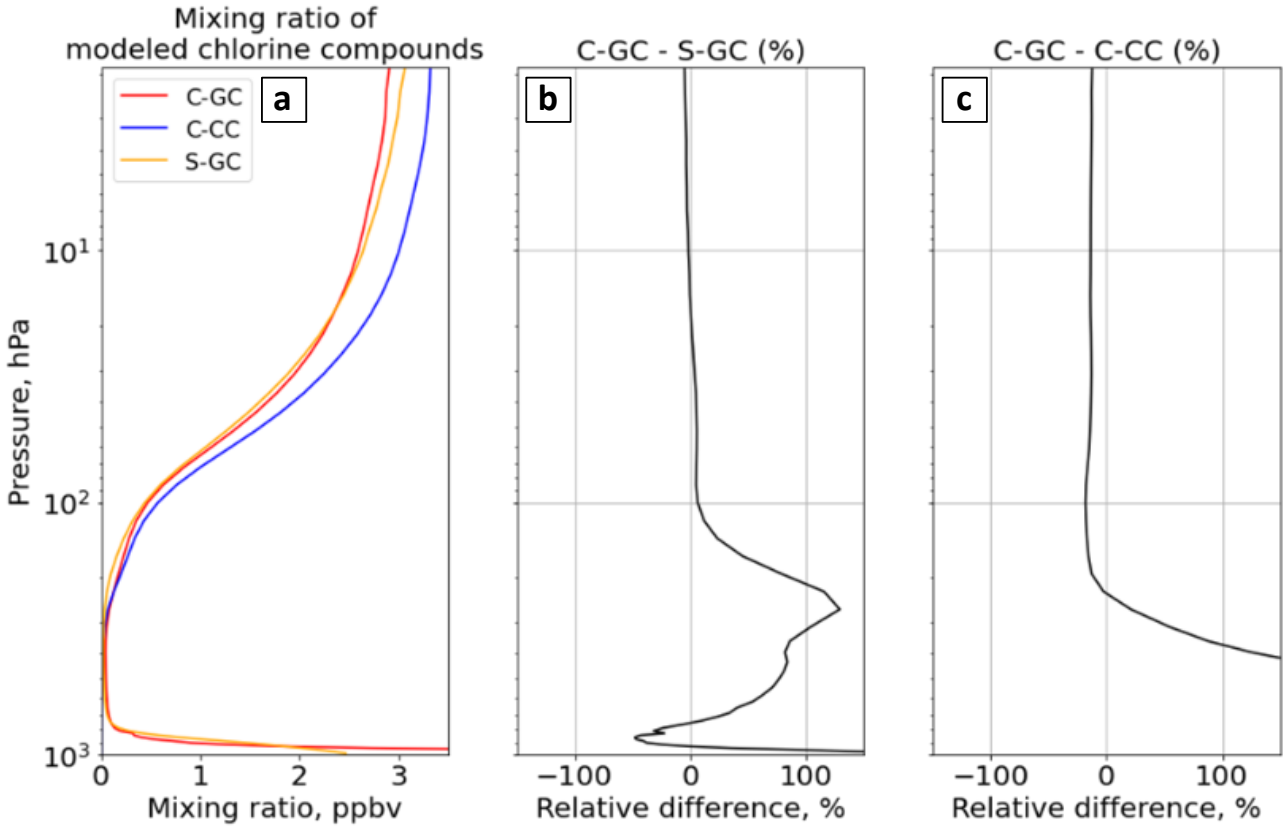

Figure 14. Comparison of annual average vertical profiles of chlorine-containing compounds in the three models. Left (panel a): Vertical profile of total gaseous chlorine mixing ratio for C-GC (red), S-GC (orange), and C-CC (blue). Middle (panel b): Relative difference in Cl_y mixing ratio between C-GC and S-GC. Right (panel c): Relative difference in Cl_y mixing ratio between C-GC and C-CC. Although relative differences between C-GC and C-CC exceed 1000% near the surface, the limits on the rightmost panel are clipped to allow comparison to the center panel.

Figure 15 shows the speciation of Cl_y as a function of altitude in each model. The greater near-surface chlorine simulated by C-GC (panel a) and S-GC (panel b) relative to C-CC (panel c) is mostly made up of HCl and chlorine in sea salt (SALACL and SALCCL). However, the short lifetime of sea salt aerosol and of chlorine in the lower troposphere means that this source is likely not significantly affecting stratospheric chlorine burdens or partitioning. In the stratosphere there is no clear difference between partitioning in C-GC and S-GC, but larger mixing ratios of upper tropospheric and lower stratospheric HCl from chlorine source compounds are found in C-CC. At 50 hPa, total Cl_y in C-CC is 15% greater than in C-GC and S-GC, but the mean mixing ratio of HCl in C-CC is 45% greater. Differences in $ClNO_3$ reach their peak at higher altitudes, around 20-30 hPa.

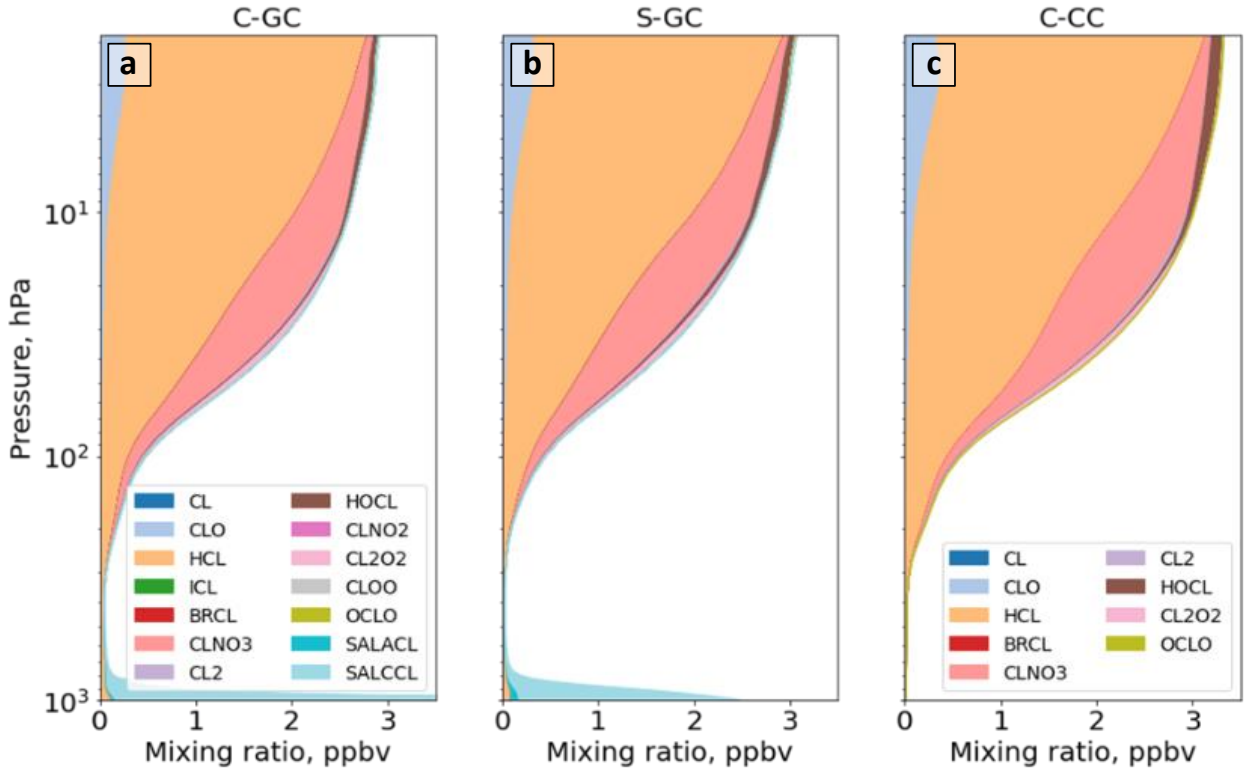

Figure 15. Global annual mean vertical speciation of total organic and inorganic bromine in C-GC (left, a), S-GC (middle, b), and C-CC (right, c) from the surface up to the model top (approximately 2 hPa). Values correspond to the number of Cl atoms present, such that (e.g.) the mixing ratio of Cl_2 is multiplied by 2. SALACL and SALCCL correspond to chlorine in fine and coarse sea salt, respectively.

The global mean tropospheric concentration of Cl atoms is 590 cm^{-3}, roughly consistent with a recent evaluation from Wang et al. (2021) which found a value of 630 cm^{-3}. This is 24% greater than the value from S-GC (477 cm^{-3}) and 160% greater than that from C-CC (224 cm^{-3}), likely due to the greater emissions of sea salt and indicating that chlorine will play a greater role in tropospheric oxidation in C-GC.

5. Comparison of model results to observations

We now compare the results from C-GC to observational data, with results from S-GC and C-CC also provided as context. Section 5.1 evaluates model performance at the surface, comparing to ground measurements of surface NO_2 and ozone. Section 5.2 compares model results to a climatology of vertical profiles of ozone, based on ozone sonde data. Section 5.3 evaluates the level of agreement of simulated ozone and carbon monoxide (CO) columns to measurements from the Aura Ozone Monitoring Instrument (OMI) and Microwave Limb Sounder (MLS), and MOPITT satellite instruments. Finally, Section 5.4 evaluates the model against measurements of dry deposition fluxes and rainwater composition measurements. The CESM wet deposition

scheme is presented in Neu and Prather (2012), while the wet deposition scheme implemented in GEOS-Chem uses different schemes for gases and aerosols (Liu et al., 2001; Amos et al., 2012). Dry deposition in GEOS-Chem is described in several publications (Wesely, 1989; Wang et al., 1998; Zhang et al., 2001), while the coupling between CAM and CLM is described in Val Martin et al. (2014) .

5.1. Surface NO_2 and ozone

Figure 16 compares surface mass concentrations of NO_2 as estimated by C-GC, S-GC, and C-CC for 2016 against ground station measurements for North America (top row), Europe (middle row), and South-East Asia (bottom row) (AirNow API, 2021; Environmental Numerical Database, 2021; China Air Quality Historical Data, 2021; European Air Quality Portal, 2021). All ground station measurements are the average value over 2016. By comparing model results at an approximately 2° horizontal resolution to point observations, we expect some differences in this evaluation due to grid-box representation errors.

All three model configurations calculate lower mixing ratios than are reported by the ground observations. This is likely to be in part due to the presence of interferants such as HNO_3, which cause in-situ monitors to overestimate the concentration of NO_2 (Dunlea et al., 2007). However, S-GC is consistently biased lower than C-GC or C-CC. We also find that the surface NO_2 concentrations display variable agreement depending on the geographical location. The correlation coefficients for North America, Europe and South-East Asia are provided in Table 8. All three models give similar correlation coefficients for each region. This is expected given that the three model configurations all use the same input wind fields and NO_x emissions datasets. Nonetheless, both C-GC and C-CC estimate higher concentrations of NO_2 in Northern China, Northern Europe, and the northeast US than S-GC. This suggests that the representation of meteorology, photolysis, and NO_y removal processes have a greater impact on simulated NO_2 than the chemistry module alone. Comparing in-situ NO_2 measurements against NO_y model results could potentially remove the effect of interferants in the observations of surface NO_2 concentrations, but is not considered here.

Table 8. Correlation coefficients of surface-level NO_2 mass concentrations for C-GC, S-GC and C-CC against measurements.

	C-GC	*S-GC*	*C-CC*
North America	0.39	0.36	0.38
Europe	0.21	0.21	0.21
South-East Asia	0.42	0.41	0.41

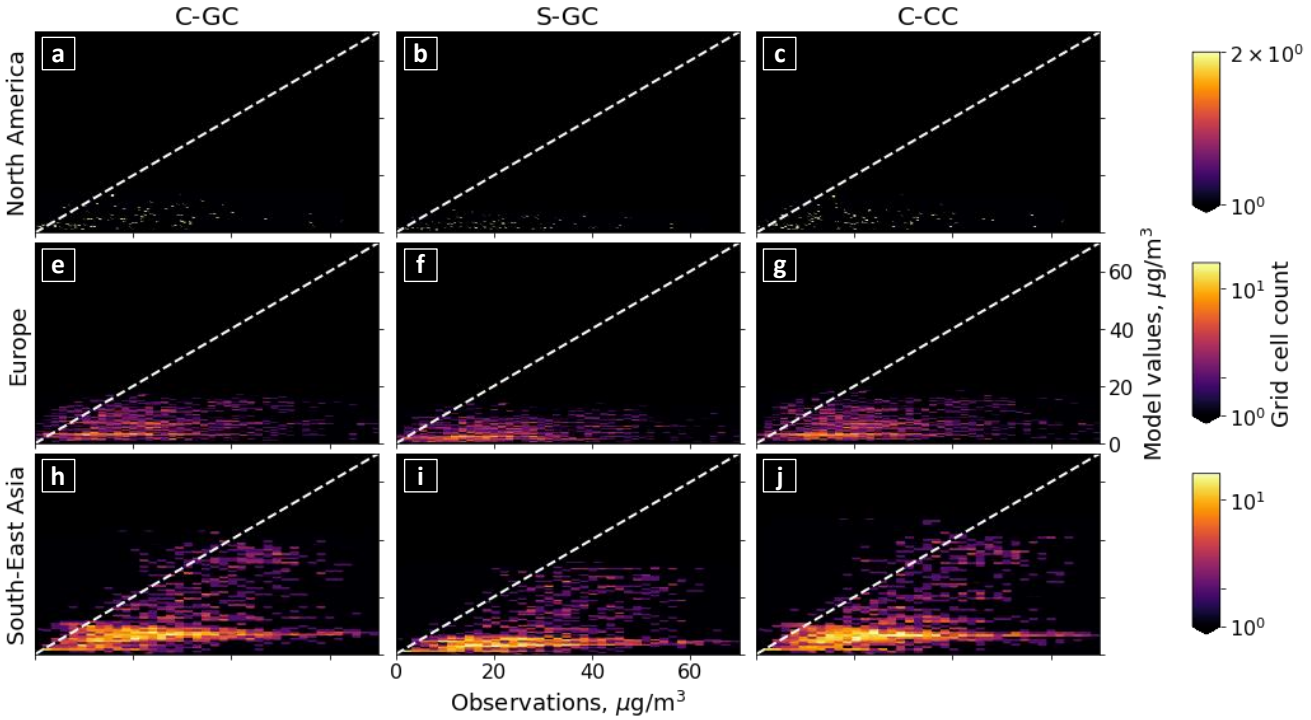

Figure 16. Annual average surface NO_2 mass concentrations simulated by C-GC (left: a, e, h), S-GC (middle: b, f, i), and C-CC (right: c, g, j) for 2016 compared against monitor measurements in North America (top: a-c), Europe (middle: d-e), and South East Asia (bottom: h-j).

Figure 17 shows the ratio of annual mean NO to annual mean NO_2, and thus provides some insight into possible causes of these disagreements. The global distribution of surface-level NO2 and NOx is presented in the Supplementary Information. All three configurations show enhanced NO:NO_2 ratios in polluted regions such as eastern China and over icy regions such as Greenland and Antarctica. However, S-GC shows reduced NO:NO_2 ratios over land compared to either C-CC or C-GC. For example, ratios over North America in S-GC range from 0.1 to 0.2, compared to a range of 0.01 to 0.1 in C-GC and C-CC. Surface NO:NO_2 ratios are typically dictated by surface ozone and the NO_2 photolysis rate (Seinfeld and Pandis, 2006). Given that surface ozone concentrations in S-GC are typically between those calculated in C-GC and C-CC (see Figure 4) and that S-GC and C-GC share the same photolysis treatment, this discrepancy may instead be caused by the differences in cloudiness calculated by CESM compared to the MERRA-2 fields read in by S-GC.

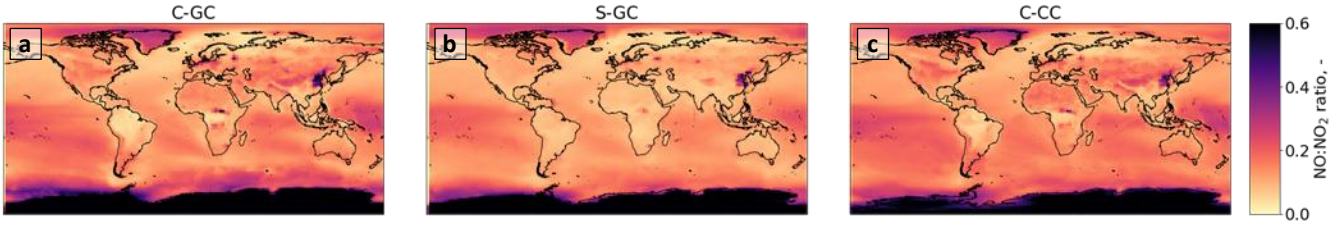

Figure 17. Surface-level $NO:NO_2$ estimated by C-GC (left, a), S-GC (middle, b), and C-CC (right, c) for 2016. Annual average of $NO:NO_2$ is calculated as annual mean NO divided by annual mean NO_2.

Differences in $NO:NO_2$ may also be related to differences in emissions and treatment of oxidants such as VOCs and bromine. C-GC and C-CC show a reduction in $NO:NO_2$ over the Amazon and in the Congo river basin, but this pattern is not reproduced in S-GC. Similarly, topographical features including the Andes and Himalayas are visible in the C-CC and C-GC $NO:NO_2$ ratios, but not in the S-GC data – whereas a large reduction in $NO:NO_2$ over the Arctic Ocean is more pronounced in S-GC and C-GC than in C-CC. This latter feature may be related to differences in the response of the simulated atmosphere to anthropogenic emissions, as ship tracks are more visible in the C-GC and S-GC $NO:NO_2$ ratios (see e.g. Cape Horn and the Cape of Good Hope) than in C-CC.

Figure 18 compares surface ozone against monitor measurements. The correlation coefficients are shown in Table 9. The geographical pattern is also consistent, with high surface ozone concentrations over the Mediterranean Sea and lower concentrations over Northern Europe.

Table 9. Correlation coefficients of surface-level ozone mass concentrations for C-GC, S-GC and C-CC against measurements.

	C-GC	*S-GC*	*C-CC*
North America	0.37	0.28	0.24
Europe	0.44	0.43	0.44
South-East Asia	-0.24	-0.07	-0.22

However, the results from all models appear to be biased low. As discussed in Section 4.2, C-GC estimates surface ozone mixing ratios lower than either S-GC and C-CC, and therefore exhibits the greatest mean bias. C-GC, C-CC, and S-GC show mean biases of -15, -9, and -10 ppbv for over Europe; -10, -3, and -5 ppbv over North America; and -20, -11, and -12 ppbv over South-East Asia.

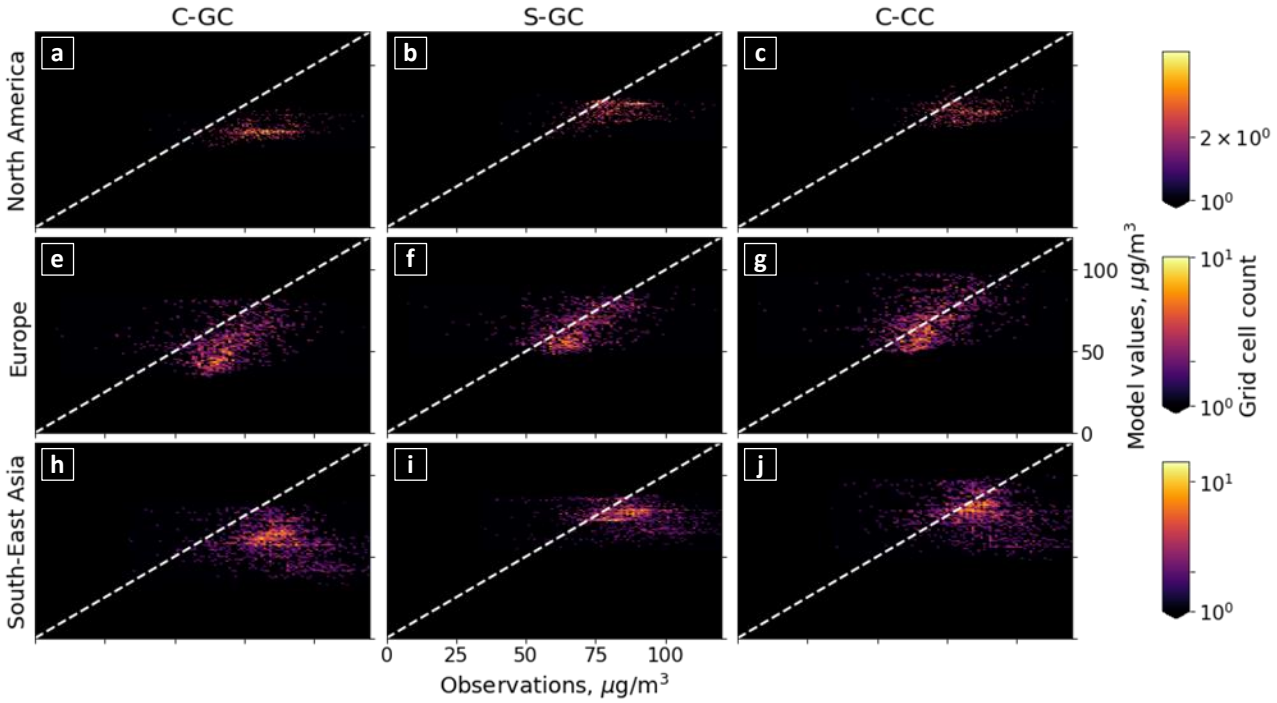

Figure 18. Annual average surface ozone mass concentrations simulated by C-GC (left: a, e, h), S-GC (middle: b, f, i), and C-CC (right: c, g, j) for 2016 compared against monitor measurements in North America (top: a-c), Europe (middle: d-e), and South East Asia (bottom: h-j).

The greater negative bias in simulated ozone shown by C-GC is likely related to both the different representation of meteorology compared to S-GC and the greater bromine emissions compared to both S-GC and C-CC. However, further work is needed to disentangle the root causes of discrepancies between the three models, and the common biases relative to observations.

5.2. Vertical profiles of ozone

We now focus on the evaluation of the profile of ozone mixing ratios by comparing C-GC, C-CC, and S-GC to a climatology of ozone sonde observations from 1995-2010 (Tilmes et al., 2012). This climatology (in addition to those shown in Section 5.3) has been used repeatedly in evaluations of CAM-chem, and is therefore chosen here to provide a familiar point of comparison which also allows the three configurations to be compared to a realistic baseline. Over the past decades, observations from ozone sondes in different locations provide a valuable dataset of the evolution of ozone mixing ratios in the troposphere and stratosphere. Figure 19 provides a Taylor diagram comparison between the C-GC, C-CC, and S-GC simulations of 2016 to the climatology.

In general, C-GC does not perform significantly better or worse than C-CC or S-GC, producing mean biases and correlations in each region/altitude combination which are within the same range. The clearest exception is at low altitudes (900 or 500 hPa) and mid- to high latitudes. In these regions, C-GC results frequently show a smaller normalized difference from the mean (radius) than either S-GC or C-CC, but also a weaker correlation with the observed seasonal cycle. The C-GC simulation of tropical ozone also shows the smallest mean bias at all altitudes at or below 250 hPa (panels a, d, and g), although again showing a weaker correlation.

At high altitude (50 hPa, panels j-l), all three models appear to perform similarly. This may however simply reflect the lack of spin up time. Since the three models only simulated 1.5-2 years in total, the simulated stratosphere will not have had time to fully respond to the new model configuration. Longer simulations are needed to fully evaluate the performance and capability of the C-GC stratosphere.

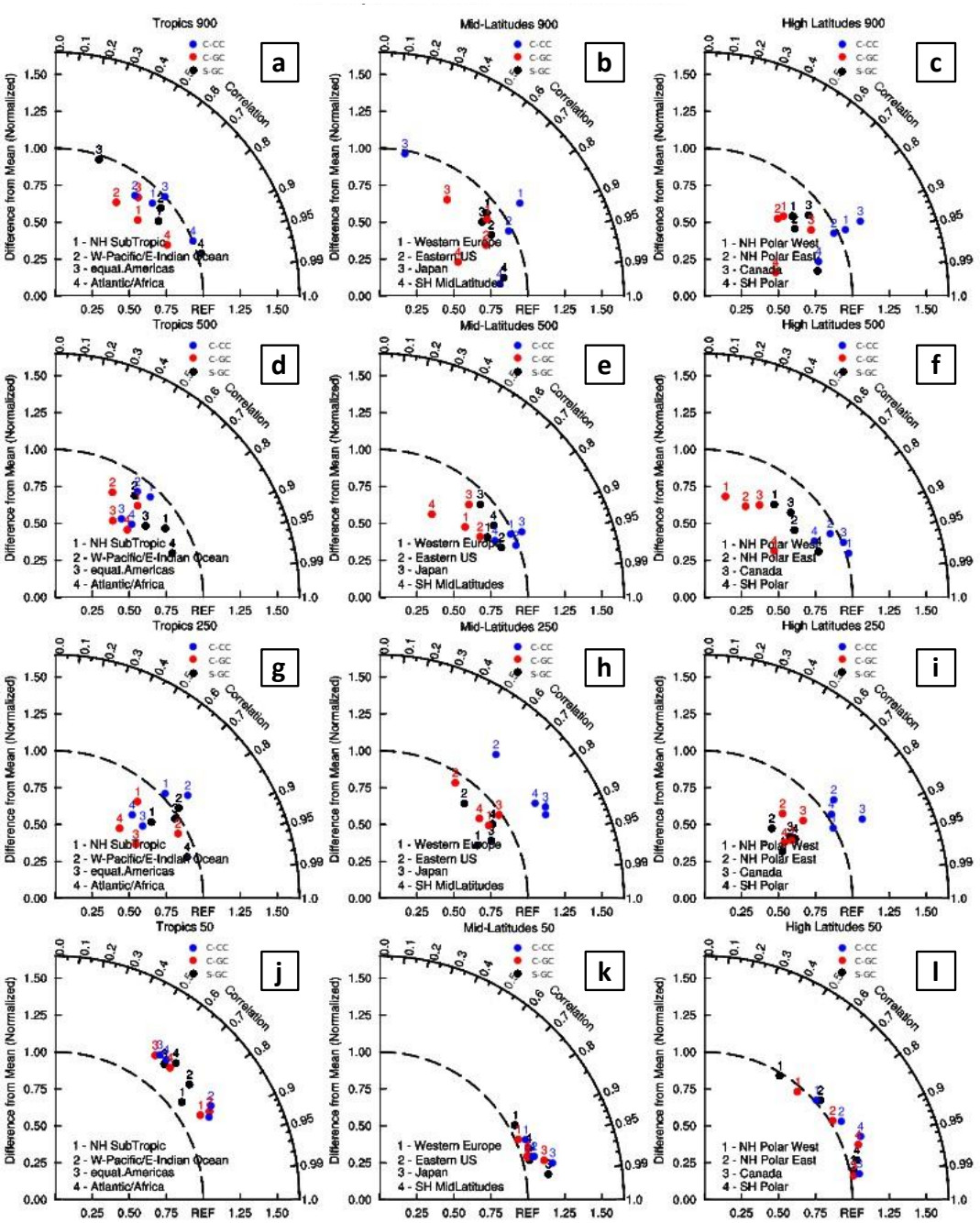

Figure 19. Taylor diagrams of the comparison of C-GC (red), C-CC (blue), and S-GC (black) simulations to a present-day (1995-2010) ozone sonde climatology. Top row to bottom row: comparisons at 900 (a-c), 500 (d-f), 250 (g-i) and 50 hPa (j-l). Left column to right column: tropics (a, d, g, j), mid latitudes (b, e, h, j), and high latitudes (c, f, i, l). The normalized mean difference between simulations and observations for each region is shown on the radius, and the correlation of the seasonal cycle is shown as the angle from the vertical.

5.3. Total column ozone and CO

Figure 20 shows total ozone column climatologies in Dobson Units as measured by OMI/MLS for the 2004-2010 time period (Ziemke et al., 2011). The results from the satellite observations (panel a) are compared to results from C-GC, C-CC, and S-GC (panels b, d, and f respectively,). We find that on average the results from C-GC are 7.8 DU lower than the observations (panel c), mostly driven by an overestimation of stratospheric ozone depletion during the Antarctic spring of up to 16 DU (value not shown in figure). C-CC predicts a total ozone column that is 6.6 DU larger than the global mean ozone column (panel e). When broken down by tropospheric and stratospheric ozone column, we find that the bias in the stratospheric and tropospheric ozone columns for C-GC is -2 and -6 DU respectively, compared to +9.5 and -2.5 DU for C-CC (value not shown in figure). Additionally, we find that the bias in seasonal variations of total column ozone as predicted by C-GC range between -16 and -6 DU, while the variations range from -3 to +7 DU for C-CC (value not shown in figure). The model results from S-GC predict similar geographical biases in total ozone column as C-GC, although with a smaller net bias of -3.3 DU (panel g).

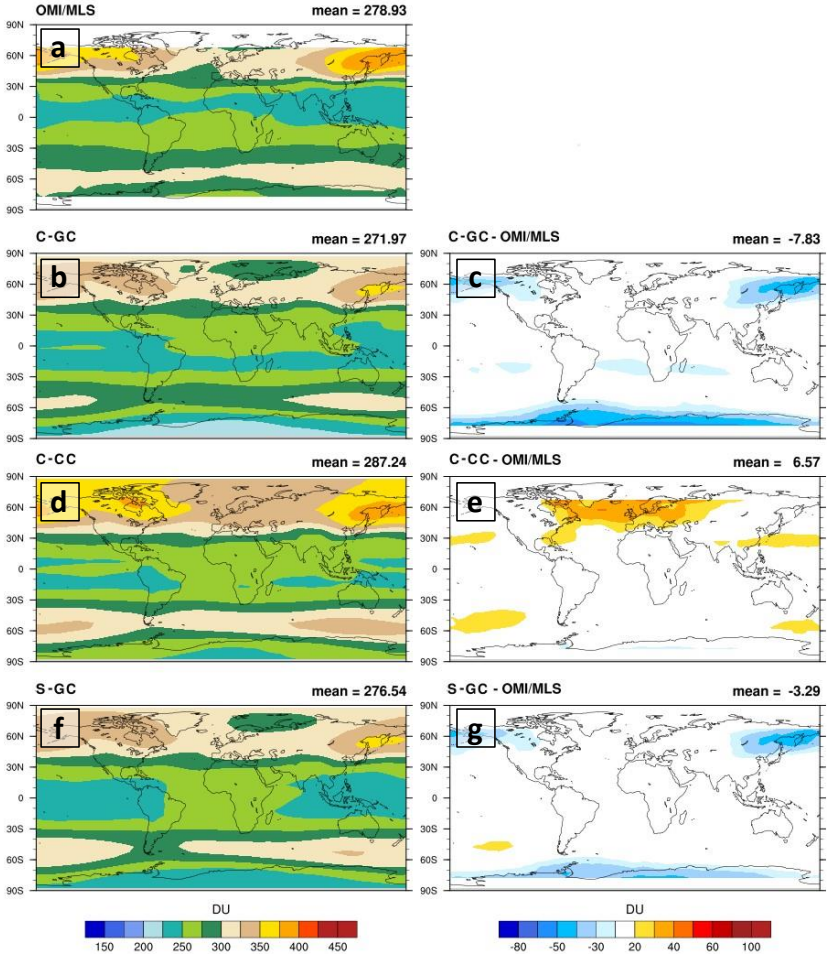

Figure 20. Total ozone column in DU as observed by OMI/MLS for the 2004-2010 time period (panel a), compared to the results from C-GC (2nd row, panels b and c), C-CC (3rd row, panels d and e), and S-GC (4th row, panels f and g) for the year 2016. The measurements and model results are presented on the left (a, b, d, f), while the model biases are shown on the right (c, e, g).

Figure 21 compares the simulated total columns of CO (panels b, d, and f) to retrievals from the MOPITT satellite instrument (panel a), averaged for each April in the period 2003 to 2012 (Deeter et al., 2014). The model results as well as the model biases are shown for April 2016. The CO model estimates using C-CC (panel d) are characterized by a bias of -9×10^{17} molec/cm^2 in the Northern Hemisphere (panel e), consistent with previous evaluations of CAM-chem (Emmons et al., 2020). In C-GC (panel b), a negative bias still exists in the Northern Hemisphere (panel c), but is smaller at -5×10^{17} molec/cm^2. Across all three model configurations a north-south gradient is observed in the model bias, with the bias in the Southern Hemisphere being approximately 10^{18} molec/cm^2, which is of greater magnitude than the (negative) bias in the Northern Hemisphere. The results from S-GC (panel f) are nearly identical to those in C-GC, with a smaller negative bias in the Northern Hemisphere (panel g) than C-CC, but a larger positive bias in the Southern Hemisphere.

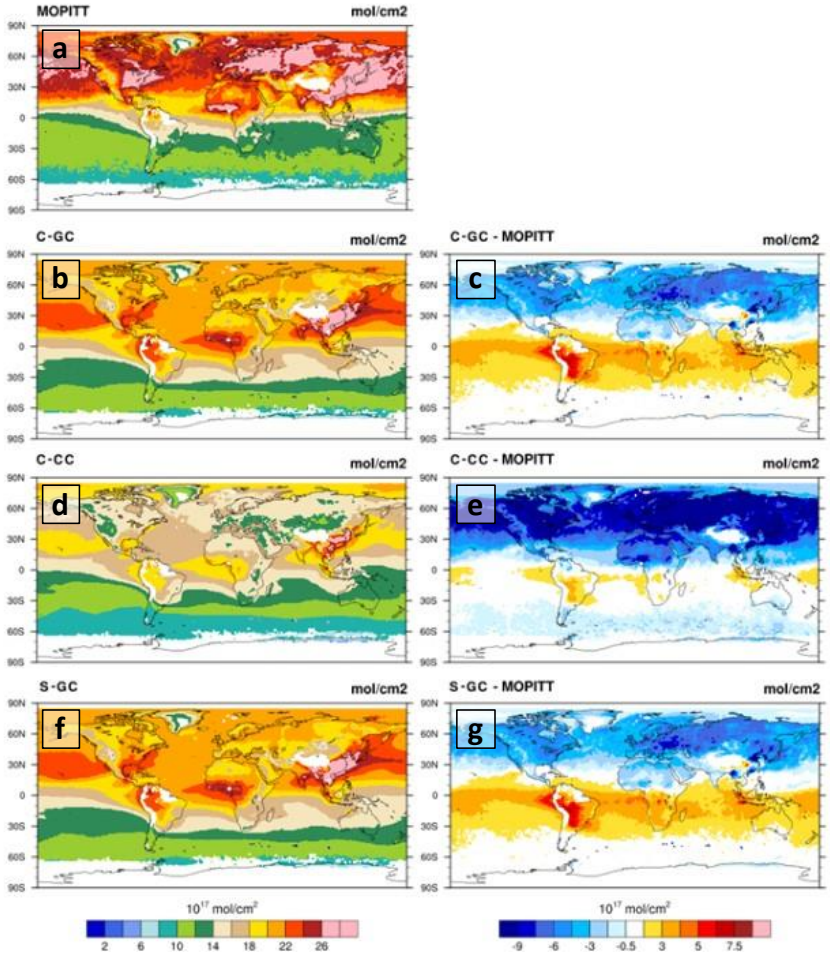

Figure 21. Total CO column in molec/cm^2 as observed by MOPITT during April for the 2003-2012 time period. (panel a), compared to the results from C-GC (2nd row, panels b and c), C-CC (3rd row, panels d and e), and S-GC (4th row, panels f and g) for April 2016. The measurements and model results are presented on the left (a, b, d, f), while the model biases are shown on the right (c, e, g).

5.4. Wet and dry deposition tendencies

Finally, we compare simulated and observed surface deposition. Since deposition is the primary removal mechanism for atmospheric reactive nitrogen and sulfur species, the ability of a model to reproduce observed patterns of deposition provides an aggregate diagnostic for its representation of emissions, atmospheric chemistry, and the physical deposition processes.

Recent measurements have provided wet deposition rates in numerous geographical locations for the years 2005 to 2007 (Vet et al., 2014). Dry deposition fluxes are available from the same study but are limited to sulfur and nitrogen species. They are also limited to fewer geographical locations. Nonetheless we compare results from all three model configurations to the results from Vet et al. (2014) below.

Figure 22 compares the model-evaluated wet deposition rates of nitrogen at the surface for C-GC, C-CC, and S-GC. The total nitrogen flux is calculated by adding surface fluxes from each individual nitrogen compound undergoing wet deposition. Rainwater composition measurements are also displayed where available for comparison. We find correlation coefficients of 0.65, 0.66, and 0.67 for C-GC, C-CC and S-GC respectively with these observations. On average, the results from C-GC (panel b) are closest to parity with a slope of 0.6, compared to 0.5 and 0.49 for C-CC (panel d) and S-GC (panel f). We do not find any clear trends by location between the three models.

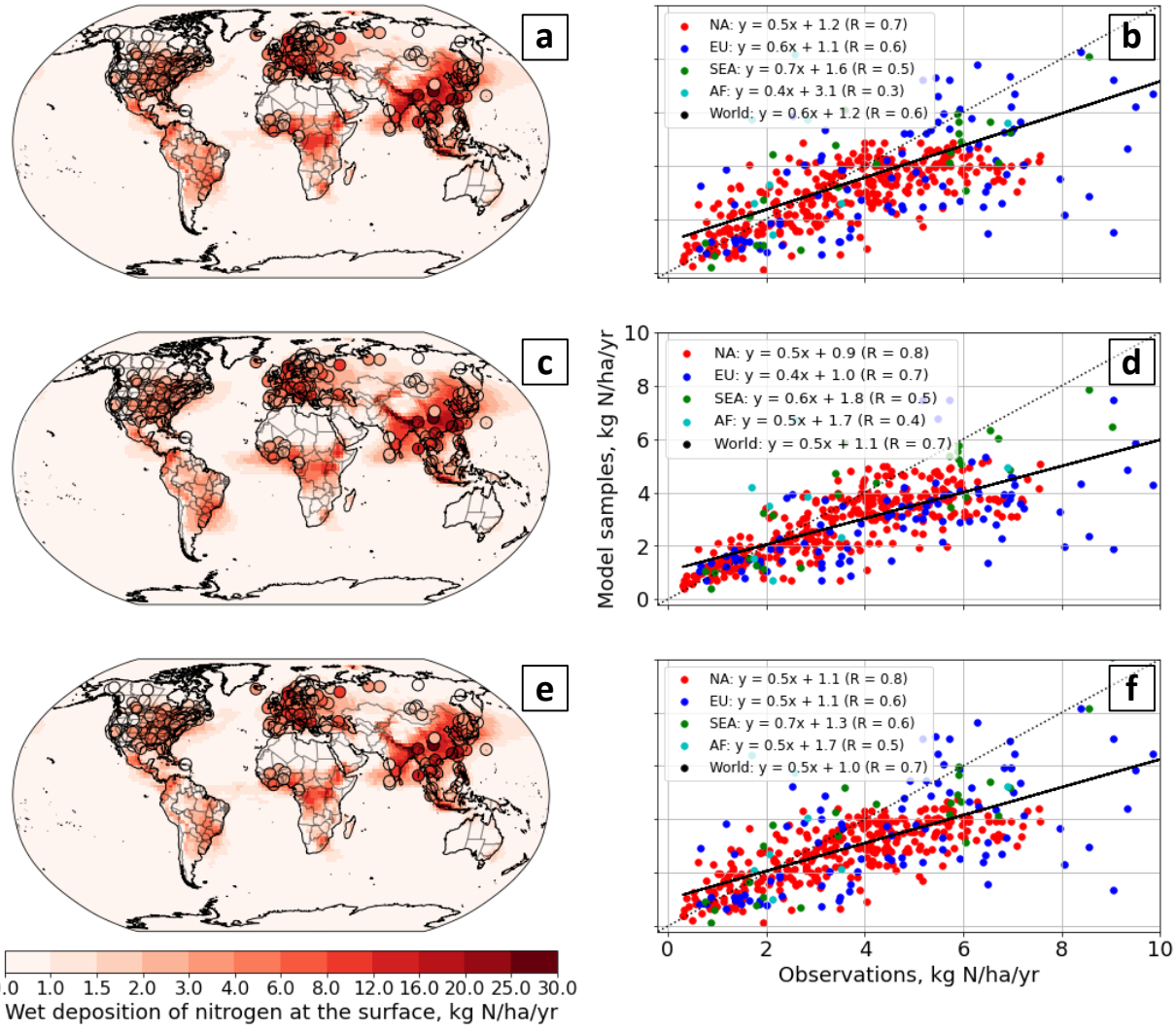

Figure 22. Geographical distribution of the wet deposition flux of nitrogen for C-GC (top, panels a-b), S-GC (middle, panels c-d), and C-CC (bottom, panels e-f). The annual mean value is shown as a map for each model, with circles used to indicate observational measurements (left, panels a, c, e). A parity plot of the results against the rainwater composition measurements is also provided for each model simulation (right, panels b, d, f).

Comparing the dry deposition flux of nitrogen species at the surface from C-GC, C-CC and S-GC to in-situ measurements over North America (the only region present in this data set) from 2005 to 2007 shows that all models have positive biases. Relative to an observational mean of 1.57 kgN/ha/yr, C-GC has the best performance with a mean bias of +0.94 kgN/ha/yr, compared to +1.76 and +2.32 kgN/ha/yr from S-GC and C-CC respectively. These biases from all three models can be explained by either larger concentrations of nitrogen compounds or enhanced dry deposition velocities. However, we do not compensate for changes in nitrogen emissions between the time of the observations (2005-2007) and the simulated period, during which NO_x emissions are estimated to have increased (Emmons et al., 2020).

Figure 23 displays the evaluated wet deposition rates of non-sea salt sulfur from C-GC, C-CC, and S-GC alongside measurements of sulfur in rainwater for 2005. When comparing across model results, we find a global mean deposition rate of 0.58, 0.38, and 0.50 kg S/ha/year in C-GC, S-GC, and C-CC respectively (computed as the global surface average of the left panels in Figure 23). The results from C-GC and C-CC show a correlation coefficient greater than 0.95, whereas C-GC and S-GC results show a correlation coefficient of 0.88.

Comparing to observational data, we find a mean bias of –2.40 kg S/ha/year (C-CC and C-GC) and –2.76 kg S/ha/year (S-GC) between the simulation results and rainwater composition measurements. This bias is location-dependent, with simulated data for Asia showing a lower bias than North America or Europe. For instance, over North America, measurements indicate a mean sulfur wet deposition flux of approximately 5 kg S/ha/year (for the year 2005), while the results at the same stations are lower with the slope of the linear fit equal to 0.2, 0.1, and 0.2 for C-GC, S-GC and C-CC respectively. This can be explained by the reduction in the sulfur wet deposition surface flux over the past decades. Previous literature has found that the deposition rate of sulfur over the Eastern U.S. has been decreasing at a rate of 1 kg S/ha/year^2 since 1990, with 60% of the reduction being in wet deposition rates and 40% in dry deposition rates (Zhang et al., 2018). Similar findings have been suggested for wet deposition rates over Europe (Theobald et al., 2019). A similar, but more recent, decrease over Asia has also been observed (Aas et al., 2019).

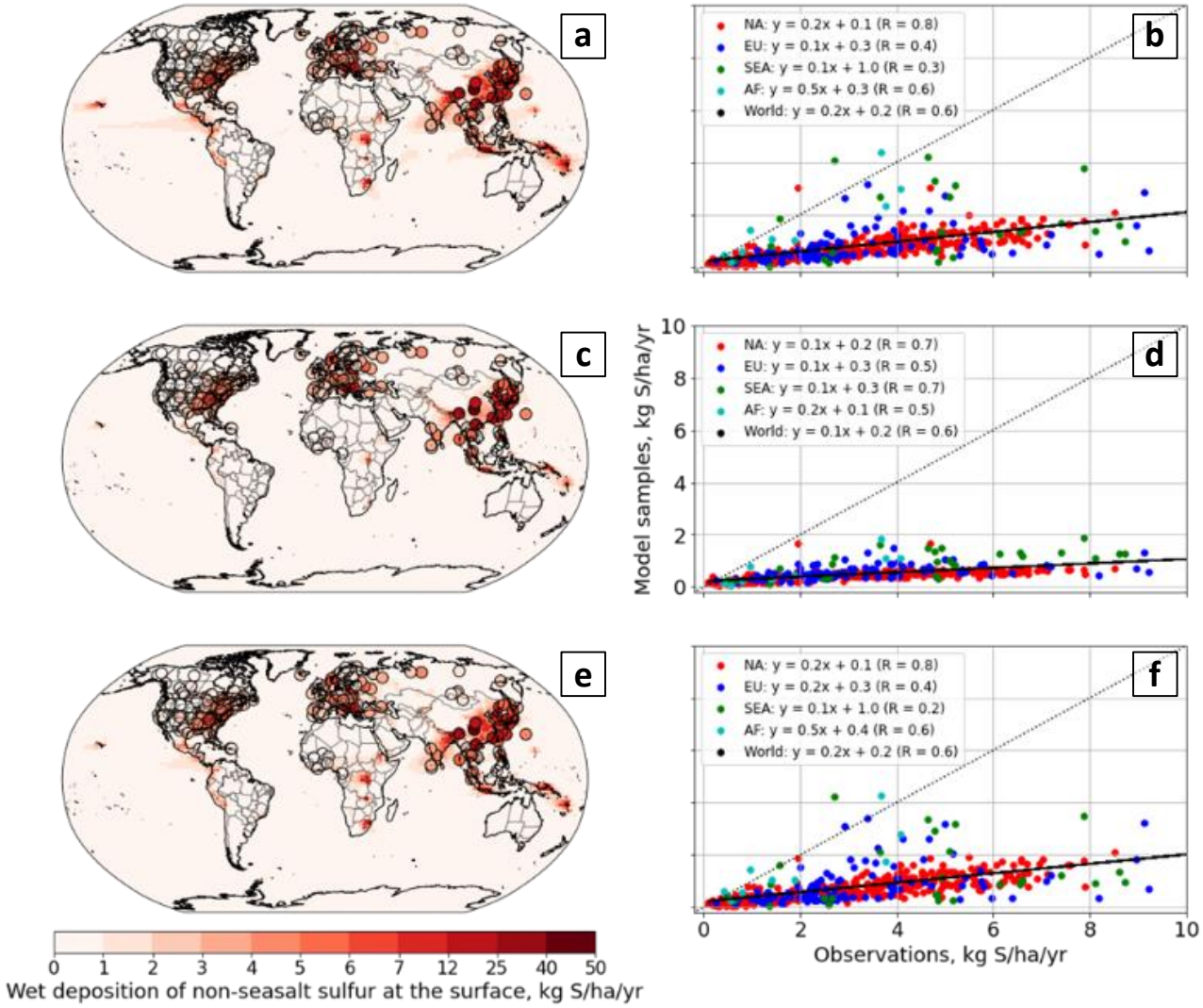

Figure 23. As in Figure 22, but now for non-sea salt sulfur. Rows: C-GC (top), S-GC (middle), and C-CC (bottom).

It is difficult to say with confidence that the calculated bias is purely due to lack of recent data without new measurements to support this conclusion. However, our results do show that the simulation of sulfur deposition in C-GC more closely follows that in C-CC than that in S-GC. This could be due to either the simulated distribution of precipitation, the representation of aerosol, or the representation of scavenging processes, all of which differ between C-GC (or C-CC) and S-GC.

6. Discussion and conclusion

We present the first implementation of the GEOS-Chem chemistry mechanism as an option in the Community Earth System Model (CESM). In addition to allowing users of CESM to take advantage of advancements in atmospheric modeling implemented in the GEOS-Chem model, this also allows the community to better understand why models disagree and how progress might be made to improve model performance and accuracy.

Our results suggest that differences in the representation of tropospheric halogen chemistry – in particular the representation and magnitude of emissions of short-lived bromine and chlorine sources – may be responsible for differences in simulated ozone between these model configurations. However, in addition to the recognized differences in chemical mechanisms, subtle structural differences in atmospheric models may have a significant role. Our evaluation of tropospheric ozone concentrations suggests that one of the key drivers in differences between CAM-chem and GEOS-Chem ozone fields differences may be differences in free tropospheric water vapor. Similarly, we show that sulfur deposition rates are approximately twice as great when running GEOS-Chem in a standalone model as opposed to running GEOS-Chem embedded in CESM, despite the use of identical emissions.

We also find that differences in the representation of wet scavenging are a significant contributor to differences in reactive nitrogen and halogen species distributions between GEOS-Chem and CAM-chem. The unification of convective transport and scavenging in GEOS-Chem helps to prevent movement of soluble species to the upper troposphere through convective updrafts, and therefore limits the effect of near surface halogen emissions from sea salt on ozone at higher altitudes.

Our implementation of GEOS-Chem in CESM is now publicly available for use. We envision that this model can become a powerful tool for research, forecast, and regulatory applications of global atmospheric chemistry, air quality, and climate research. Furthermore, this is also an important step towards the Multiscale Infrastructure for Chemistry and Aerosols (MUSICA), and thereof a truly modular Earth system model. By enabling us to fairly compare models down to individual processes, we can begin to understand precisely why different models perform better or worse in reproducing different measurements and accelerate our efforts to improve atmospheric modeling fidelity as a whole.

Finally, this work will foster collaboration between the GEOS-Chem and CESM-CAM-chem communities. GEOS-Chem is presently used and developed worldwide for research by over 100 university groups and government agencies, and CAM-chem similarly has numerous users and developers. The availability of GEOS-Chem as an option in CESM will stimulate broader interest in the GEOS-Chem community to use CESM, and in the CESM community to use GEOS-Chem. Indeed, we expect that on-line simulation of atmospheric chemistry will become increasingly attractive to GEOS-Chem users as the resolution of dynamical models increase, and that CESM will provide the principal vehicle for this because of its public

availability and support. By enabling improvements developed for GEOS-Chem to percolate into CESM without the need for re-implementation, this work will accelerate progress in atmospheric chemistry and Earth system modeling.

Author contributions

TMF, SDE, HL, and EWL were responsible for the software development. TMF performed the investigation, formal analysis, and validation. SDE, LKE, SRHB, and DJJ conceived of the project and acquired funding. SDE, LKE, SG, SRHB, and DJJ supervised the work. TMF performed all visualization and prepared the original draft. Review and editing were performed by all co-authors. All contributions are defined according to the CRediT taxonomy (https://casrai.org/credit).

Acknowledgements

This material is based upon work supported by the National Science Foundation under Grant No. 1914920. We would like to acknowledge high-performance computing support from Cheyenne (doi:10.5065/D6RX99HX) provided by NCAR's Computational and Information Systems Laboratory (CISL), sponsored by the National Science Foundation.

We would like to thank Mary Barth, Simone Tilmes, and Jean-François Lamarque for their assistance in understanding washout of aerosols in CESM. We also would like to thank Eloise Marais and Alma Hodzic for their help regarding the mapping of secondary organic aerosols.

Code availability statement

GEOS-Chem as an option within CESM is currently being implemented into the CESM main branch, such that no additional download will be needed to use it. However, a standalone copy of the specific implementation of CESM including GEOS-Chem which was used to generate the results in this manuscript is permanently archived at https://github.com/CESM-GC/CESM-GC-Standalone/releases/tag/v1.0.0_review (permanent DOI: https://doi.org/10.5281/zenodo.6465076). To reproduce the results of this work, the repository should be used as-is without using features such as checkout_externals to acquire any additional code.

Data availability statement

Output data from the model are available from the authors upon request. Satellite data retrievals including from OMI/MLS and of carbon monoxide from the Terra/MOPITT instrument are available from the NASA Earth data archive (https://earthdata.nasa.gov; ftp://l5ftl01.larc.nasa.gov/MOPITT/). Surface observations of carbon monoxide are available from

the NOAA Earth System Research Laboratory Global Monitoring Division data archive (https://www.esrl.noaa.gov/gmd/dv/ftpdata.html).

Competing interests

The authors declare that they have no conflict of interest.

References

Aas, W., Mortier, A., Bowersox, V., Cherian, R., Faluvegi, G., Fagerli, H., Hand, J., Klimont, Z., Galy-Lacaux, C., Lehmann, C. M. B., Myhre, C. L., Myhre, G., Olivié, D., Sato, K., Quaas, J., Rao, P. S. P., Schulz, M., Shindell, D., Skeie, R. B., Stein, A., Takemura, T., Tsyro, S., Vet, R., and Xu, X.: Global and regional trends of atmospheric sulfur, Sci. Rep., 9, 953, 2019.

Alexander, B., Park, R. J., Jacob, D. J., Li, Q. B., Yantosca, R. M., Savarino, J., Lee, C. C. W., and Thiemens, M. H.: Sulfate formation in sea-salt aerosols: Constraints from oxygen isotopes, J. Geophys. Res. D: Atmos., 110, 1–12, 2005.

Amos, H. M., Jacob, D. J., Holmes, C. D., Fisher, J. A., Wang, Q., Yantosca, R. M., Corbitt, E. S., Galarneau, E., Rutter, A. P., Gustin, M. S., Steffen, A., Schauer, J. J., Graydon, J. A., Louis, V. L. S., Talbot, R. W., Edgerton, E. S., Zhang, Y., and Sunderland, E. M.: Gas-particle partitioning of atmospheric Hg(II) and its effect on global mercury deposition, Atmos. Chem. Phys., 12, 591–603, 2012.

Andres, R. J. and Kasgnoc, A. D.: A time-averaged inventory of subaerial volcanic sulfur emissions, J. Geophys. Res., 103, 25251–25261, 1998.

AirNow API: https://docs.airnowapi.org/, last access: 9 September 2021.

Badia, A., Iglesias-Suarez, F., Fernandez, R. P., Cuevas, C. A., Kinnison, D. E., Lamarque, J.-F., Griffiths, P. T., Tarasick, D. W., Liu, J., and Saiz-Lopez, A.: The role of natural halogens in global tropospheric ozone chemistry and budget under different 21st century climate scenarios, J. Geophys. Res., 126, https://doi.org/10.1029/2021jd034859, 2021.

Bey, I., Jacob, D. J., Yantosca, R. M., Logan, J. A., Field, B. D., Fiore, A. M., Li, Q., Liu, H. Y., Mickley, L. J., and Schultz, M. G.: Global modeling of tropospheric chemistry with assimilated meteorology: Model description and evaluation, J. Geophys. Res., 106, 23073–23095, 2001.

Bogenschutz, P. A., Gettelman, A., Morrison, H., Larson, V. E., Craig, C., and Schanen, D. P.: Higher-Order Turbulence Closure and Its Impact on Climate Simulations in the Community Atmosphere Model, J. Clim., 26, 9655–9676, 2013.

Brasseur, G. P. and Solomon, S.: Aeronomy of the middle atmosphere, 3rd ed., Springer, New York, NY, 646 pp., 2006.

Bretherton, C., Balaji, V., Delworth, T., Dickinson, R. E., Edmonds, J. A., Famiglietti, J. S., and Smarr, L. L.: A national strategy for advancing climate modeling, National Academies Press, 2012.

Carn, S. A., Yang, K., Prata, A. J., and Krotkov, N. A.: Extending the long-term record of volcanic SO_2 emissions with the Ozone Mapping and Profiler Suite nadir mapper: OMPS volcanic SO_2 measurements, Geophys. Res. Lett., 42, 925–932, 2015.

China Air Quality Historical Data: https://quotsoft.net/air/, last access: 2021.

Cohen, R. C. and Murphy, J. G.: Photochemistry of NO_2 in Earth's stratosphere: constraints from observations, Chem. Rev., 103, 4985–4998, 2003.

Damian, V., Sandu, A., Damian, M., Potra, F., and Carmichael, G. R.: The kinetic preprocessor KPP-a software environment for solving chemical kinetics, Comput. Chem. Eng., 26, 1567–1579, 2002.

Deeter, M. N., Martínez-Alonso, S., Edwards, D. P., Emmons, L. K., Gille, J. C., Worden, H. M., Sweeney, C., Pittman, J. V., Daube, B.

C., and Wofsy, S. C.: The MOPITT Version 6 product: algorithm enhancements and validation, Atmos. Meas. Tech., 7, 3623–3632, 2014.

Dunlea, E. J., Herndon, S. C., Nelson, D. D., Volkamer, R. M., San Martini, F., Sheehy, P. M., Zahniser, M. S., Shorter, J. H., Wormhoudt, J. C., Lamb, B. K., Allwine, E. J., Gaffney, J. S., Marley, N. A., Grutter, M., Marquez, C., Blanco, S., Cardenas, B., Retama, A., Ramos Villegas, C. R., Kolb, C. E., Molina, L. T., and Molina, M. J.: Evaluation of nitrogen dioxide chemiluminescence monitors in a polluted urban environment, Atmos. Chem. Phys., 7, 2691–2704, 2007.

Eastham, S. D., Weisenstein, D. K., and Barrett, S. R. H.: Development and evaluation of the unified tropospheric–stratospheric chemistry extension (UCX) for the global chemistry-transport model GEOS-Chem, Atmos. Environ., 89, 52–63, 2014.

Eastham, S. D., Long, M. S., Keller, C. A., Lundgren, E., Yantosca, R. M., Zhuang, J., Li, C., Lee, C. J., Yannetti, M., Auer, B. M., Clune, T. L., Kouatchou, J., Putman, W. M., Thompson, M. A., Trayanov, A. L., Molod, A. M., Martin, R. V., and Jacob, D. J.: GEOS-Chem High Performance (GCHP v11-02c): A next-generation implementation of the GEOS-Chem chemical transport model for massively parallel applications, Geosci. Model Dev., 2941–2953, 2018.

Emmons, L. K., Arnold, S. R., Monks, S. A., Huijnen, V., Tilmes, S., Law, K. S., Thomas, J. L., Raut, J.-C., Bouarar, I., Turquety, S., Long, Y., Duncan, B., Steenrod, S., Strode, S., Flemming, J., Mao, J., Langner, J., Thompson, A. M., Tarasick, D., Apel, E. C., Blake, D. R., Cohen, R. C., Dibb, J., Diskin, G. S., Fried, A., Hall, S. R., Huey, L. G., Weinheimer, A. J., Wisthaler, A., Mikoviny, T., Nowak, J., Peischl, J., Roberts, J. M., Ryerson, T., Warneke, C., and Helmig, D.: The POLARCAT Model Intercomparison Project (POLMIP): overview and evaluation with observations, Atmos. Chem. Phys., 15, 6721–6744, 2015.

Emmons, L. K., Schwantes, R. H., Orlando, J. J., Tyndall, G., Kinnison, D., Lamarque, J.-F., Marsh, D., Mills, M. J., Tilmes, S., Bardeen, C., Buchholz, R. R., Conley, A., Gettelman, A., Garcia, R., Simpson, I., Blake, D. R., Meinardi, S., and Pétron, G.: The chemistry mechanism in the community earth system model version 2 (CESM2), J. Adv. Model. Earth Syst., 12, e2019MS001882, 2020.

European Air Quality Portal: https://discomap.eea.europa.eu/map/fme/AirQualityExport.htm, last access: 2021.

Fahey, D., Newman, P. A., Pyle, J. A., Safari, B., Chipperfield, M. P., Karoly, D., Kinnison, D. E., Ko, M., Santee, M., and Doherty, S. J.: Scientific assessment of ozone depletion: 2018, global ozone research and monitoring project-report no. 58, World Meteorological Organization, 2018.

Fairlie, D. T., Jacob, D. J., and Park, R. J.: The impact of transpacific transport of mineral dust in the United States, Atmos. Environ., 41, 1251–1266, 2007.

Feng, X., Lin, H., Fu, T.-M., Sulprizio, M. P., Zhuang, J., Jacob, D. J., Tian, H., Ma, Y., Zhang, L., Wang, X., Chen, Q., and Han, Z.: WRF-GC (v2.0): online two-way coupling of WRF (v3.9.1.1) and GEOS-Chem (v12.7.2) for modeling regional atmospheric chemistry–meteorology interactions, Geosci. Model Dev., 14, 3741–3768, 2021.

Fernandez, R. P., Barrera, J. A., López-Noreña, A. I., Kinnison, D. E., Nicely, J., Salawitch, R. J., Wales, P. A., Toselli, B. M., Tilmes, S., Lamarque, J.-F., Cuevas, C. A., and Saiz-Lopez, A.: Intercomparison Between Surrogate, Explicit, and Full Treatments of VSL Bromine Chemistry Within the CAM-Chem Chemistry-Climate Model, Geophys. Res. Lett., 48, e2020GL091125, 2021.

Fountoukis, C. and Nenes, A.: ISORROPIA II: a computationally efficient thermodynamic equilibrium model for K^+-Ca^{2+}-Mg^{2+}-NH_4-Na^+-SO_4^{2+}-NO_3^--Cl^--H_2O aerosols, 4639–4659, 2007.

Ge, C., Wang, J., Carn, S., Yang, K., Ginoux, P., and Krotkov, N.: Satellite-based global volcanic SO_2 emissions and sulfate direct radiative forcing during 2005-2012, J. Geophys. Res., 121, 3446–3464, 2016.

Guenther, a. B., Jiang, X., Heald, C. L., Sakulyanontvittaya, T., Duhl, T., Emmons, L. K., and Wang, X.: The model of emissions of gases and aerosols from nature version 2.1 (MEGAN2.1): An extended and updated framework for modeling biogenic emissions, 5, 1471–1492, 2012.

He, J., Zhang, Y., Glotfelty, T., He, R., Bennartz, R., Rausch, J., and Sartelet, K.: Decadal simulation and comprehensive evaluation of CESM/CAM5.1 with advanced chemistry, aerosol microphysics, and aerosol-cloud interactions, J. Adv. Model. Earth Syst., 7, 110–141, 2015.

Hill, C., DeLuca, C., Balaji, Suarez, M., and Silva, A. D.: The architecture of the Earth System Modeling Framework, 6, 18–28, 2004.

Hoesly, R. M., Smith, S. J., Feng, L., Klimont, Z., Janssens-Maenhout, G., Pitkanen, T., Seibert, J. J., Vu, L., Andres, R. J., Bolt, R. M., Bond, T. C., Dawidowski, L., Kholod, N., Kurokawa, J.-I., Li, M., Liu, L., Lu, Z., Moura, M. C. P., O'Rourke, P. R., and Zhang, Q.: Historical (1750–2014) anthropogenic emissions of reactive gases and aerosols from the Community Emissions Data System (CEDS), Geoscientific Model Development, 11, 369–408, 2018.

Hu, L., Keller, C. A., Long, M. S., Sherwen, T., Auer, B., Da Silva, A., Nielsen, J. E., Pawson, S., Thompson, M. A., Trayanov, A. L., Travis, K. R., Grange, S. K., Evans, M. J., and Jacob, D. J.: Global simulation of tropospheric chemistry at 12.5 km resolution: performance and evaluation of the GEOS-Chem chemical module (v10-1) within the NASA GEOS Earth system model (GEOS-5 ESM), Geosci. Model Dev., 11, 4603–4620, 2018.

Hurrell, J. W., Holland, M. M., Gent, P. R., Ghan, S., Kay, J. E., Kushner, P. J., Lamarque, J.-F., Large, W. G., Lawrence, D., Lindsay, K., Lipscomb, W. H., Long, M. C., Mahowald, N., Marsh, D. R., Neale, R. B., Rasch, P., Vavrus, S., Vertenstein, M., Bader, D., Collins, W. D., Hack, J. J., Kiehl, J., and Marshall, S.: The Community Earth System Model: A Framework for Collaborative Research, Bull. Am. Meteorol. Soc., 94, 1339–1360, 2013.

Jaeglé, L., Quinn, P. K., Bates, T. S., Alexander, B., and Lin, J. T.: Global distribution of sea salt aerosols: New constraints from in situ and remote sensing observations, Atmos. Chem. Phys., 11, 3137–3157, 2011.

Jaeglé, L., Shah, V., Thornton, J. A., Lopez-Hilfiker, F. D., Lee, B. H., McDuffie, E. E., Fibiger, D., Brown, S. S., Veres, P., Sparks, T. L., Ebben, C. J., Wooldridge, P. J., Kenagy, H. S., Cohen, R. C., Weinheimer, A. J., Campos, T. L., Montzka, D. D., Digangi, J. P., Wolfe, G. M., Hanisco, T., Schroder, J. C., Campuzano-Jost, P., Day, D. A., Jimenez, J. L., Sullivan, A. P., Guo, H., and Weber, R. J.: Nitrogen oxides emissions, chemistry, deposition, and export over the northeast United States during the WINTER aircraft campaign, J. Geophys. Res., 123, 12,368-12,393, 2018.

Environmental Numerical Database: https://www.nies.go.jp/igreen/index.html, last access: 2021.

Jöckel, P., von Kuhlmann, R., Lawrence, M. G., Steil, B., Brenninkmeijer, C. A. M., Crutzen, P. J., Rasch, P. J., and Eaton, B.: On a fundamental problem in implementing flux-form advection schemes for tracer transport in 3-dimensional general circulation and chemistry transport models, Q.J.R. Meteorol. Soc., 127, 1035–1052, 2001.

Jonson, J. E., Schulz, M., Emmons, L., Flemming, J., Henze, D., Sudo, K., Tronstad Lund, M., Lin, M., Benedictow, A., Koffi, B., Dentener, F., Keating, T., Kivi, R., and Davila, Y.: The effects of intercontinental emission sources on European air pollution levels, Atmos. Chem. Phys., 18, 13655–13672, 2018.

Keller, C., Auer, B., Hu, L., Jacob, D., Long, M., Nielsen, E., Pawson, S., da Silva, A., and Thompson, M.: High-resolution GEOS-5 nature run with tropospheric chemistry, 2017.

Keller, C. A., Long, M. S., Yantosca, R. M., Da Silva, A. M., Pawson, S., and Jacob, D. J.: HEMCO v1.0: a versatile, ESMF-compliant component for calculating emissions in atmospheric models, Geoscientific Model Development, 7, 1409–1417, 2014.

Keller, C. A., Knowland, K. E., Duncan, B. N., Liu, J., Anderson, D. C., Das, S., Lucchesi, R. A., Lundgren, E. W., Nicely, J. M., Nielsen, E., Ott, L. E., Saunders, E., Strode, S. A., Wales, P. A., Jacob, D. J., and Pawson, S.: Description of the NASA GEOS composition forecast modeling system GEOS-CF v1.0, J. Adv. Model. Earth Syst., 13, https://doi.org/10.1029/2020ms002413, 2021.

Kinnison, D. E., Brasseur, G. P., and Walters, S.: Sensitivity of chemical tracers to meteorological parameters in the MOZART-3 chemical transport model, 2007.

Kodros, J. K. and Pierce, J. R.: Important global and regional differences in aerosol cloud-albedo effect estimates between simulations with and without prognostic aerosol microphysics, J. Geophys. Res., 122, 4003–4018, 2017.

Lamarque, J.-F., Emmons, L. K., Hess, P. G., Kinnison, D. E., Tilmes, S., Vitt, F., Heald, C. L., Holland, E. a., Lauritzen, P. H., Neu, J., Orlando, J. J., Rasch, P. J., and Tyndall, G. K.: CAM-chem: description and evaluation of interactive atmospheric chemistry in the Community Earth System Model, 5, 369–411, 2012.

Lin, H., Feng, X., Fu, T.-M., Tian, H., Ma, Y., Zhang, L., Jacob, D. J., Yantosca, R. M., Sulprizio, M. P., Lundgren, E. W., and Others: WRF-GC (v1. 0): online coupling of WRF (v3. 9.1. 1) and GEOS-Chem (v12. 2.1) for regional atmospheric chemistry modeling--Part 1: Description of the one-way model, 13, 3241–3265, 2020.

Lin, H., Jacob, D. J., Lundgren, E. W., Sulprizio, M. P., Keller, C. A., Fritz, T. M., Eastham, S. D., Emmons, L. K., Campbell, P. C., Baker, B., Saylor, R. D., and Montuoro, R.: Harmonized Emissions Component (HEMCO) 3.0 as a versatile emissions component for atmospheric models: application in the GEOS-Chem, NASA GEOS, WRF-GC, CESM2, NOAA GEFS-Aerosol, and NOAA UFS models, 2021.

Liu, H., Jacob, D. J., Bey, I., and Yantosca, R. M.: Constraints from ^{210}Pb and ^{7}Be on wet deposition and transport in a global three-dimensional chemical tracer model driven by assimilated meteorological fields, J. Geophys. Res., 106, 12109–12128, 2001.

Liu, X., Easter, R. C., Ghan, S. J., Zaveri, R., Rasch, P., Shi, X., Lamarque, J.-F., Gettelman, A., Morrison, H., Vitt, F., Conley, A., Park, S., Neale, R., Hannay, C., Ekman, A. M. L., Hess, P., Mahowald, N., Collins, W., Iacono, M. J., Bretherton, C. S., Flanner, M. G., and Mitchell, D.: Toward a minimal representation of aerosols in climate models: description and evaluation in the Community Atmosphere Model CAM5, Geosci. Model Dev., 5, 709–739, 2012.

Liu, X., Ma, P.-L., Wang, H., Tilmes, S., Singh, B., Easter, R. C., Ghan, S. J., and Rasch, P. J.: Description and evaluation of a new four-mode version of the Modal Aerosol Module (MAM4) within version 5.3 of the Community Atmosphere Model, Geosci. Model Dev., 9, 505–522, 2016.

Long, M. S., Yantosca, R., Nielsen, J. E., Keller, C. A., da Silva, A., Sulprizio, M. P., Pawson, S., and Jacob, D. J.: Development of a grid-independent GEOS-Chem chemical transport model (v9-02) as an atmospheric chemistry module for Earth system models, Geoscientific Model Development, 8, 595–602, 2015.

Marais, E. A., Jacob, D. J., Jimenez, J. L., Campuzano-Jost, P., Day, D. A., Hu, W., Krechmer, J., Zhu, L., Kim, P. S., Miller, C. C., and Others: Aqueous-phase mechanism for secondary organic aerosol formation from isoprene: application to the southeast United States and co-benefit of SO 2 emission controls, Atmos. Chem. Phys., 16, 1603–1618, 2016.

Mills, M. J., Schmidt, A., Easter, R., Solomon, S., Kinnison, D. E., Ghan, S. J., Neely, R. R., III, Marsh, D. R., Conley, A., Bardeen, C. G., and Gettelman, A.: Global volcanic aerosol properties derived from emissions, 1990–2014, using CESM1(WACCM), J. Geophys. Res., 121, 2332–2348, 2016.

Murray, L. T., Jacob, D. J., Logan, J. A., Hudman, R. C., and Koshak, W. J.: Optimized regional and interannual variability of lightning in a global chemical transport model constrained by LIS/OTD satellite data, J. Geophys. Res., 117, D20307, 2012.

Neely, R. R., III and Schmidt, A.: VolcanEESM: Global volcanic sulphur dioxide (SO2) emissions database from 1850 to present, https://doi.org/10.5285/76ebdc0b-0eed-4f70-b89e-55e606bcd568, 2016.

Neu, J. L. and Prather, M. J.: Toward a more physical representation of precipitation scavenging in global chemistry models: cloud overlap and ice physics and their impact on tropospheric ozone, Atmos. Chem. Phys., 12, 3289–3310, 2012.

Nicely, J. M., Salawitch, R. J., Canty, T., Anderson, D. C., Arnold, S. R., Chipperfield, M. P., Emmons, L. K., Flemming, J., Huijnen, V., Kinnison, D. E., Lamarque, J.-F., Mao, J., Monks, S. A., Steenrod, S. D., Tilmes, S., and Turquety, S.: Quantifying the causes of differences in tropospheric OH within global models, J. Geophys. Res., 122, 1983–2007, 2017.

NRC: The Future of Atmospheric Chemistry Research: Remembering Yesterday, Understanding Today, Anticipating Tomorrow, {National Research Council}, 226 pp., 2016.

Park, R. J.: Natural and transboundary pollution influences on sulfate-nitrate-ammonium aerosols in the United States: Implications for policy, J. Geophys. Res., 109, 13,791, 2004.

Park, R. J., Oak, Y. J., Emmons, L. K., Kim, C.-H., Pfister, G. G., Carmichael, G. R., Saide, P. E., Cho, S.-Y., Kim, S., Woo, J.-H., Crawford, J. H., Gaubert, B., Lee, H.-J., Park, S.-Y., Jo, Y.-J., Gao, M., Tang, B., Stanier, C. O., Shin, S. S., Park, H. Y., Bae, C., and Kim, E.: Multi-model intercomparisons of air quality simulations for the KORUS-AQ campaign, Elementa: Science of the Anthropocene, 9, https://doi.org/10.1525/elementa.2021.00139, 2021.

Pickering, K. E., Wang, Y., Tao, W.-K., Price, C., and Müller, J.-F.: Vertical distributions of lightning NO x for use in regional and global chemical transport models, J. Geophys. Res., 103, 31203–31216, 1998.

Pound, R. J., Sherwen, T., Helmig, D., Carpenter, L. J., and Evans, M. J.: Influences of oceanic ozone deposition on tropospheric photochemistry, Atmos. Chem. Phys., 20, 4227–4239, 2020.

Price, C., Penner, J., and Prather, M.: NO_x from lightning: 1. Global distribution based on lightning physics, J. Geophys. Res., 102, 5929–5941, 1997.

Pye, H. O. T. and Seinfeld, J. H.: A global perspective on aerosol from low-volatility organic compounds, Atmos. Chem. Phys., 10, 4377–4401, 2010.

Pye, H. O. T., Chan, A. W. H., Barkley, M. P., and Seinfeld, J. H.: Global modeling of organic aerosol: the importance of reactive nitrogen (NOx and NO3), Atmos. Chem. Phys., 10, 11261–11276, 2010.

Riahi, K., van Vuuren, D. P., Kriegler, E., Edmonds, J., O'Neill, B. C., Fujimori, S., Bauer, N., Calvin, K., Dellink, R., Fricko, O., Lutz, W., Popp, A., Cuaresma, J. C., Kc, S., Leimbach, M., Jiang, L., Kram, T., Rao, S., Emmerling, J., Ebi, K., Hasegawa, T., Havlik, P., Humpenöder, F., Da Silva, L. A., Smith, S., Stehfest, E., Bosetti, V., Eom, J., Gernaat, D., Masui, T., Rogelj, J., Strefler, J., Drouet, L., Krey, V., Luderer, G., Harmsen, M., Takahashi, K., Baumstark, L., Doelman, J. C., Kainuma, M., Klimont, Z., Marangoni, G., Lotze-Campen, H., Obersteiner, M., Tabeau, A., and Tavoni, M.: The Shared Socioeconomic Pathways and their energy, land use, and greenhouse gas emissions implications: An overview, Glob. Environ. Change, 42, 153–168, 2017.

Sandgathe, S., O'Connor, W., Lett, N., McCarren, D., and Toepfer, F.: National Unified Operational Prediction Capability Initiative, Bull. Am. Meteorol. Soc., 92, 1347–1351, 2011.

Schwantes, R. H., Lacey, F. G., Tilmes, S., Emmons, L. K., Lauritzen, P. H., Walters, S., Callaghan, P., Zarzycki, C. M., Barth, M. C., Jo, D. S., and Others: Evaluating the impact of chemical complexity and horizontal resolution on tropospheric ozone over the conterminous US with a global variable resolution chemistry model, 14, e2021MS002889, 2022.

Seinfeld, J. H. and Pandis, S. N.: Atmospheric Chemistry and Physics, 2nd ed., Wiley, 2006.

Simone, N. W., Stettler, M. E. J., and Barrett, S. R. H.: Rapid estimation of global civil aviation emissions with uncertainty quantification, Transp. Res. Part D: Trans. Environ., 25, 33–41, 2013.

Solomon, S., Kinnison, D., Bandoro, J., and Garcia, R.: Simulation of polar ozone depletion: An update, J. Geophys. Res. D: Atmos., 120, 7958–7974, 2015.

Theobald, M. R., Vivanco, M. G., Aas, W., Andersson, C., Ciarelli, G., Couvidat, F., Cuvelier, K., Manders, A., Mircea, M., Pay, M.-T., and Others: An evaluation of European nitrogen and sulfur wet deposition and their trends estimated by six chemistry transport models for the period 1990--2010, Atmos. Chem. Phys., 19, 379–405, 2019.

Tilmes, S., Lamarque, J.-F., Emmons, L. K., Conley, A., Schultz, M. G., Saunois, M., Thouret, V., Thompson, A. M., Oltmans, S. J., Johnson, B., and Tarasick, D.: Technical Note: Ozonesonde climatology between 1995 and 2011: description, evaluation and applications, Atmos. Chem. Phys., 12, 7475–7497, 2012.

Tilmes, S., Lamarque, J.-F., Emmons, L. K., Kinnison, D. E., Marsh, D., Garcia, R. R., Smith, A. K., Neely, R. R., Conley, A., Vitt, F., Val Martin, M., Tanimoto, H., Simpson, I., Blake, D. R., and Blake, N.: Representation of the Community Earth System Model (CESM1) CAM4-chem within the Chemistry-Climate Model Initiative (CCMI), Geosci. Model Dev., 9, 1853–1890, 2016.

Tilmes, S., Hodzic, A., Emmons, L. K., Mills, M. J., Gettelman, A., Kinnison, D. E., Park, M., Lamarque, J.-F., Vitt, F., Shrivastava, M., Campuzano-Jost, P., Jimenez, J. L., and Liu, X.: Climate forcing and trends of organic aerosols in the community earth system model (CESM2), J. Adv. Model. Earth Syst., 11, 4323–4351, 2019.

Val Martin, M., Heald, C. L., and Arnold, S. R.: Coupling dry deposition to vegetation phenology in the Community Earth System Model: Implications for the simulation of surface O3, Geophys. Res. Lett., 41, 2988–2996, 2014.

Vet, R., Artz, R. S., Carou, S., Shaw, M., Ro, C.-U., Aas, W., Baker, A., Bowersox, V. C., Dentener, F., Galy-Lacaux, C., Hou, A., Pienaar, J. J., Gillett, R., Forti, M. C., Gromov, S., Hara, H., Khodzher, T., Mahowald, N. M., Nickovic, S., Rao, P. S. P., and Reid, N. W.: A global assessment of precipitation chemistry and deposition of sulfur, nitrogen, sea salt, base cations, organic acids, acidity and pH, and phosphorus, Atmos. Environ., 93, 3–100, 2014.

Vinken, G. C. M., Boersma, K. F., Jacob, D. J., and Meijer, E. W.: Accounting for non-linear chemistry of ship plumes in the GEOS-Chem global chemistry transport model, Atmos. Chem. Phys., 11, 11707–11722, 2011.

Wang, X., Jacob, D. J., Eastham, S. D., Sulprizio, M. P., Zhu, L., Chen, Q., Alexander, B., Sherwen, T., Evans, M. J., Lee, B. H., Haskins, J. D., Lopez-Hilfiker, F. D., Thornton, J. A., Huey, G. L., and Liao, H.: The role of chlorine in global tropospheric chemistry, Atmos. Chem. Phys., 19, 3981–4003, 2019.

Wang, X., Jacob, D. J., Downs, W., Zhai, S., Zhu, L., Shah, V., Holmes, C. D., Sherwen, T., Alexander, B., Evans, M. J., Eastham, S. D., Neuman, J. A., Veres, P., Koenig, T. K., Volkamer, R., Huey, L. G., Bannan, T. J., Percival, C. J., Lee, B. H., and Thornton, J. A.: Global tropospheric halogen (Cl, Br, I) chemistry and its impact on oxidants, Atmos. Chem. Phys., https://doi.org/10.5194/acp-2021-441, 2021.

Wang, Y., Jacob, D. J., and Logan, J. A.: Global simulation of tropospheric O_3-NO_x-hydrocarbon chemistry: 1. Model formulation, J. Geophys. Res., 103, 10713–10725, 1998.

Wesely, M.: Parameterization of Surface Resistances to Gaseous Dry Deposition in Regional-Scale Numerical-Models, 765 Atmos. Environ., 23, 1293-1304, 1989.

Wild, O., Zhu, X., and Prather, M. J.: Fast-J: Accurate simulation of in- and below-cloud photolysis in tropospheric chemical models, J. Atmos. Chem., 245–282, 2000.

Wu, S., Mickley, L. J., Jacob, D. J., Logan, J. A., Yantosca, R. M., and Rind, D.: Why are there large differences between models in global budgets of tropospheric ozone?, J. Geophys. Res., 112, D05302, 2007.

Yu, F. and Luo, G.: Simulation of particle size distribution with a global aerosol model: contribution of nucleation to aerosol and CCN number concentrations, Atmos. Chem. Phys., 9, 7691–7710, 2009.

Yu, K., Keller, C. A., Jacob, D. J., Molod, A. M., Eastham, S. D., and Long, M. S.: Errors and improvements in the use of archived meteorological data for chemical transport modeling: an analysis using GEOS-Chem v11-01 driven by GEOS-5 meteorology, Geoscientific Model Development, 11, 305–319, 2018.

Zender, C. S.: Mineral Dust Entrainment and Deposition (DEAD) model: Description and 1990s dust climatology, J. Geophys. Res., 108, https://doi.org/10.1029/2002jd002775, 2003.

Zhang, G. J. and McFarlane, N. A.: Sensitivity of climate simulations to the parameterization of cumulus convection in the Canadian climate centre general circulation model, Atmosphere-Ocean, 33, 407–446, 1995.

Zhang, L., Gong, S., Padro, J., and Barrie, L.: A size-segregated particle dry deposition scheme for an atmospheric aerosol module, Atmos. Environ., 35, 549–560, 2001.

Zhang, Y., Mathur, R., Bash, J. O., Hogrefe, C., Xing, J., and Roselle, S. J.: Long-term trends in total inorganic nitrogen and sulfur deposition in the US from 1990 to 2010, Atmos. Chem. Phys., 18, 9091–9106, 2018.

Ziemke, Chandra, and Labow: A global climatology of tropospheric and stratospheric ozone derived from Aura OMI and MLS measurements, Atmos. Clim. Sci., 2011.

Supplementary information to:

Implementation and evaluation of the GEOS-Chem chemistry module version 13.1.2 within the Community Earth System Model v2.1

Thibaud M. Fritz[1], Sebastian D. Eastham[1,2]*, Louisa K. Emmons[3], Haipeng Lin[4], Elizabeth W. Lundgren[4], Steve Goldhaber[3], Steven R. H. Barrett[1,2], Daniel J. Jacob[4]

[1]Laboratory for Aviation and the Environment, Department of Aeronautics and Astronautics, Massachusetts Institute of Technology, Cambridge, MA 02139, USA

[2]Joint Program on the Science and Policy of Global Change, Massachusetts Institute of Technology, Cambridge, MA 02139, USA

[3]Atmospheric Chemistry Observations and Modeling Laboratory, National Center for Atmospheric Research, Boulder, CO, USA

[4]John A. Paulson School of Engineering and Applied Sciences, Harvard University, Cambridge, MA 02138, USA

Correspondence to: Sebastian D. Eastham (seastham@mit.edu)

1. Order of routine calls in CAM

CAM performs two sets of calls depending on whether the data has been updated from the land model. The first routine "cam_run1" performs dynamics and atmospheric physics that do not require land model updates, dry adjustment, deep and shallow convection, stratiform macrophysics, MAM wet scavenging and radiation. The second routine "cam_run2" merges the data from the land model and then performs emissions, chemistry, vertical diffusion, Rayleigh friction, MAM dry deposition, gravity wave drag and QBO relaxation.

2. Species mapping between MAM4 and GEOS-Chem species

Table S1 describes the species mapping between MAM4 modal aerosols and GEOS-Chem species.

Table S1: Mapping between MAM4 and GEOS-Chem.

GEOS-Chem species	Mapping to MAM4 species
TSOA0 + ASOAN	soa1_a1 + soa1_a2 + soa2_a1 + soa2_a2

TSOA1 + ASOA1	soa3_a1 + soa3_a2
TSOA2 + ASOA2	soa4_a1 + soa4_a2
TSOA3 + ASOA3	soa5_a1 + soa5_a2
TSOG0	soag0 + soag1
TSOG1 + ASOG1	soag2
TSOG2 + ASOG2	soag3
TSOG3 + ASOG3	soag4
SO4	so4_a1 + so4_a2 + so4_a3 + H2SO4
BCPI	bc_a1
BCPO	bc_a4
OCPI	pom_a1
OCPO	pom_a4
DST1	dst_a1 + dst_a2
DST2	None
DST3	None
DST4	dst_a3
SALA	ncl_a1 + ncl_a2
SALC	ncl_a3

3. Mapping between CLM biogenic emission species and GEOS-Chem species

Table S2 presents the mapping between GEOS-Chem species and MEGAN biogenic emission species as calculated in CLM. Mapping to CAM-chem species is listed in the Supplementary Information of Emmons et al. (2020).

Table S2: Mapping between GEOS-Chem species and MEGAN species in CLM

GEOS-Chem species	MEGAN species in CLM
ISOP	isoprene
MOH	methanol
EOH	ethanol
CH2O	formaldehyde
ALD2	acetaldehyde
ACTA	acetic_acid
ACET	acetone

HCOOH	formic_acid
None	hydrogen_cyanide
CO	carbon_monoxide
C2H6	ethane
C2H4	ethene
C3H8	propane
ALK4	pentane + hexane + heptane + tricyclene
PRPE	propene + butene
TOLU	Toluene
LIMO	Limonene
MTPA	pinene_a + pinene_b + sabinene + carene_3
MTPO	terpinene_g + terpinene_a + terpinolene + myrcene + ocimene_al + ocimene_t_b + ocimene_c_b + thujene_a + 2met_styrene + cymene_p + cymene_o + bornene + fenchene_a + camphene + phellandrene_a + phellandrene_b

4. Emissions mapping in C-GC, C-CC, and S-GC

Table S3 presents the emissions mapping between HEMCO and all three models considered in this study.

Table S3: Emissions mapping from HEMCO to C-GC, C-CC, and S-GC

Emission species	C-GC	C-CC	S-GC
MOH	MOH	CH3OH	MOH
EOH	EOH	C2H5OH	EOH
ROH	ROH	-	ROH
C2H6	C2H6	C2H6	C2H6
C3H8	C3H8	C3H8	C3H8
C4H10	ALK4	BIGALK	ALK4
C5H12	ALK4	BIGALK	ALK4
C6H14	ALK4	BIGALK	ALK4
C2H4	C2H4	C2H4	C2H4
PRPE	PRPE	C3H6	PRPE
C2H2	C2H2	C2H2	C2H2

BENZ	BENZ	BENZENE	BENZ
TOLU	TOLU	TOLUENE	TOLU
XYLE	XYLE	XYLENES	XYLE
TMB	-	XYLENES	-
OTAR	-	XYLENES	-
CH2O	CH2O	CH2O	CH2O
ALD2	ALD2	CH3CHO	ALD2
MEK	MEK	MEK	MEK
ACE	-	CH3COCH3	-
HCOOH	HCOOH	HCOOH	HCOOH
C2OH	-	CH3COOH	-
EOH	EOH	C2H5OH	EOH
MACR	MACR	MACR	MACR
ACET	ACET	CH3COCH3	ACET
BCPI	bc_a*	bc_a*	BCPI
OCPI	pom_a*	pom_a*	OCPI
SO4	so4_a1/so4_a2	so4_a1/so4_a2	SO4

5. Dust emissions in CESM

Emissions of dust in CESM are calculated through the Community Land Model (CLM), with a resolution-dependent scaling factor applied. For this work, we use the same scaling factor (0.24) for both C-CC and C-GC, resulting in dust emissions of 5,894 Tg per year. This is significantly greater than the ~3,000 Tg/yr reported by Emmons et al. (2020), due to the use of a different scaling factor and resolution in that work.

As discussed by Tilmes et al. (2016), the dust emissions scaling factor in CESM is typically tuned to achieve an annual mean dust aerosol optical depth (AOD) of 0.025 – 0.030. We find AODs of 0.04 in C-GC, and 0.08 in C-CC. This suggests that dust removal in C-GC is roughly twice as efficient as in C-CC. This implies that the scaling factor should be reduced in future usage of C-GC or C-CC. The combination of C-GC's relatively small overestimate in dust AOD and the large total dust emissions also implies that dust scavenging in C-GC may be too rapid.

6. Scavenging scheme

Figure S1 shows the calculated wet removal rate of HNO_3 in all three models. Positive values correspond to rain re-evaporation at low altitudes re-releasing dissolved HNO_3. The Neu scavenging scheme in C-GC and C-CC results in an HNO_3 wet removal rate which is four times higher in C-GC than in S-GC. This likely explains the greater depletion of HNO_3 in the mid-troposphere calculated by C-GC compared to S-GC, as shown in Figure 11. Wet scavenging in C-CC is faster yet, with HNO_3 wet removal rates approximately six times greater than in S-GC, and 50% greater than in C-GC. This is in part because the mixing ratio (or fraction of total NO_y) of HNO_3 in the mid- and upper-troposphere as modeled in C-CC is greater than in either C-GC or S-GC, but also because C-GC and S-GC simulate nitrate aerosol explicitly.

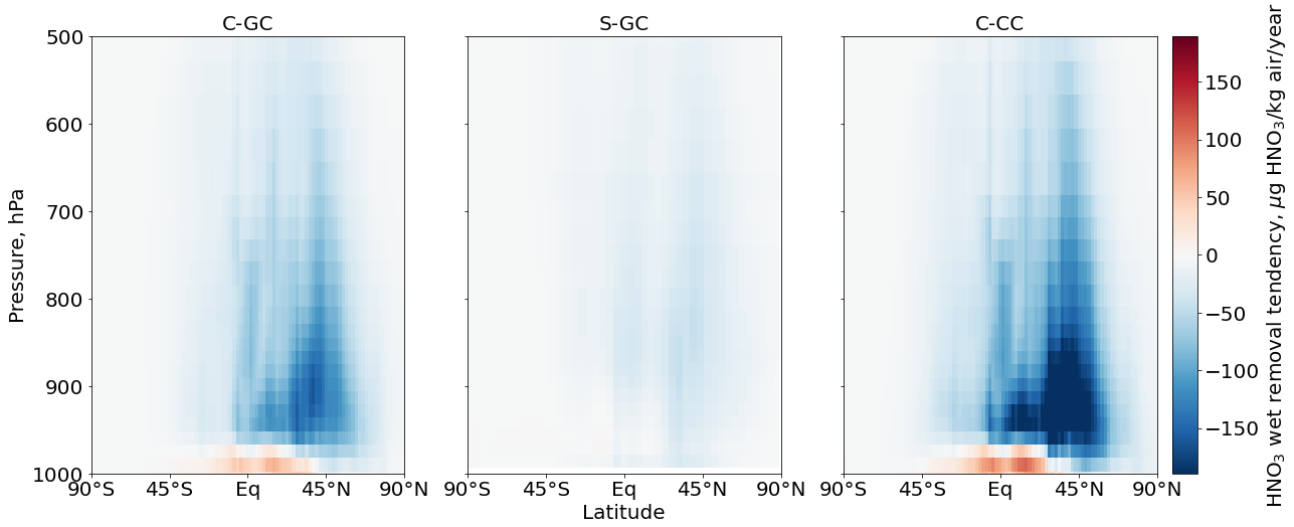

Figure S1: Annual zonal mean of nitric acid wet removal tendencies for C-GC (left), S-GC (middle), and C-CC (right).

The application of the Neu scheme to remove nitrate aerosol also affects removal of total NO_y in C-GC. Figure S2 shows the annual mean wet removal rates of the nitrate aerosol tracer NIT in C-GC and S-GC. The Neu scheme removes aerosol more rapidly than the scheme used in S-GC, and at lower altitudes.

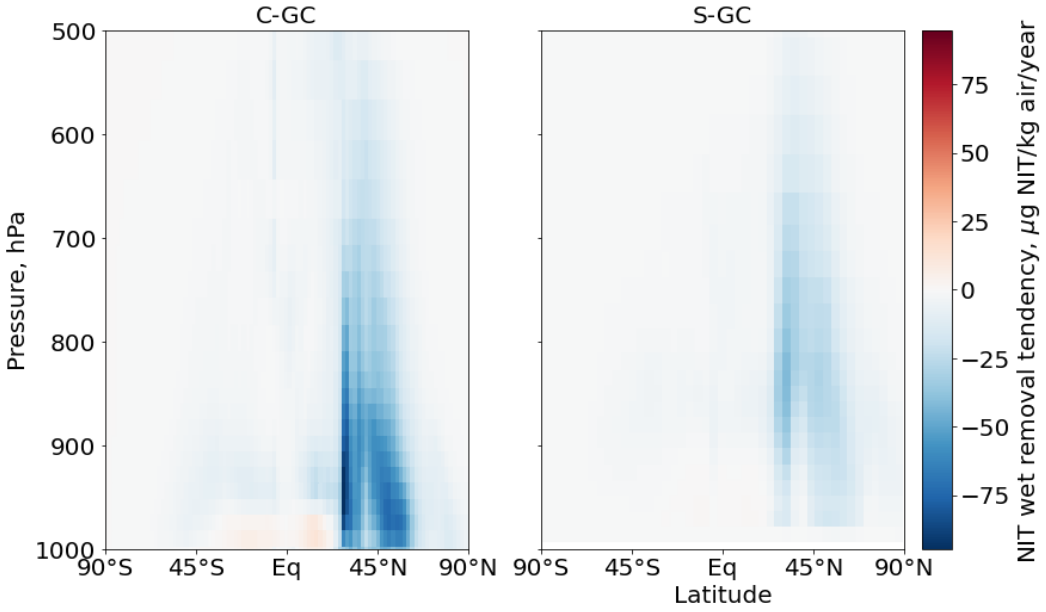

Figure S2: Annual zonal mean of nitrate aerosol (NIT) wet removal tendencies for C-GC (left) and S-GC (right). Nitrate aerosols are not modeled in CAM-chem.

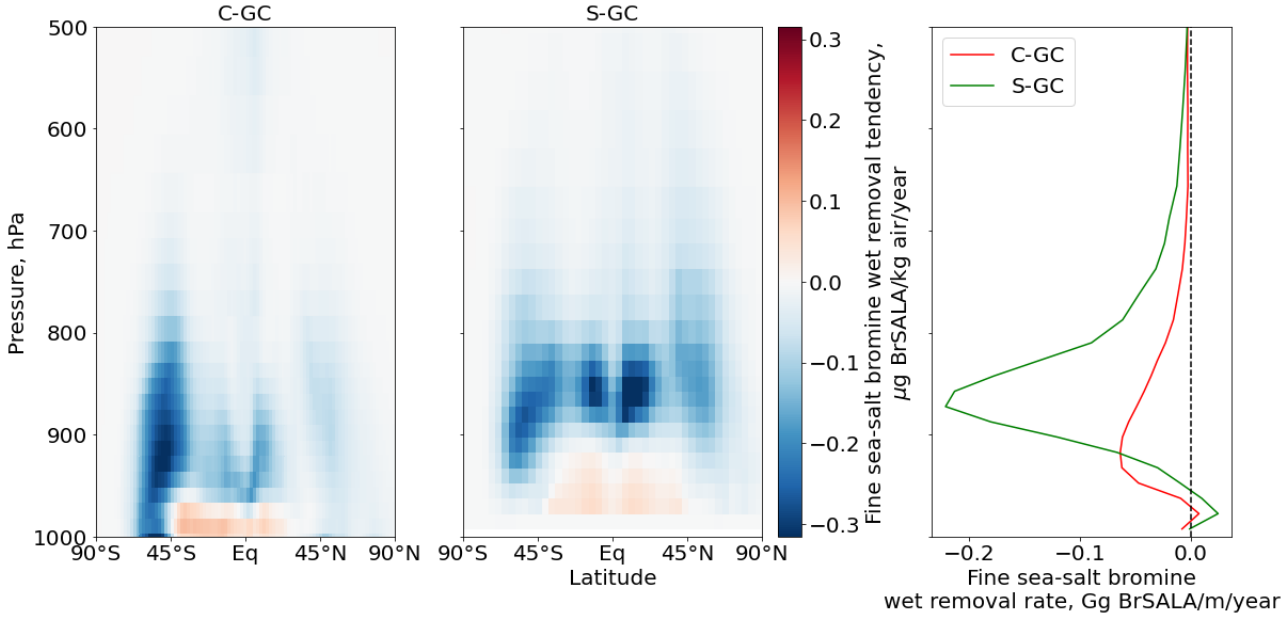

Figure S3. Zonal mean wet removal tendency of bromine carried in fine sea salt**.** Left and middle: Removal rates calculated by C-GC (left) and S-GC (middle). Right: Annual mean of fine sea salt bromine aerosol wet removal rate for C-GC (red), S-GC (green). Bromine in sea-salt aerosol is not modeled in CAM-chem.

7. Surface-level NO_2, NO_x and NO:NO_2 ratio

Figure S4 shows the global distribution of NO_2 and of NO_x ($NO + NO_2$). These data are provided to supplement Figure 17 in the main text, and thus provides some insight into possible causes of disagreements.

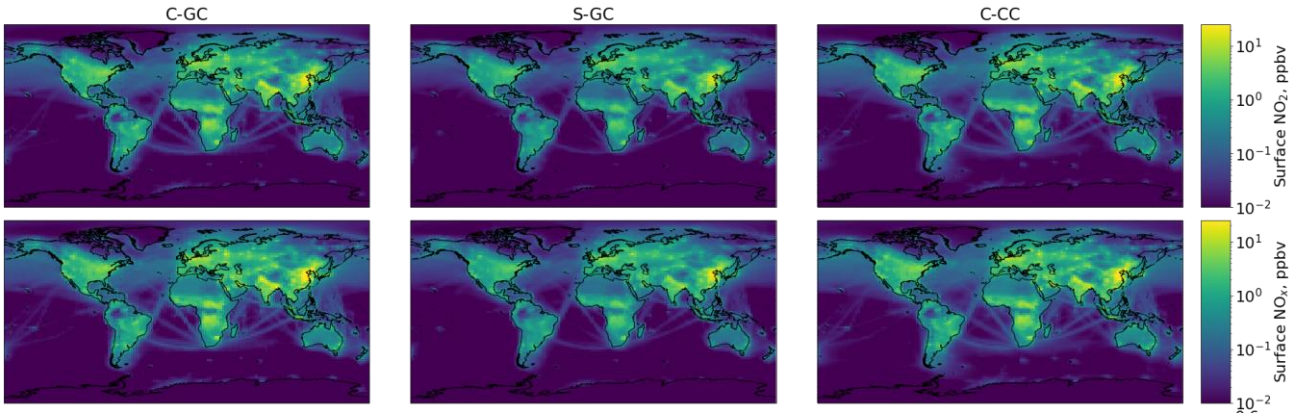

Figure S4: Surface-level NO_2, NO_x, and NO:NO_2 estimated by C-GC (left), S-GC (middle), and C-CC (right) for 2016. Top: annual average NO_2 in ppbv. Bottom: annual average NO_x ($NO + NO_2$) in ppbv..

8. Representations of in-cloud sulfur oxidation in the GEOS-Chem chemistry modules and MAM

Two representations of in-cloud sulfur oxidation exist in C-GC: from the GEOS-Chem chemistry modules and in MAM. For C-GC, we choose to use the GEOS-Chem representation of in-cloud sulfur oxidation, such that the GEOS-Chem chemistry module remains identical to that of the GEOS-Chem CTM. However, this makes C-GC and C-CC, both embedded in CESM2, rely on different processes to perform sulfur oxidation in clouds. The routines responsible for in-cloud sulfur oxidation in MAM are bypassed when running C-GC.

Previous versions of C-GC double counted in-cloud sulfur oxidation. We here perform two test runs of C-GC for January 2015 before and after the sulfur oxidation bugfix - which introduces the bypass of the routines in MAM responsible for in-cloud sulfur oxidation. Figures S5 and S6 display the relative difference in zonal SO_2 and SO_4 attributable to the MAM in-cloud sulfur routines. Implementing this bugfix increases SO_2 and decreases SO_4, enhancing the SO_2 burden by ~5 to 10%.

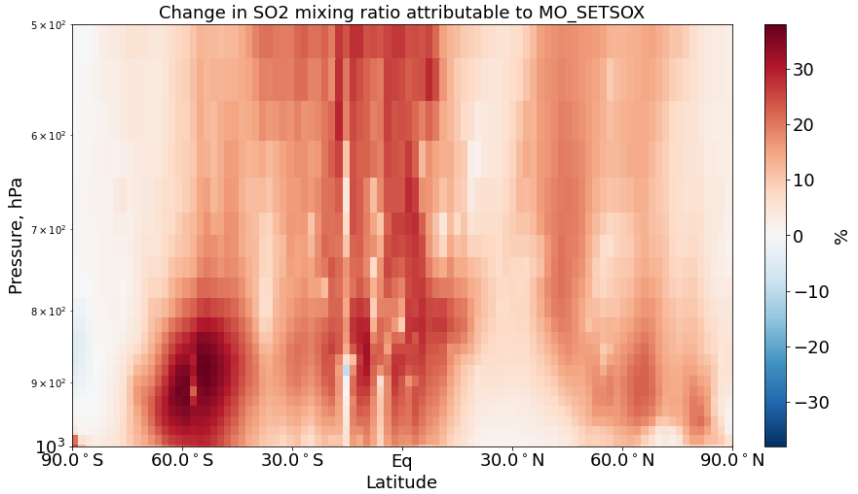

Figure S5: Relative difference in zonally-averaged sulfur dioxide mixing ratios up to 500 hPa due to in-could sulfur oxidation as evaluated by MAM.

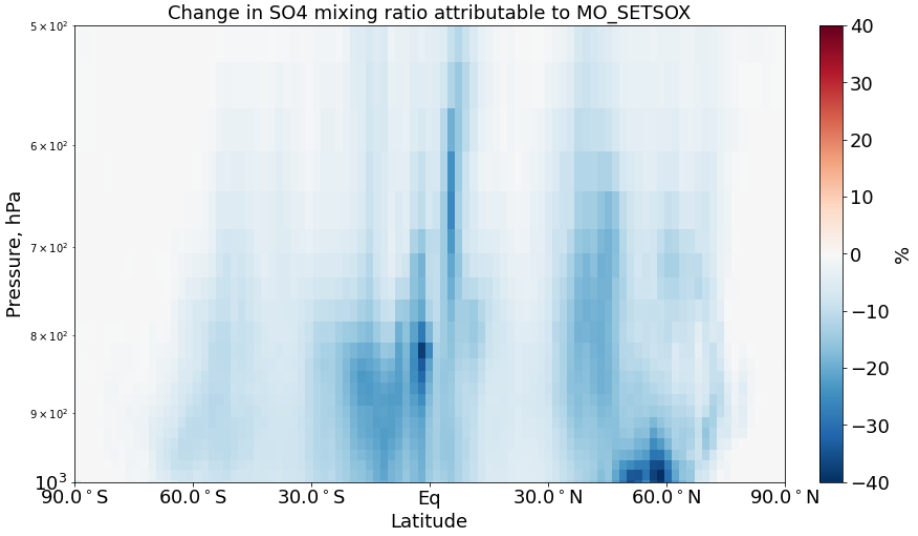

Figure S6: Relative difference in zonally-averaged sulfate aerosols mixing ratios up to 500 hPa due to in-could sulfur oxidation as evaluated by MAM.

9. Non-linear chemistry during the Antarctic spring

This section focuses on the changes in atmospheric composition above the South Pole for C-GC and S-GC. Figures S7, S8, and S9 respectively display active chlorine, inactive chlorine, and ozone, averaged over the 80°S - 90°S latitude band for C-GC and S-GC for 2015 and 2016.

For both C-GC and S-GC, we observe strong production of active chlorine during austral winter. The peak active chlorine mixing ratio is greater in S-GC by ~15%. Correspondingly, we find that reservoir species of chlorine are depleted during austral winter in the 10 to 100 hPa altitude band in both models.

In both models, we find that ozone is depleted during the Antarctic spring (from September to December) due to the presence of active halogens and sunlight. We find that the magnitude of the ozone hole matches from one year to the other in both models (2015 appears to have a more significant ozone hole than 2016). We also find that during the Antarctic spring, ozone around 10 hPa increases in both C-GC and S-GC.

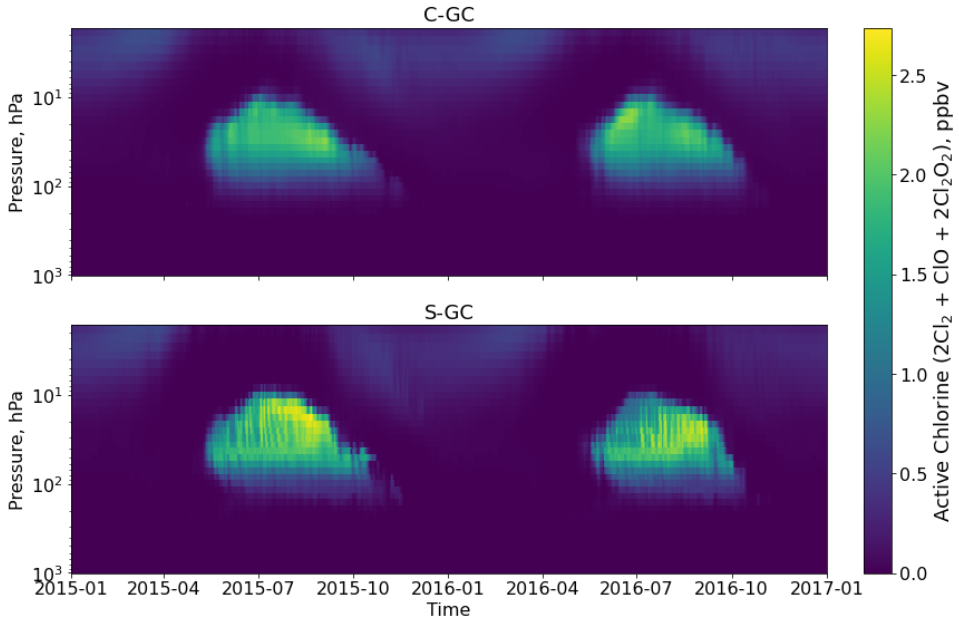

Figure S7: Temporal evolution of active chlorine averaged over the 80°S - 90°S latitude band for C-GC (top) and S-GC (bottom).

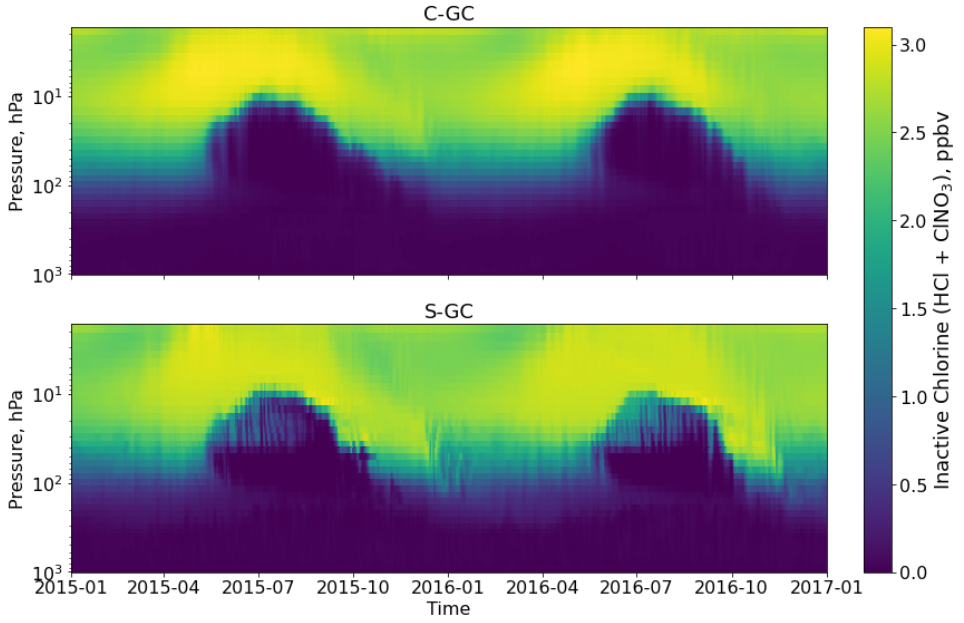

Figure S8: Temporal evolution of inactive chlorine averaged over the 80°S - 90°S latitude band for C-GC (top) and S-GC (bottom).

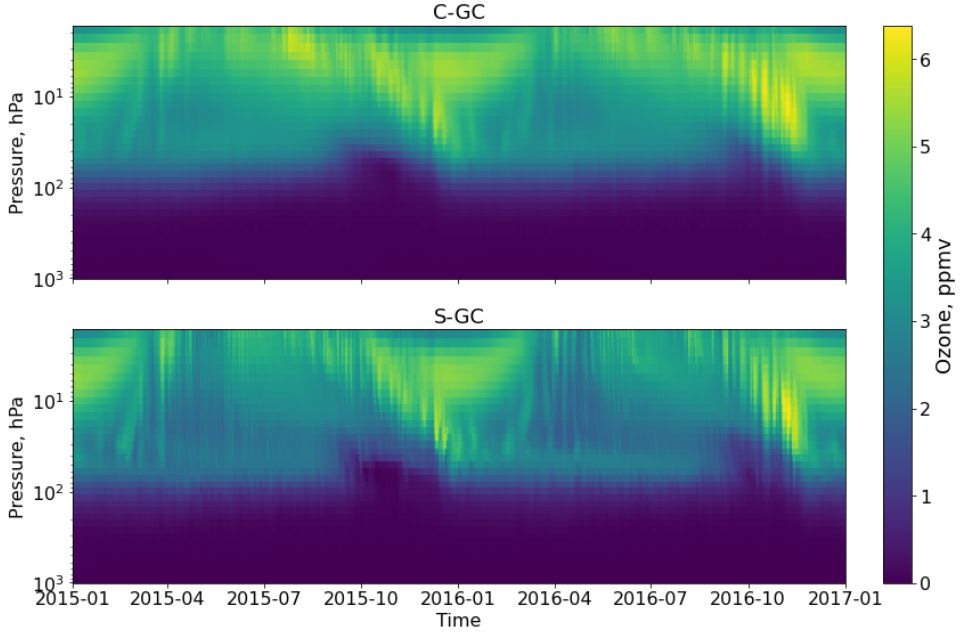

Figure S9. Temporal evolution of ozone averaged over the 80°S - 90°S latitude band for C-GC (top) and S-GC (bottom).

Figure S10 displays the minimum ozone column in the 80°S - 90°S latitude band from C-GC and S-GC against measurements from the NASA Ozone Watch (https://ozonewatch.gsfc.nasa.gov/, last accessed 7 January 2022).

During the Antarctic spring, we find that C-GC more accurately reproduces the dip in the ozone column, but this could be due to differences in the horizontal resolution. We also find that both models fail to capture the increase in the South Pole ozone column between May and July for both 2015 and 2016.

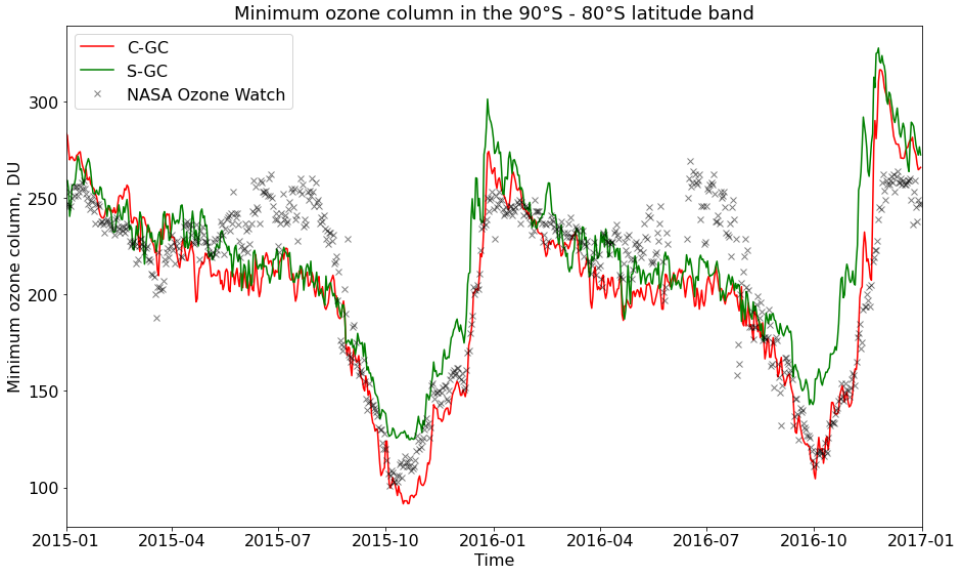

Figure S10: Temporal evolution of minimum ozone column averaged over the 80°S - 90°S latitude band for C-GC (blue) and the GEOS-Chem CTM (red).